

RICE UNIVERSITY

**Nanoparticle Engineering of Multifunctional,  
Multicomponent Microcapsules**

by

**Vinit Satish Murthy**

A THESIS SUBMITTED  
IN PARTIAL FULFILLMENT OF THE  
REQUIREMENTS FOR THE DEGREE

**Doctor of Philosophy**

APPROVED, THESIS COMMITTEE:



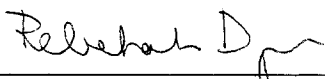
Michael S. Wong, Assistant Professor  
Chemical and Biomolecular Engineering, Chemistry



George J. Hirasaki, A.J. Hartsook Professor  
Chemical and Biomolecular Engineering



Vicki L. Colvin, Professor  
Chemistry, Chemical and Biomolecular Engineering



Rebekah A. Drezek, Stanley C. Moore Assistant Professor  
Bioengineering

HOUSTON, TEXAS

MAY 2006

UMI Number: 3216754

## INFORMATION TO USERS

The quality of this reproduction is dependent upon the quality of the copy submitted. Broken or indistinct print, colored or poor quality illustrations and photographs, print bleed-through, substandard margins, and improper alignment can adversely affect reproduction.

In the unlikely event that the author did not send a complete manuscript and there are missing pages, these will be noted. Also, if unauthorized copyright material had to be removed, a note will indicate the deletion.



---

UMI Microform 3216754

Copyright 2006 by ProQuest Information and Learning Company.

All rights reserved. This microform edition is protected against unauthorized copying under Title 17, United States Code.

ProQuest Information and Learning Company  
300 North Zeeb Road  
P.O. Box 1346  
Ann Arbor, MI 48106-1346

## ABSTRACT

### Nanoparticle Engineering of Multifunctional, Multicomponent Microcapsules

by

Vinit S. Murthy

The objective of this research is to understand and control the assembly of charged nanoparticles (NPs) and polymers to form functional microcapsules. Microcapsules find extensive applications in pharmaceutical, food, and consumer industry by serving as tiny containers to store, deliver, and/or release substances. Nanoparticle-assembled capsules (NACs) are one such model structure, in which NPs and polymer assemble into stable closed-shell structure. Their highly tunable structural features coupled with the nanoscale properties of NPs lead to exciting prospects in encapsulation and controlled release applications. The formation of NACs involves the charge interactions of polymer and NPs. An early form of NACs involved positively-charged polymers combining with negatively-charged gold NPs to form sub-micron-sized spherical aggregates. Water-filled, hollow microspheres were subsequently obtained upon combination of negatively-charged silica NPs with a suspension of gold NP-polymer aggregates, whereupon the silica NPs formed a thick shell. It was discovered that spherical polymer aggregates could be formed by combining a solution of cationic polymers with a multivalent anion salt solution, increasing the versatility of the NP assembly method. These aggregates, upon shell formation with NPs of silica or other negatively-charged compositions, yielded inorganic/polymer NACs. Aggregate formation was investigated as a function of charge

ratio, pH, and time through dynamic light scattering, electrophoretic mobility measurements, chloride ion measurements, and optical microscopy. This two-step synthesis technique is unique among other capsule preparation routes, as it allows the rapid and scalable formation of shells at room temperature, in near-neutral water, and with readily available precursors. These benign synthesis conditions allow encapsulation of sensitive molecules such as enzymes. The synthesis, characterization, and activity of acid phosphatase-containing NACs were studied to demonstrate ease of encapsulation and recoverability. Finally, combining two dissimilar positively-charged polymers and a multivalent anion unexpectedly led to the formation of internally segregated polymer aggregates. These aggregates templated the synthesis of (sub)micron particles with an anisotropic polymer distribution and a surface with discrete polymer patches. The effects of charge and polymer ratios on polymer distribution in these “patchy” particles were studied. Controlled localization of gold NPs within these patches was demonstrated, providing a way to selectively functionalize the surface patches.



## ACKNOWLEDGMENTS

I would like to express my deepest gratitude to my advisor and friend, Professor Michael Wong, for always encouraging me to reach for the stars. I attribute whatever little success which came my way in the last five years, to your superior guidance, unwavering support, and unflinching faith in my modest abilities. For all your words of wisdom, and instilling in me the passion for perfection, I will ever be indebted to you.

This body of work would not have consummated had it not been for the fantastic learning environment provided by the group members of *Catalysis and Nanomaterials Laboratory*. Time flew so fast that it seems only last month when we brought in the Texas longhorn (Milky Way). Thanks, Will Knowles, for turning this crazy idea into reality and also for getting me hooked to Mountain Dew. Your hard-work and an amazing sense of humor has left a lot of us in complete awe. To Mike Nutt, for his ever-ready-to-help attitude. I will always look forward to starting the 3ds Max company with you; we have the potential, the current is favorable, then why the resistance? To Dr. Rohit Rana, for all our interesting conversations ranging from self-assembly to arranged marriages. To Jie Yu, for the Mountain Dew “relief” fund and for all the encouragement you gave in my down-times. To Regina Yoo, thanks a bunch for the polymer dye conjugation. We would have missed out a lot had it not been for your expertise...and your mouth-watering desserts. To the Rice undergraduate students who worked on various aspects of my research: Crystal Ramon, Kush Mathur, Lynh Jones, Grant Belgard, and Chris Barth; your enthusiasm, curiosity, and diligence has often left me amazed. I hope you learnt from me as much as I learnt from you guys. To Shyam Kadali, let's make NITK proud of us (thanks for keeping my research alive).

I would like to express my gratitude to our collaborators Dr. Elizabeth Whitsitt and Prof. Andrew Baron from Rice University's Department of Chemistry. I much appreciate your whole-hearted enthusiasm on the fullerenol project. Liz, thanks for lending your ears and for being such a good team-mate. It was amazing to see how two plus two becomes five.

Special thanks to the current and former staff of Department of Chemical and Biomolecular Engineering at Rice University (Mary Beth McQueen, Cindy Wilkes, Diana Walker, Virginia Morton, Seryu Patel, Heather Dodge, and Richard Chronister) for the helping hand you lent many a times.

To my thesis committee: Professor George Hirasaki, Professor Vicki Colvin, and Professor Rebekah Drezek for taking time out of your hectic schedule to be on board and for all the insights you provided.

For the financial funding, I would like to convey my gratitude to Rice University, Halliburton Energy Services, Kraft Foods, George Kozmetsky Award, Smalley-Curl Innovation Award, and Oak Ridge Faculty Enhancement Award.

A few words need to be said about my apartment-mates for five years: Sushant Dutta and Prasad Dharap. It was through them that I learnt to become a better person and soften my rough edges. Their camaraderie and caring nature was what kept me constantly going. Sushant, I will always cherish the fine moments you brought through your unique movie shows, early morning songs, and "do-chaar pyaar ki batein." Prasad, thanks for ALWAYS being there whenever I needed the most and for making our food group so enviable. Hopefully, our cooking woes will come to a Bollywood-style happy ending, pretty soon.

For all the out-of-lab fun times, I would like to thank my beloved friends Dr. Rajat Duggal, Dr. Vikram Bhide, Priya Gupta, Tushar Prasad, Vipul Singhvi, Atul Singh, Pradeep Bhat, and many more. The Rice experience would have been incomplete without you all. To Amit Saha, for humbling me on the badminton court and teaching that winning is not everything.

Lastly, I would like to thank my family. To my parents, Satish and Vani Murthy, and brother, Srijit Murthy, for their unconditional patience, love, and support all these years. I will always strive hard to make you proud. To my grandparents, K.L. Subbaramaiah and Vasantlakhmi, for ingraining in me the virtues of “work hard and play hard.” To my uncle Dr. Sridhar Subbaramaiah, for teaching me that through determination and hard work, impossibility becomes a relative concept.

## TABLE OF CONTENTS

Abstract .....	ii
Acknowledgements .....	iv
Table of Contents .....	vii
List of Tables .....	x
List of Figures .....	xi
 <b>Chapter 1. Background and research motivation.....</b>	 <b>1</b>
1.1. Assembling nanoparticles into hierarchically ordered structures.....	1
1.2. Synthesis approaches to hollow spheres.....	4
1.2.1. Sacrificial core method (or template-directed method).....	5
1.2.2. Emulsion/phase separation technique.....	6
1.2.3. Nozzle generator technique.....	7
1.2.4. Vesicles and liposomes.....	9
1.3. Research motivation and thesis layout.....	10
1.4. References.....	15
 <b>Chapter 2. Hollow microspheres from flocculation assembly of gold and silica Nanoparticles.....</b>	 <b>25</b>
2.1. Introduction.....	25
2.2. Experimental section.....	27
2.2.1. Materials.....	27
2.2.2. Synthesis.....	29
2.2.3. Characterization.....	30
2.3. Results and discussions.....	32
2.3.1. Hollow microsphere formation.....	32
2.3.2. Au NP-PLL floc formation.....	36
2.3.3. Sphere size control.....	38
2.3.4. Proposed formation mechanism of hollow spheres.....	40
2.3.5. Reversible assembly of hollow spheres.....	42

2.4. Conclusions.....	43
2.5. References.....	44
<b>Chapter 3. Nanoparticle-assembled capsule synthesis: Formation of colloidal polyamine-salt intermediates.....</b>	<b>49</b>
3.1. Introduction.....	49
3.2. Experimental section.....	50
3.2.1. Materials.....	50
3.2.2. Synthesis.....	50
3.2.3. Characterization.....	52
3.3. Results and discussions.....	54
3.3.1. Morphology of PAH-cit aggregates.....	54
3.3.2. Charge ratio $R$ effect on PAH-salt aggregate formation.....	56
3.3.3. Charge ratio $R$ effect on PAH-salt aggregate growth rate.....	60
3.3.4. pH effect on PAH-salt aggregate formation.....	63
3.3.5. PAH-cit aggregate growth mechanism.....	66
3.3.6. Effects of PAH-cit aggregate aging time and $R$ ratio on capsule size.....	71
3.4. Conclusions.....	74
3.5. References.....	75
<b>Chapter 4. Encapsulation of enzymes in nanoparticle-assembled capsules.....</b>	<b>78</b>
4.1. Introduction.....	78
4.1.1. Covalent binding.....	79
4.1.2. Physical adsorption.....	80
4.1.3. Encapsulation.....	81
4.1.4. Physical entrapment.....	82
4.1.5. Crosslinking.....	84
4.2. Experimental section.....	86
4.2.1. Materials.....	86
4.2.2. Synthesis and enzyme assay.....	86
4.2.3. Characterization.....	88

4.3. Results and discussions.....	89
4.3.1. Encapsulation of acid phosphatase.....	89
4.3.2. Protein-containing NACs.....	95
4.3.3. Activity of encapsulated enzyme.....	100
4.3.4. Recoverability studies on encapsulated enzymes.....	101
4.4. Conclusions.....	105
4.5. References.....	106
 <b>Chapter 5. “Patchy” particles formed from polyamine microphase separation..</b>	<b>110</b>
5.1. Introduction.....	110
5.2. Experimental section.....	117
5.2.1. Materials.....	117
5.2.2. Synthesis.....	117
5.2.3. Characterization.....	118
5.3. Results and discussions.....	119
5.3.1. Effect of charge ratio R on aggregate structure.....	122
5.3.2. Effect of PLL/PAH ratio on aggregate internal structure.....	122
5.3.3. Effect of aggregate aging time.....	124
5.3.4. Formation mechanism of microphase-segregated polyamine aggregates.....	125
5.3.5. Effect of PLL/PAH ratio on SiO <sub>2</sub> /polymer microsphere structure.....	136
5.3.6. Anisotropic nanoparticle-assembled capsules.....	138
5.3.7. Spatio-selective localization of gold nanoparticles.....	141
5.4. Conclusions.....	143
5.5. References.....	145
 <b>Chapter 6. Conclusions and recommendations for future work.....</b>	<b>149</b>
 <b>Appendix A. Nanoparticle self-assembly of hierarchically ordered microcapsule                 structures.....</b>	<b>152</b>

## LIST OF TABLES

Table 2.1.	List of various poly- <i>L</i> -lysines used for experiments along with their size and polydispersity information.....	28
Table 2.2.	List of nanoparticles used for experiments.	29
Table 4.1.	Data showing enzyme loading and encapsulation efficiency as a function of acid phosphatase concentration.....	94
Table A.1.	Various sodium salt forms that were used for microcapsule synthesis from PLL (222 kDa) or PAH (70 kDa) and SiO <sub>2</sub> NPs. Charge ratio <i>R</i> was kept at 10 for all the experiments.....	157
Table A.2.	Negatively-charged colloidal species self-assemble into microcapsule structures.....	161

## LIST OF FIGURES

Figure 1.1.	Schematic of procedures for preparing inorganic and hybrid hollow spheres via layer-by-layer coating approach. The scheme is shown for polystyrene latex particle.....	5
Figure 1.2.	Schematic representation of the mechanism of shell formation. Nomenclature: VS – volatile solvent; NVNS – non-volatile non solvent; AI – active ingredient.....	7
Figure 1.3.	(a) Schematic of hollow microsphere generator using coaxial nozzle technique (redrawn from [52]), (b) droplet formation using the coaxial nozzle technology [80], (c) production of coffee oil-alginate capsules in a multi-nozzle unit with the vibration technology.....	8
Figure 1.4.	Experimental set-up for producing Taylor cone.....	8
Figure 1.5.	Schematic diagram depicting the hierarchical self-assembly of gold and silica nanoparticles into hollow spheres with a two layer structure. The addition of Au NP to the disulfide crosslinked block copolypeptide produced globules of gold particles. The introduction of silica NP then drove the formation of hollow micron-sized spheres whose walls were composed of a distinct inner layer of Au NPs followed by an outer layer of silica NPs.....	11
Figure 1.6.	Scanning electron microscopy image of as-synthesized hollow spheres from poly(lysine- <i>b</i> -cysteine) copolymer, Au NPs, and SiO <sub>2</sub> NPs.....	12
Figure 1.7.	Schematic diagram of nanoparticle vesicles and the directional charge-stabilized hydrogen bonds that form between the amines of the poly( <i>L</i> -lysine) and the carboxylic acid group of the citrate stabilized quantum dots. The quantum dots formed the “oily” zone what extends into the exterior and interior water regions are portions of the poly( <i>L</i> -lysine) chains that are not coordinated with the carboxylic acid groups of the citrate-stabilized nanoparticles.....	12
Figure 2.1.	Confocal microscopy images showing the step-by-step formation of microspheres using PLL, Au NP, and SiO <sub>2</sub> NP. (a) PLL3 (conjugated to FITC dye) in solution, (b) globular flocs formed from Au NP–PLL3, and (c) microspheres formed after	



addition of SiO <sub>2</sub> NP to Au NP–PLL3 flocs.....	33
Figure 2.2. Line intensity profile across a microsphere showing the core-shell structure. Note that the fluorescence intensity is non-zero in the core and in the background.....	34
Figure 2.3. (a) Scanning electron microscopy image and (b) confocal microscopy image of microspheres (made from PLL3) after they have been dried and subjected to a vacuum of $5 \times 10^{-5}$ torr at room temperature. Autoquant deblurring software was used to process the raw image in Figure 3(b).....	35
Figure 2.4. TEM images of hollow spheres made from PLL-FITC / Au NP / SiO <sub>2</sub> NP. The spheres were aged for six days before imaging.....	35
Figure 2.5. DLS time measurements of Au NP–PLL floc suspensions prepared with different PLL chain lengths. The error bar at each data point was $\pm 20$ nm.....	37
Figure 2.6. Confocal images of hollow microspheres prepared from Au NP–PLL3 floc suspensions aged from (a) 3 min, (b) 20 min, and (c) 2 hr.....	38
Figure 2.7. Coulter counter analysis of hollow microspheres prepared from Au NP–PLL3 floc suspensions aged for (a) 3 min, (b) 20 min, and (c) 2 hr. The lower limit of detection was $1.04 \mu\text{m}$ . Inset: comparison of size distributions of the Au NP–PLL3 flocs (from DLS) and resultant hollow microspheres (from Coulter counter and confocal image analysis).....	39
Figure 2.8. Confocal images of resultant suspensions (a) after SiO <sub>2</sub> NPs were added to Au NP–PLL3 flocs, (b) after Au NPs were added to SiO <sub>2</sub> NP–PLL3, and (c) after PLL3 was added to a combined Au NP–SiO <sub>2</sub> NP sol.....	40
Figure 2.9. Proposed flocculation-based self-assembly of organic–inorganic hollow spheres from PLL, Au NPs, and SiO <sub>2</sub> NPs.....	41
Figure 2.10 Images from confocal microscopy showing the structural reversibility of microspheres using a pH trigger. (a) As prepared hollow sphere suspension (pH $\sim 4.9$ ), (b) acidification of suspension (final pH $\sim 0.5$ ) causes the spheres to break due to re-dispersion of SiO <sub>2</sub> NP wall, and (c) addition of base to the acidified suspension re-assembles the microspheres (final pH $\sim 10.0$ ).....	42

Figure 3.1.	(a) Brightfield and (b) confocal microscopy images of surface-bound PAH-FITC-cit aggregates in a water environment. (c) AFM images of air-dried PAH-cit aggregates supported on freshly cleaved mica surface. Synthesis conditions: $[\text{PAH}]_{\text{final}} = 1.43 \text{ mg/ml}$ , $[\text{cit}]_{\text{final}} = 10.19 \text{ mM}$ , $R = 2$ , aging time of PAH-cit suspension = 30 min. (d) Brightfield, (e) confocal microscopy, and (f) SEM images of the resultant capsules, after addition of $\text{SiO}_2$ NPs to the-above PAH-cit suspension.....	55
Figure 3.2.	Cryo-TEM image of PAH-cit aggregate suspension. Synthesis conditions: $[\text{PAH}]_{\text{final}} = 0.029 \text{ mg/ml}$ , $[\text{cit}]_{\text{final}} = 0.2 \text{ mM}$ , $R = 2$ , no aging of PAH-cit suspension.....	56
Figure 3.3.	Confocal microscopy images of aggregates formed from PAH and various multivalent salts. Aggregates were formed with (a) tetravalent $\text{EDTA}^{4-}$ and (b) divalent $\text{SO}_4^{2-}$ , but acetate $^{1-}$ (c) did not result in any clusters. Synthesis conditions: $[\text{PAH}]_{\text{final}} = 1.43 \text{ mg/ml}$ , $R = 2$ , aging time = 30 min.....	57
Figure 3.4.	Percentage of total Cl in PAH solution as free ions (square data points) and corresponding pH values (round data points) as a function of charge ratio for multivalent salts: (a) edta, (b) cit, (c) succinate, and (d) acetate. Hatched marks indicate the $R$ values at which aggregate formation occur. Synthesis: $[\text{PAH}]_{\text{final}} = 1.43 \text{ mg/ml}$ , no aging.....	57
Figure 3.5.	Percentage of total Cl in PAH solution as free ions (square data points) and corresponding pH values (round data points) as a function of charge ratio for sulfate salt. Hatched bar shows the $R$ values at which aggregate formation occurs. Synthesis conditions: $[\text{PAH}]_{\text{final}} = 1.43 \text{ mg/ml}$ , no aging.....	60
Figure 3.6.	(a) Hydrodynamic diameter-time curves and (b) electrophoretic mobility and relative growth rates of PAH-cit aggregates as a function of $R$ . Synthesis: $[\text{PAH}]_{\text{final}} = 0.029 \text{ mg/ml}$ .....	61
Figure 3.7.	Critical $R$ values plotted against polymer concentration for PAH-cit system. Data points were collected by visual inspection and laser light scattering.....	61
Figure 3.8.	Effect of suspension pH on PAH-cit aggregate growth using different salts ( $[\text{PAH}]_{\text{final}} = 0.029 \text{ mg/ml}$ , $[\text{cit}]_{\text{final}} = 0.51$ , $R = 5$ ): (a) Aggregate size as a function of aging time. (b) Scattered light intensity (log-scale) of the different PAH-citrate systems. (c) Citrate species distribution calculated as a function of pH, and (d) the calculated species distribution at the pH values of PAH-	

citrate systems shown in (a). The samples were prepared using (i) trisodium citrate, (ii) 50% trisodium citrate + 50% disodium citrate, (iii) disodium citrate, (iv) monosodium citrate, (v) citric acid, (vi) NaCl ( $R = 5$ ), and (vii) no salt..... 64

Figure 3.9. SEM image of spheres formed by addition of glutaraldehyde to PAH-disodium citrate aggregates. Synthesis conditions:  $[\text{PAH}]_{\text{final}} = 0.026 \text{ mg/ml}$ ,  $[\text{disodium citrate}]_{\text{final}} = 0.46 \text{ mM}$ , aging time = 30 min,  $[\text{glutaraldehyde}]_{\text{final}} = 0.26 \text{ M}$ , glutaraldehyde treatment time = 24 hrs..... 65

Figure 3.10. Confocal microscopy images of PAH-cit aggregates aged for various times (1 min, 20 min, and 30 min): FITC-tagged PAH-cit aggregates aged for (a) 1 min, (b) 20 min, and (c) 30 min; RITC-tagged PAH-cit aggregates aged for (f) 1 min, (g) 20 min, and (h) 30 min; and the resultant aggregates after combining the 19-minute-aged FITC- and RITC-tagged suspensions from (a) and (f), respectively, and aging for (d) 1 min and (e) 11 min. Synthesis:  $[\text{PAH}]_{\text{final}} = 1.43 \text{ mg/ml}$ ,  $[\text{cit}]_{\text{final}} = 10.19 \text{ mM}$ ,  $R = 2$ . Scale bars:  $10 \mu\text{m}$ ..... 67

Figure 3.11 PAH-cit aggregate growth as a function of PAH precursor concentration: (a)  $D_h$  vs. time, (b)  $D_h^3$  vs. time, and (c) rate constant vs. polymer concentration. The highest precursor PAH concentration tested was  $0.50 \text{ mg/ml}$ , due to multiple scattering of the PAH-cit suspensions at higher PAH concentrations. Synthesis:  $[\text{PAH}]_{\text{final}} = [\text{PAH}]_{\text{precursor}} \div 3.5$ ;  $R = 5$ ..... 68

Figure 3.12 Time-lapse brightfield microscopy images of concentrated PAH-cit aggregate "droplets." The field of view did not change. Time zero corresponds to when the 10-second vortex mixing stopped. Synthesis:  $[\text{PAH}]_{\text{final}} = 11.43 \text{ mg/ml}$ ,  $[\text{cit}]_{\text{final}} = 50.9 \text{ mM}$  ( $R = 1.2$ ). Scale bar:  $50 \mu\text{m}$ ..... 70

Figure 3.13. Time-lapse differential interference contrast images of PAH-cit aggregates (low coverage of glass slide). Time  $t = 0$  corresponds to the time when the 10 sec vortex mixing of PAH-cit solution was stopped. Synthesis conditions:  $[\text{PAH}]_{\text{final}} = 11.4 \text{ mg/ml}$ ,  $[\text{cit}]_{\text{final}} = 50.9 \text{ mM}$ ,  $R = 1.2$ . Scale bar:  $50 \mu\text{m}$ ..... 70

Figure 3.14. Optical microscopy images of product formed after combining  $\text{SiO}_2$  NPs with PAH-cit samples of varying  $R$  ratios: (a)  $R = 0$ , (b)  $R = 0.3$ , (c)  $R = 1$ , (d)  $R = 5$ , (e)  $R = 10$ , and (f)  $R = 20$ . Critical ratio  $R_c = 0.6$ .  $[\text{PAH}]_{\text{final}} = 0.83 \text{ mg/ml}$ ,  $[\text{SiO}_2 \text{ NP}]_{\text{final}} = 8.5 \text{ wt.}\%$ , aging time after NP addition = 30 min..... 71

Figure 3.15.	Brightfield and confocal microscopy images of NACs prepared from PAH-FITC-cit aggregates aged for 10 sec (a,b) and 30 min (d,e). (c,f) Size distributions of PAH-cit aggregates (filled circles) aged for 10 sec and 30 min, respectively, and the resultant NACs (open circles). $[\text{PAH}]_{\text{final}} = 0.83 \text{ mg/ml}$ , $[\text{cit}]_{\text{final}} = 5.94 \text{ mM}$ , $[\text{SiO}_2 \text{ NP}]_{\text{final}} = 8.5 \text{ wt\%}$ , aging time after NP addition = 30 min.....	73
Figure 3.16.	SEM image of an ultramicrotomed capsule. The NACs were prepared from PAH-cit aggregates and $\text{SiO}_2$ NPs. $[\text{PAH}]_{\text{final}} = 0.83 \text{ mg/ml}$ , $[\text{cit}]_{\text{final}} = 5.94 \text{ mM}$ , $R = 2$ , aggregate aging time = 30 min, $[\text{SiO}_2 \text{ NP}]_{\text{final}} = 8.5 \text{ wt\%}$ .....	74
Figure 4.1.	Schematic showing the enzyme molecules covalently bound to the substrate.....	80
Figure 4.2.	Schematic showing physical adsorption of enzyme molecules on the substrate.....	81
Figure 4.3.	Schematic showing encapsulation of enzymes.....	82
Figure 4.4.	Schematic showing physical entrapment of enzymes in a substrate matrix.....	83
Figure 4.5	Schematic showing the crosslinking of enzyme molecules.....	84
Figure 4.6.	Conceptual diagram illustrating three-step encapsulation of enzyme in NACs.....	90
Figure 4.7.	Three-dimensional structure of rat acid phosphatase.....	90
Figure 4.8.	(a,c) Bright field and (b,d) confocal microscopy images of (a,b) PLL-cit-AP aggregates and (c,d) of AP-containing $\text{SiO}_2$ NACs. $[\text{PLL}]_{\text{final}} = 0.13 \text{ mg/ml}$ ; $[\text{cit}]_{\text{final}} = 2.1 \text{ mM}$ ; $[\text{SiO}_2 \text{ NP}]_{\text{final}} = 7.9 \text{ wt\%}$ ; $[\text{AP}]_{\text{final}} = 0.26 \text{ mg/ml}$ . PLL is tagged with FITC.....	92
Figure 4.9.	SEM images of AP-containing $\text{SiO}_2$ NACs for different amounts of enzyme added to the PLL-cit aggregates. (a) $[\text{AP}]_{\text{final}} = 0.0 \text{ mg/ml}$ , (b) $[\text{AP}]_{\text{final}} = 0.019 \text{ mg/ml}$ , (c) $[\text{AP}]_{\text{final}} = 0.034 \text{ mg/ml}$ , (d) $[\text{AP}]_{\text{final}} = 0.10 \text{ mg}$ , and (e) $[\text{AP}]_{\text{final}} = 0.26 \text{ mg}$ .....	95
Figure 4.10.	(a) Bright field, (b) confocal, and (c,d) scanning electron microscopy images of PLL-cit-BSA aggregates. Inset: Fluorescence intensity line profile of a BSA microsphere. $[\text{PLL}]_{\text{final}} = 0.21 \text{ mg/ml}$ ; $[\text{cit}]_{\text{final}} = 3.4 \text{ mM}$ ; $[\text{BSA}]_{\text{final}} = 5.1 \text{ mg/ml}$ .....	97

Figure 4.11.	(a) Bright field, (b) confocal, and (c,d) scanning electron microscopy images of BSA-containing silica NACs. $[\text{PLL}]_{\text{final}} = 0.13 \text{ mg/ml}$ ; $[\text{cit}]_{\text{final}} = 2.1 \text{ mM}$ ; $[\text{BSA}]_{\text{final}} = 3.1 \text{ mg/ml}$ ; $[\text{SiO}_2 \text{ NP}]_{\text{final}} = 7.9 \text{ wt\%}$ .....	98
Figure 4.12.	(a,c) Bright field and (b,d) confocal microscopy images of (a,b) disintegrated PLL-cit-BSA aggregates and (c,d) of BSA-containing $\text{SiO}_2$ NACs incubated in protease enzyme for 15 hr time period at room temperature.....	99
Figure 4.13.	Series of time-lapse fluorescence microscopy images of phosphatase-containing $\text{SiO}_2$ NACs suspended in an aqueous solution of FDP ((a) 3 min, (b) 15 min, and (c) 30 min). Non-fluorescent FDP diffuses inside the NACs, interacts with the enzyme, and fluorescent product (fluorescein) diffuses out. The images were pseudo-colored to visually enhance the concentration gradient. Scale bar: $10 \mu\text{m}$ .....	100
Figure 4.14.	Schematic showing the step-by-step protocol for conducting recoverability studies of encapsulated enzyme.....	102
Figure 4.15.	Graphs showing the increase in product concentration in the presence of (a) encapsulated enzyme and (b) free enzyme for three cycles. The solid lines are guide to the eyes. Histogram in (c) shows a comparison of the activities of free and encapsulated enzymes.....	104
Figure 5.1.	Model patchy particles studied by Zhang and Glotzer. (a) Side view of patchy sphere with two diametrically opposed circular patches, Red beads represent the coarse-grained “atoms” in the patches; yellow beads represent the rest of the particle, (b) axial view of the patchy sphere in (a), (c) side view of sphere with ring-like patch on the equator, and (d) axial view of sphere in (c).....	111
Figure 5.2.	Equilibrium structures formed by particles in Fig. 5.1. (a) Long chains formed by patchy spheres in Fig. 5.1a and (b) Side view of sheets formed by spheres with ring-like equatorial patch as shown in Fig. 5.1b.....	111
Figure 5.3.	Schematic procedure of preparation of nonsymmetrical microspheres by the L-B technique. The copolymer monolayers were transferred onto the monolayer of microspheres to modify a restricted part of the microsphere surface.....	112

Figure 5.4.	Scheme of the preparation of dipolar colloidal particles by microcontact printing of water-insoluble cationic surfactant on a monolayer of sulfate latex particles.....	113
Figure 5.5.	Schematic description of the fabrication process of the half-coated particle via vapor deposition of gold.....	114
Figure 5.6.	Schematic of the procedure to synthesize dissymmetric nanoparticles. In gray: silica nanoparticles; in black: gold nanoparticles.....	115
Figure 5.7.	(a) A schematic diagram of the experimental setup used for electrohydrodynamic processing. When exposed to an applied electric potential (5–15 kV depending on the jetting conditions), the bipolar jetting liquid experiences an electrical field that is formed between the tip of the liquid and the counter-electrode (collecting substrate). For certain parameter combinations, well-structured biphasic Taylor cones were observed at the tip of the nozzle, consisting of two aligned fluid phases (b) A digital image of a typical biphasic Taylor cone with jet. Each phase was labeled by addition of 0.5% w/v of a fluorescent dye, that is, fluorescein isothiocyanate-conjugated dextran (green) and rhodamine-B-conjugated dextran (red). The inset shows a detailed image of the swirl-like jet ejection point.....	115
Figure 5.8.	(a) Confocal image of homogenous 50/50 aqueous mixture of PLL/PAH, (b) confocal image of microphase-separated PLL/PAH-cit aggregates, (c) DIC image of microphase-separated PLL/PAH-cit aggregates (50/50) with non-conjugated PLL and PAH, (d) confocal image of anisotropic microspheres from addition of silicic acid to (b), (e) SEM image of an microsphere from addition of silicic acid to (b), and (d) confocal image of anisotropic NACs from addition of 13 nm SiO <sub>2</sub> NP to (b).....	120
Figure 5.9.	Confocal microscopy images of PLL/PAH-cit aggregates with varying relative amounts of PLL/PAH. (a) 100/0, (b) 90/10, (c) 75/25, (d) 50/50, (e) 25/75, (f) 10/90, and (g) 0/100.....	123
Figure 5.10.	Confocal microscopy images of representative PLL/PAH-cit aggregates. Aliquots were withdrawn from the aggregates suspension at different times: (a) 5 sec, (b) 5 min, and (c) 30 min. PLL/PAH ratio was kept constant at 50/50.....	125
Figure 5.11.	Schematic for the formation and growth mechanism of microphase-segregated polyamine aggregates.....	126

Figure 5.12.	Confocal images of (a) PAH-cit aggregates aged for 10 min, (b) PLL-cit aggregates aged for 10 min, (c) composite aggregates formed by mixing (a) and (b) and aging for 5 sec, (d) composite aggregates obtained after aging (c) for 10 min.....	127
Figure 5.13.	Confocal microscopy images of suspensions obtained after mixing PLL/PAH-FITC-cit and PLL/PAH-Rhod-cit aggregates for 75/25 mixture (aged for (a) 5 sec and (b) 10 min) and 25/75 mixture (aged for (c) 5 sec and (d) 10 min).....	128
Figure 5.14.	Schematic showing a drop of liquid on a solid substrate.....	130
Figure 5.15.	Schematic showing the spreading behavior of one liquid on another immiscible liquid droplet in the presence of a third mutually immiscible liquid.....	131
Figure 5.16.	Possible equilibrium configurations when two immiscible droplets (phase 1 and 3) are suspended in a third immiscible medium (phase 2, not shown).....	134
Figure 5.17.	Confocal microscopy images of SiO <sub>2</sub> /polymer microspheres prepared from PLL-FITC/PAH-Rhod-cit aggregates with varying relative amounts of PLL/PAH: (a) 100/0, (b) 90/10, (c) 75/25, (d) 50/50, (e) 25/75, (f) 10/90, and (g) 0/100.....	136
Figure 5.18.	SEM images of SiO <sub>2</sub> /polymer microspheres with varying relative amounts of PLL/PAH. (a) 100/0, (b) 90/10, (c) 75/25, (d) 50/50, (e) 25/75, (f) 10/90, and (g) 0/100.....	138
Figure 5.19.	Confocal microscopy images of NACs prepared from PLL-FITC/PAH-Rhod-cit aggregates with varying relative amounts of PLL/PAH: (a) 100/0, (b) 90/10, (c) 75/25, (d) 50/50, (e) 25/75, (f) 10/90, and (g) 0/100.....	140
Figure 5.20.	Reactions scheme showing the conjugation of non-fluorescence fluorescamine with primary amine groups to yield a fluorescent product.....	141
Figure 5.21.	Schematic showing four possible modes to impart spatial control of Au NPs inside microspheres.....	142
Figure 5.22.	Optical microscopy images of PLL/PAH (50/50) microspheres with controlled localization of Au NPs (a) evenly located throughout the microspheres, (b) located only within the PAH domains, (c) located on the periphery of the PAH domains, and (d) located on the external surface of the microsphere.....	143

- Figure A.1. Tandem self-assembly of microcapsules. **(a)** Proposed schematic of the tandem, two-step formation process, in which positively-charged polymer chains ionic crosslink with multivalent anions, and silica NPs subsequently deposit around the polymer aggregates. **(b)** Confocal microscopy image of EDTA-bridged PLL-FITC aggregates. **(c-e)** Brightfield and confocal and (Inset) combined confocal/brightfield images of three different silica structures suspended in water, and **(f-h)** SEM and **(i-k)** TEM images of the corresponding dried structures: **(c,f,i)** microcapsules self-assembled from SiO<sub>2</sub> NPs, EDTA, and PLL, **(d,g,j)** microspheres synthesized using silicic acid, EDTA, and PLL, and **(e,h,k)** microcapsules self-assembled from SiO<sub>2</sub> NPs, citrate, and PLL. All scale bars, 5  $\mu\text{m}$ ..... 154
- Figure A.2. Citrate-bridged PAH aggregates in microcapsule formation. **(a)** Aggregate growth curves of citrate and PAH suspensions at different charge ratios  $R$ . The charge ratio was adjusted with varying amounts of citrate. The citrate and polymer were combined at an aging time of 0 min. The suspensions could not be analyzed at times earlier than  $\sim 2$  min due to experimental limitations. **(b)** Aggregate growth rates (at 2 min, determined from growth curves of **(a)**), zeta potentials, and %dissociation of Cl ions at different  $R$ 's. Growth rates were normalized to maximum growth rate (found at  $R = 50$ ). **(c)** Size distributions of citrate-bridged PAH aggregate ( $R = 10$ ) at 3 min and 30 minutes. **(d)** Optical microscopy images of microcapsules prepared from corresponding PAH aggregates. Scale bars, 5  $\mu\text{m}$ ..... 160
- Figure A.3. Tapping mode AFM of **(a)** citrate-bridged PAH aggregates and **(b)** microcapsules formed on a mica support. After aging the citrate-bridged PAH suspension for 30 min, 100  $\mu\text{l}$  of the suspension was dropped on a freshly cleaved mica surface. After 1 min, the suspension was rinsed with deionized water, and the substrate dried overnight before imaging. For the microcapsule formation, 100  $\mu\text{l}$  of silica colloidal suspension was dropped on to the above freshly added PAH aggregates on a mica support. It was then aged for 30 min, rinsed with deionized water and then dried overnight before imaging. Height scale, 4  $\mu\text{m}$ ..... 162
- Figure A.4. Representative microcapsules prepared from citrate-bridged PLL aggregates and SiO<sub>2</sub> NPs that contain *acid phosphatase* enzyme, in an aqueous solution containing fluorescein diphosphate: **(a)** a series of time-lapse confocal microscopy images collected over the course of 30 min, **(b)** brightfield image, and **(c)** line intensity profiles along the red line shown in **(b)**. The reactant diffuses inside the microcapsules and interacts with the encapsulated



enzyme to form the fluorescent fluorescein product. Scale bars:  
2  $\mu\text{m}$ .....

## **Chapter 1. Background and research motivation**

### **1.1. Assembling nanoparticles into hierarchically ordered structures**

Recent years have seen the emergence of new synthesis routes to nanoparticle-based materials in which there is well defined spatial ordering of the nanoparticle (NP) building blocks [1-22]. Such routes range from crosslinking of NPs functionalized with molecules that participate in complementary binding (*e.g.*, antibody-antigen [23], DNA oligonucleotides [24], streptavidin-biotin [25], and diaminotriazine-thymine pairs [26], to the organization of NPs into rings [27], wires [3,28], and superlattices [4,6,29,30], induced by solvent evaporation [11,31] and by application of external fields [32,33]. Layer-by-layer assembly based on electrostatically “sandwiching” oppositely charged polyelectrolyte-NP layers has also been conceived to direct the formation of thin films [9,34]. Such bottom-up “brick-and-mortar” synthesis approaches achieved by selective non-covalent bonding, provides a powerful tool to synthesize NP-based structured systems [24]. In some cases, these NP-based materials can be further extended to fabricate real-world macroscopic functional structures that exhibit the optical, electronic, magnetic, or catalytic properties of the constituent NPs. These properties become extremely sensitive to the length scales at nanometer levels; thus, controlling the NP assembly becomes the crucial first step towards fine tuning the macroscopic properties.

As noted by Alivisatos [35], there are not many ways of controlling the particle-particle interactions at such a small length scale owing to the limited knowledge of colloid science and also to insufficient nanoscale characterization techniques. Mirkin and coworkers showed that interparticle distance, and hence, optical properties of gold NPs can be controlled precisely by adsorbing complementary DNA strands of specific lengths

on the Au surface [36]. The molecular recognition property of DNA strands guides the assembly of NP building blocks with complementary recognition elements to build ordered nanoparticle network [1,27]. This complementary base binding is reversible upon increasing the temperature (hence bringing about a change in the color of Au NP aliquot) of the colloid suspension [37]. The thermodynamics governing the adsorption of these DNA strands and the affinity of particular bases over the others for Au surface has also been studied [38,39]. This work is not only interesting from a materials point of view but also lends itself to practical applications in clinical diagnostics [40] or detection of biological warfare agents such as anthrax [2].

Mann and coworkers have also taken advantage of molecule recognition-driven assembly. Protein-substrate binding has been used to program the self-assembly of NP-based structures [26,41]. The highly specific recognition properties of antibody–antigen and streptavidin–biotin molecules [42] have been suggested to make it possible to assemble a wide range of NP-based structures, compositions, and macroscopic architectures.

Template-directed assembly giving rise to ordered structures in the nano- and micrometer size regimes has been sought after recently. The template can be in the form of a colloidal particle [9,43], polymer micelle [44], vesicle [45], virus crystals [46], emulsions [47], or scaffolds formed by organic [48] or inorganic entities [49,50]. The NPs are either adsorbed on the templates via electrostatic attraction or cross-linked through covalent bonds thus maintaining the template shape. The template is later calcined, or dissolved using suitable solvents where a hollow morphology is needed.

Among the many ordered structures formed via NP assembly, there has been a revived interest in the synthesis of a class of materials called hollow spheres or capsules in the micron ( $> 1000$  nm), sub-micron (100–1000 nm), and nanometer (10–100 nm) size ranges. A capsule is essentially a hollow container consisting of an outer shell wall which protects the internal contents (also called payload or active ingredient). The shell wall can be designed to release its contents at the desired time and place by rupturing, melting, dissolving or degrading its constituents. Hollow spheres permeate various markets such as consumer (detergents, antiperspirants, over-the-counter medicines), chemicals (catalysts, paints, adhesives, corrosion inhibitors), pharmaceuticals (antibiotics, biocells, medicines, bioactive agents), agriculture (pesticides/herbicides/fungicides, growth regulators, food, supplements for animal feed, veterinary medicines), and food (flavors, preservatives, coloring agents, vitamins, and other food supplements) [51-58]. The various applications to which they have been put to are: providing controlled and/or sustained release of the payload, separate reactive materials, protect and extend storage life of contents, control the start of the reaction, mask taste, odor and/or color of contents, reduce toxicity, or volatility, and even convert liquid to solid.

One of the first applications of micron-sized capsules was that of carbonless copy paper (in duplicate personal bank checks) which was invented by David Steinhardt [59,60]. The carbonless copy paper works in a fairly simple manner: The bottom part of the top sheet is coated with a layer of microcapsules containing a special invisible ink. When the top sheet is written on, the pressure from the writing instrument causes the microcapsules to rupture and spill their ink. This ink reacts quickly with the chemical coated on the top of the second sheet to form a permanent impression. Since the capsules

are very small, the impression formed is very accurate. With a similar concept, new generations of aircraft paints contain encapsulated stain-inducing additives that discolor at the point of surface impact, thereby warning of possible structural damage [61]. Hence, the burgeoning uses of microcapsules confirm their rich palette of functional capabilities and suggest their future outlook is one of growth.

So, why should anyone be interested in hollow capsules made out of NPs? As building blocks to create hierarchical structures such as hollow capsules, NPs offer a wide spectrum of chemical, mechanical, and optical properties to choose from much like the tinker toy construction set. A large amount of research has already been performed in the area of NP synthesis and an enormous variety of NPs with different material constituents, sizes, and exotic shapes have been fabricated. These NPs can be further functionalized with specific chemical groups relatively easily. As a result, one can confer the desired properties to microcapsules by choosing appropriate NPs, an advantage, which other building blocks do not necessarily offer.

## **1.2. Synthesis approaches to hollow spheres**

Various approaches have been taken by workers for the fabrication of hollow spheres in the micron ( $> 1000$  nm), sub-micron (100–1000 nm), and nanometer (10–100 nm) size regimes, resulting in both organic and inorganic spheres. These methods can be categorized into four broad categories as given below:

### 1.2.1. Sacrificial core method (or template-directed method)

The starting point for this method involves selecting a solid [9] or a liquid core [47] around which an even coating of shell material is deposited. The shell is formed either via depositing alternate layers of positive and negative species (such as NPs and/or polymers) (see Fig. 1.1) [43,62,63], sol-gel chemistry [64-67], polymerization [68], or adsorption of smaller particles [49,50].

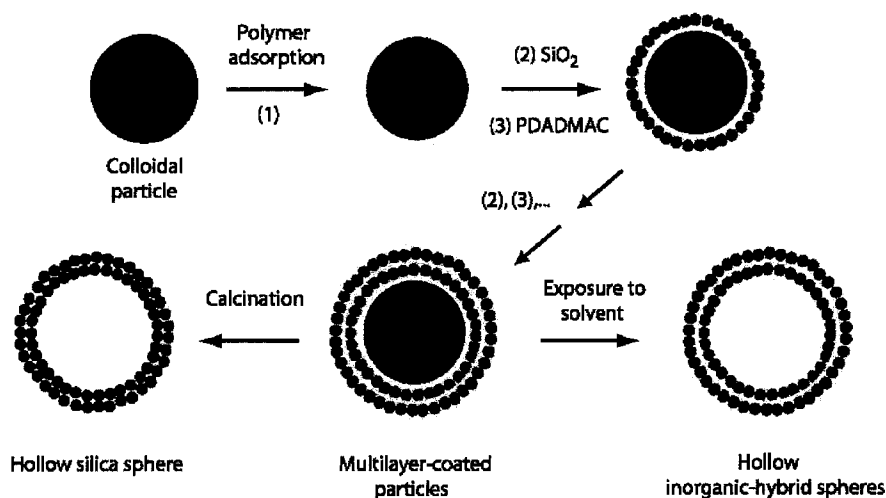


**Figure 1.1.** Schematic of procedures for preparing inorganic and hybrid hollow spheres via layer-by-layer coating approach. The scheme is shown for polystyrene latex particle (redrawn from [9]).

The core is subsequently dissolved in a suitable solvent or volatilized at high temperatures [69] leaving behind the coating which forms the desired hollow shell. The sacrificial core templating approach can yield stable hollow spheres with uniform diameters if solid particles are used as the template and a thick shell is formed. Besides latex particles, other materials can be used as the template, like metal nanoparticles, vesicles, micelles, emulsion droplets, and inverse opals depending on the desired size of the final capsules [47,49,66,70-73]. This approach is highly flexible, though it requires

more processing steps than the self-assembly routes (*vide post*). Encapsulation of sensitive compounds is not trivial, though, as the template removal step must be carried out in such a way as to not damage the encapsulated compounds.

### 1.2.2. Emulsion/phase separation technique

This technique takes advantage of the interfacial forces and immiscibility criterion between two or more liquid phases. In one simple case, a polymer is dissolved in a water-immiscible volatile solvent. The active ingredient to be encapsulated is added in the polymer solution. This polymer-solvent-drug solution is then emulsified in water containing emulsifying agent such as poly(vinyl alcohol) to form oil-in-water emulsion. The emulsion is then subjected to slightly elevated temperatures and/or reduced pressures to evaporate the volatile solvent thus precipitating the polymer, yielding a stable shell wall. The polymer solvent can also be extracted out by a third liquid [74].

In another example, Vincent and coworkers successfully prepared polymer shells containing oil cores by preparing oil in water emulsion wherein the oil phase consisted of a polymer mixed with a good solvent (dichloromethane) and a bad solvent (hexadecane, decane, octanol, tetrachloromethane) (see Fig. 1.2). The good solvent was then evaporated at slightly elevated temperatures under reduced pressure causing the polymer to phase separate forming a stable shell wall [75-77]. One of the advantages of O/W emulsification method is that a large variety of hydrophobic substances (such as steroids) can be encapsulated in the core. However, the encapsulation of water-soluble drugs is difficult *via* this technique [78,79].

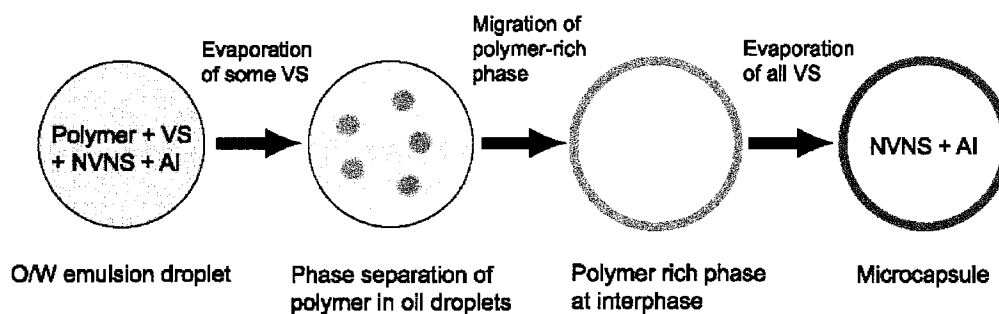


**Figure 1.2.** Schematic representation of the mechanism of shell formation (redrawn from [77]). Nomenclature: VS - volatile solvent; NVNS - non-volatile non solvent; AI - active ingredient.

### 1.2.3. Nozzle generator technique

This method is based on the design and use of nozzle systems which dispense individual liquid droplets to carefully controlled dimensions of the materials of interest. In its simple form, nozzles have been developed with two or more concentric openings to facilitate the creation of hollow spheres using a fill gas/liquid or to create spheres with layered structures [52] (Fig. 1.3). A broad variety of enhanced nozzle systems have been developed which provide unique sources of energy to create the droplets, and subsequently, hollow spheres. In one approach known as electro-spraying, a conducting liquid is slowly injected through a charged capillary tube. When the electrostatic potential between the liquid and the capillary wall rises to a few kilowatts, the meniscus at the capillary tip develops a cone shape which is also called Taylor cone. The thin thread of liquid emanating from the cone eventually fragments to form highly charged droplets.



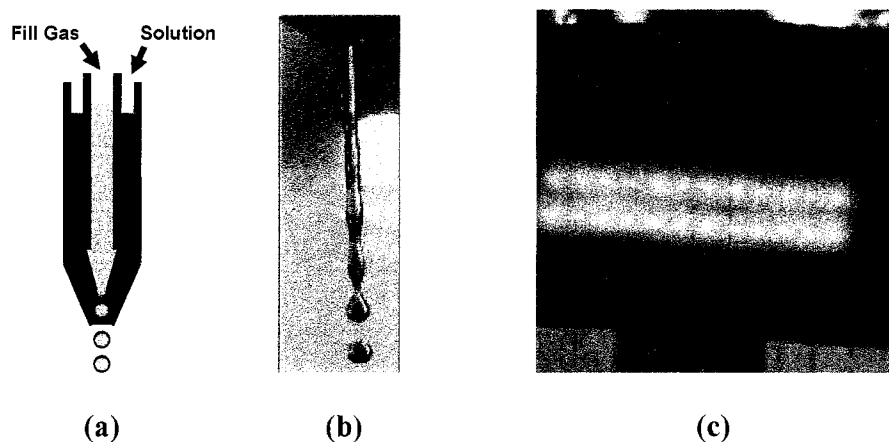


**Figure 1.3.** (a) Schematic of hollow microsphere generator using coaxial nozzle technique (redrawn from [52]), (b) droplet formation using the coaxial nozzle technology [80], (c) production of coffee oil-alginate capsules in a multi-nozzle unit with the vibration technology [80].

Loscertales *et al.* report a further development to the electro-spraying technique wherein coaxial jet of two immiscible fluids is generated via electro-hydrodynamic forces (Fig. 1.4). The liquid jet breaks up producing an aerosol of compound droplets ranging in size ranging from 150 nm to 10  $\mu\text{m}$  with controlled inner and outer shell thicknesses [81].

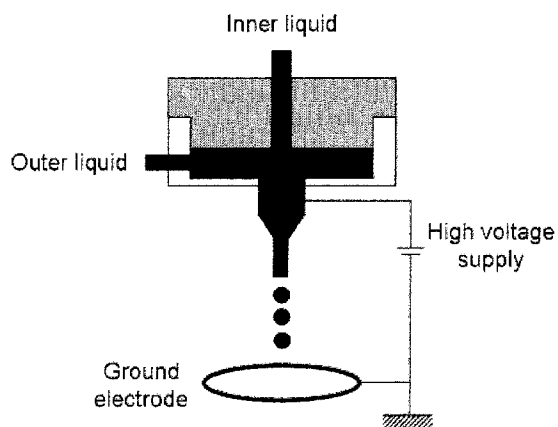


**Figure 1.4.** Experimental set-up for producing Taylor cone (redrawn from [81]).

In another approach of gas stripping of the droplet, the material of interest (generally polymers) is dissolved in a volatile solvent and passed through a needle orifice. This needle which is placed in a drying tower, is stripped with air or another gas. The droplets issuing from the needle forms an outer skin due to the evaporation of the solvent, which further develops into a shell [82]. One of the outstanding features of this technique in general is that the capsule size can be varied continuously over a wide range from hundreds of microns to tens of nanometer [83]. However, attaining encapsulation in well-defined size range, controlled thickness of the shell, and production of monodisperse spheres, all at the same time, is a challenge.

#### **1.2.4. Vesicles and liposomes**

Vesicles and liposomes are archetypal structures formed by thermodynamically driven self-assembly of amphiphilic lipid molecules. They can be synthesized in the size range of 50 nm to 50  $\mu\text{m}$ . The formation of these structures can be viewed as a two-step process. In the first step, the lipid molecules pack themselves to form bilayers and in the second step, these bilayers close upon themselves to form hollow spherical structures [84]. In addition to lipid molecules, vesicles have been synthesized using other building blocks such amphiphilic diblock copolymers [85-89], block polymers with rigid blocks [90-92], functionalized nanoparticles [93], and by molecules showing secondary interactions such as charge interactions, ligand binding, dipole interactions, and H-bonding [94-97]. The chemical, physical, and biological properties of vesicles can be tailored to specific applications by varying their block length, chemical structure, and even by functionalizing them with biological molecules. Vesicles are very promising in

terms of their encapsulation capabilities of both hydrophilic as well as hydrophobic compounds. The hydrophobic compounds are embedded in the bilayer while the hydrophilic substances are located within the core cavity [84]. Liposomes have been used commercially with the brand name Doxil® and Caelyx® to carry drugs such as doxorubicin. Vesicles and liposomes are not very physically stable and are susceptible to dissolution in the presence of high concentrations of surface active agents or when suspended in solvents other than in which they were formed originally. Upon drying, these structures tend to collapse, making it mandatory to handle them in the liquid state, a little cumbersome for certain application.

### **1.3. Research motivation and thesis layout**

Despite considerable advances in the field of nanoparticle assembly in general, and microcapsule synthesis in specific, there still exist challenges in controlling the final material properties such as size, polydispersity, shell thickness, encapsulation ability of hydrophilic and hydrophobic compound, encapsulation efficiency and loading, and putting these materials through the rigors of real-world applications. Successful future technologies will require improvements in ease of synthesis, low cost raw materials, facile encapsulation, and triggered release mechanisms. These are some of the design parameters that motivate my direction of research.

Scant attention has been paid to the interplay of Columbic charges as a route to assemble nanoparticles and polyelectrolytes into hollow spheres. Only recently, Wong *et al.* demonstrated a two-step assembly of gold and silica NPs into hollow spheres carried out at room temperature in aqueous conditions. The first step consisted of bringing the

Au NPs in contact with lysine-*b*-cysteine diblock copolymer which was observed to form globular structures (hypothesized to be due to Au NP-cysteine interaction), with the lysine block sticking out of the globule surface (Fig. 1.5) [98].

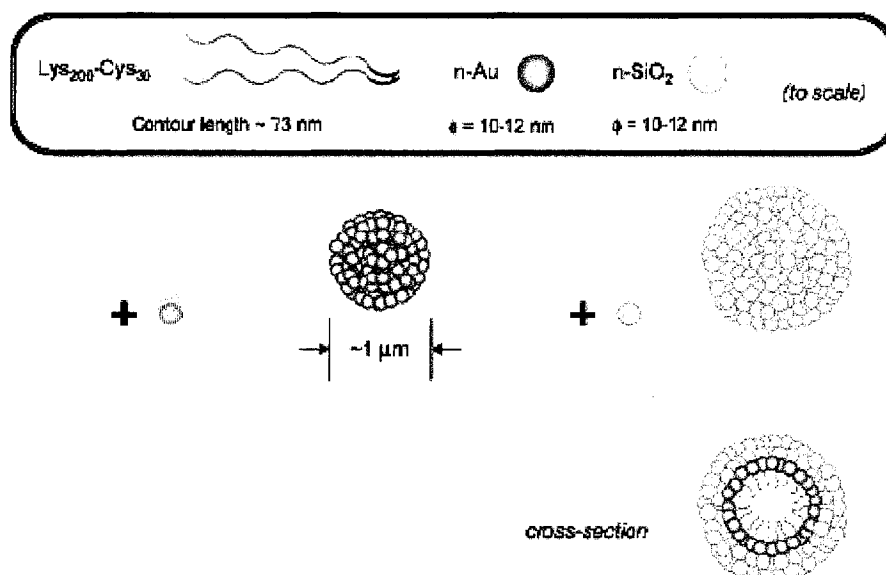


**Figure 1.5.** Schematic diagram depicting the hierarchical self-assembly of gold and silica nanoparticles into hollow spheres with a two layer structure. The addition of Au NP to the disulfide crosslinked block copolypeptide produced globules of gold particles. The introduction of silica NP then leads to the formation of hollow micron-sized spheres whose walls were composed of a distinct inner layer of Au NPs followed by an outer layer of silica NPs [98].

Upon the addition of silica NP, shell wall formation took place due to strong electrostatic interaction between the positively-charged lysine groups and negatively-charged silica NP. The final material were hollow spheres (Fig. 1.6) with the shell wall consisting of distinct layers of silica and Au NPs. The hollow cavity was created without the dissolution or volatilization of the core or by internal phase separation. This work involving simple mixing of different types of nanoparticles with appropriate polymers heralded a new and facile route to construct robust hollow spheres under benign synthesis conditions.

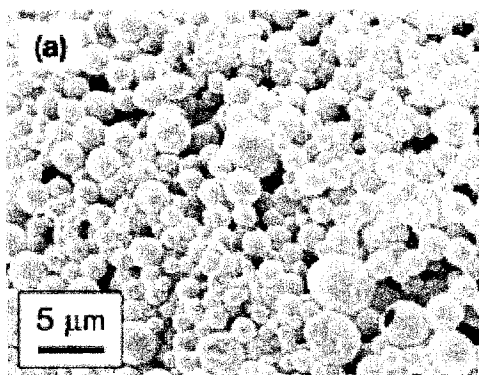


**Figure 1.6.** Scanning electron microscopy image of as-synthesized hollow spheres from poly(lysine-*b*-cysteine) copolymer, Au NPs, and SiO<sub>2</sub> NPs [98].

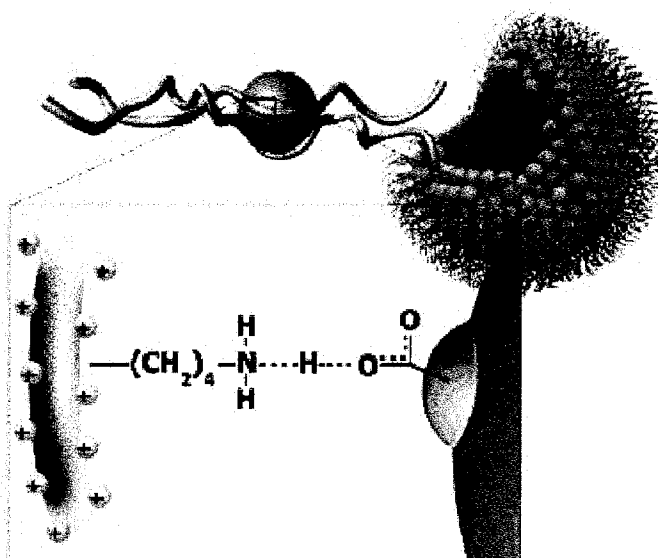


**Figure 1.7.** Schematic diagram of nanoparticle vesicles and the directional charge-stabilized hydrogen bonds that form between the amines of the poly(*L*-lysine) and the carboxylic acid group of the citrate stabilized quantum dots. The quantum dots formed the “oily” zone what extends into the exterior and interior water regions are portions of the poly(*L*-lysine) chains that are not coordinated with the carboxylic acid groups of the citrate-stabilized nanoparticles [99].

Following this, there were two more papers published by Stucky and coworkers with a similar concept albeit with different materials and target applications [99,100]. It was reported that NPs such as negatively charged citrate stabilized CdSe quantum dots

formed vesicular structures with homopolymer poly(*L*-lysine) through charge-stabilized hydrogen bonding (Fig. 1.7). These structures were used as templates to coat SiO<sub>2</sub> NPs to form hollow spheres.

My initial work focused on understanding better this two-step nanoparticle assembly mechanism. For our studies we chose poly(*L*-lysine) (PLL), Au NPs, and SiO<sub>2</sub> NPs as the system constituents. In Chapter 2, experimental results will be discussed to elucidate the interaction between cationic PLL and negatively charged Au NPs and SiO<sub>2</sub> NPs to form hollow microspheres. The hollow sphere formation was theorized to form through flocculation, in which the charge-driven aggregation of Au NPs by PLL provides the critical first step in the two-step synthesis process (“flocculation assembly”). This work was published in *Journal of the American Chemical Society* in 2004 [101].

It was discovered that simple multivalent anions (sulfate<sup>2-</sup>, citrate<sup>3-</sup>, EDTA<sup>4-</sup>, *etc.*) induce polyamines to form spherical aggregates in the (sub)micron size regime. In Chapter 3, the formation of these polymer-salt aggregates has been explained in terms of salt-bridge formation leading to a polymer network. Detailed studies to explain the formation and growth mechanism of polymer-salt aggregates have been performed by taking poly(allylamine) and citrate salt as the model compounds [102]. In addition, this chemistry has been shown to be a general one, meaning, a large variety of cationic polymers and multivalent salts exhibit this behavior [21]. These spherical aggregates could be used as templates to drive the assembly of negatively charged NPs to form a thick outer shell yielding robust nanoparticle-assembled capsules (NACs). The shell formation was understood *via* a penetration-deposition model. A variety of NPs have been used to create the shell wall. **We offer NP assembly as the easiest method to**

**synthesize stable capsule structures.** This work was published in *Advanced Materials* in 2005 [21]. A more detailed paper was recently submitted to *Journal of Physical Chemistry B* [102].

NACs allow facile encapsulation of water-soluble compounds such as drugs, dyes, and biomolecules. Chapter 4 presents results for encapsulation of a model protein, bovine serum albumin and a model enzyme, acid phosphatase. Upon mixing the enzyme solution with the polymer-salt aggregates, the enzyme molecules get immobilized within the aggregates. Subsequent deposition of NPs yields enzyme-containing NACs. Studies on enzyme loading and activity within the NACs have been performed, which will be submitted as an invited book chapter in the *ACS Symposium Series on Nanoscale Science and Technology in Biomolecular Catalysis*.

The aforementioned work was focused on studying the interaction between a single type of polyamine and different types of multivalent salts which lead to the formation of NACs with either hollow or uniformly polymer-filled cores. In Chapter 5, we disclose a very interesting phenomenon wherein a mixture of polyamines microphase segregate upon interacting with multivalent salts leading to polymer-salt aggregates having anisotropic interior. The morphology of these aggregates can be locked-in by adding SiO<sub>2</sub> NPs or silicic acid resulting in hollow NACs or solid microspheres, respectively, with “patchy” surfaces and anisotropic cores. These inhomogeneous particles pave the way for spatio-selective multi-functionalization of particles. Manuscript is in preparation for submitting to *Advanced Materials* journal.

## 1.4. References

- [1] Mirkin, C.A., Letsinger, R.L., Mucic, R.C., Storhoff, J.J. A DNA-based method for rationally assembling nanoparticles into macroscopic materials *Nature*, **1996**, 382, 607.
- [2] Mirkin, C.A. Programming the assembly of two- and three-dimensional architectures with DNA and nanoscale inorganic building blocks *Inorganic Chemistry*, **2000**, 39, 2258.
- [3] Niemeyer, C.M., Adler, M., Gao, S., Chi, L.F. Supramolecular nanocircles consisting of streptavidin and DNA *Angewandte Chemie-International Edition*, **2000**, 39, 3055.
- [4] Collier, C.P., Vossmeier, T., Heath, J.R. Nanocrystal superlattices *Annual Review of Physical Chemistry*, **1998**, 49, 371.
- [5] Shipway, A.N., Katz, E., Willner, I. Nanoparticle arrays on surfaces for electronic, optical, and sensor applications *ChemPhysChem*, **2000**, 1, 18.
- [6] Murray, C.B., Kagan, C.R., Bawendi, M.G. Self-organization of CdSe nanocrystallites into three-dimensional quantum dot superlattices *Science*, **1995**, 270, 1335.
- [7] Liz-Marzan, L.M., Norris, D.J., Bawendi, M.G., Betley, T., Doyle, H., Guyot-Sionnest, P., Klimov, V.I., Kotov, N.A., Mulvaney, P., Murray, C.B., Schiffrin, D.J., Shim, M., Sun, S., Wang, C. New aspects of nanocrystal research *MRS Bulletin*, **2001**, 26, 981.
- [8] Kotov, N.A. Ordered layered assemblies of nanoparticles *MRS Bulletin*, **2001**, 26, 992.
- [9] Caruso, F., Caruso, R.A., Mohwald, H. Nanoengineering of inorganic and hybrid hollow spheres by colloidal templating *Science*, **1998**, 282, 1111.
- [10] Alivisatos, A.P., Johnsson, K.P., Peng, X.G., Wilson, T.E., Loweth, C.J., Bruchez, M.P., Schultz, P.G. Organization of 'nanocrystal molecules' using DNA *Nature*, **1996**, 382, 609.



- [11] Fan, H., Yang, K., Boye, D., Sigmon, T., Malloy, K., Xu, H., Lopez, G., Brinker, C.J. Self-assembly of ordered, robust, three-dimensional gold nanocrystal/silica arrays *Science*, **2004**, *304*, 567.
- [12] Dumestre, F., Chaudret, B., Amiens, C., Renaud, P., Fejes, P. Superlattices of iron nanocubes synthesized from  $\text{Fe}[\text{N}(\text{SiMe}_3)(2)](2)$  *Science*, **2004**, *303*, 821.
- [13] Tang, Z., Kotov, N.A., Giersig, M. Spontaneous organization of single CdTe nanoparticles into luminescent nanowires *Science*, **2002**, *297*, 237.
- [14] Huang, Y., Duan, X., Wei, Q., Lieber, C.M. Directed assembly of one-dimensional nanostructures into functional networks *Science*, **2001**, *291*, 630.
- [15] Schlittler, R.R., Seo, J.W., Gimzewski, J.K., Durkan, C., Saifullah, M.S.M., Welland, M.E. Single crystals of single-walled carbon nanotubes formed by self-assembly *Science*, **2001**, *292*, 1136.
- [16] Cui, Y., Lieber, C.M. Functional nanoscale electronic devices assembled using silicon nanowire building blocks *Science*, **2001**, *291*, 851.
- [17] Huang, Y., Duan, X., Cui, Y., Lauhon, L., Kim, K.-H., Lieber, C.M. Logic gates and computation from assembled nanowire building blocks *Science*, **2001**, *294*, 1313.
- [18] Shevchenko, E.V., Talapin, D.V., Kotov, N.A., O'Brien, S., Murray, C.B. Structural diversity in binary nanoparticle superlattices *Nature*, **2006**, *439*, 55.
- [19] Sharma, J., Chhabra, R., Liu, Y., Ke, Y., Yan, H. DNA-templated self-assembly of two-dimensional and periodical gold nanoparticle arrays *Angewandte Chemie-International Edition*, **2006**, *45*, 730.
- [20] Huang, Y., Chaing, C.-Y., Lee, S.K., Gao, Y., Hu, E.L., Yoreo, J.D., Belcher, A.M. Programmable assembly of nanoarchitectures using genetically engineered viruses *Nano Letters*, **2005**, *5*, 1429.
- [21] Rana, R.K., Murthy, V.S., Yu, J., Wong, M.S. Nanoparticle self-assembly of hierarchically ordered microcapsule structures *Advanced Materials*, **2005**, *17*, 1145.

- [22] Shenhar, R., Norsten, T.B., Rotello, V.M. Polymer-mediated nanoparticle assembly: Structural control and applications *Advanced Materials*, **2005**, *17*, 657.
- [23] Boal, A.K., Rotello, V.M. Redox-modulated recognition of flavin by functionalized gold nanoparticles *Journal of the American Chemical Society*, **1999**, *121*, 4914.
- [24] Boal, A.K., Ilhan, F., DeRouchey, J.E., Thurn-Albrecht, T., Russel, T.P., Rotello, V.M. Self-assembly of nanoparticles into structured spherical and network aggregates *Nature*, **2000**, *404*, 746.
- [25] Niemeyer, C.M. Nanoparticles, proteins, and nucleic acids: Biotechnology meets materials science *Angewandte Chemie-International Edition*, **2001**, *40*, 4128.
- [26] Shenton, W., Davis, S.A., Mann, S. Directed self-assembly of nanoparticles into macroscopic materials using antibody-antigen recognition *Advanced Materials*, **1999**, *11*, 449.
- [27] Mucic, R.C., Storhoff, J.J., Mirkin, C.A., Letsinger, R.L. DNA-directed synthesis of binary nanoparticle network materials *Journal of the American Chemical Society*, **1998**, *120*, 12674.
- [28] Lu, X., Hanrath, T., Johnston, K.P., Korgel, B.A. Growth of single crystal silicon nanowires in supercritical solution from tethered gold particles on a silicon substrate *Nano Letters*, **2003**, *3*, 93.
- [29] Hanrath, T., Korgel, B.A. Nucleation and growth of germanium nanowires seeded by organic monolayer-coated gold nanocrystals *Journal of the American Chemical Society*, **2002**, *124*, 1424.
- [30] Korgel, B.A., Fullam, S., Connolly, S., Fitzmaurice, D. Assembly and self-organization of silver nanocrystal superlattices *Journal of Physical Chemistry B*, **1998**, *102*, 8379.
- [31] Rengarajan, R., Jiang, P., Larrabee, D.C., Colvin, V.L., Mittleman, D.M. Colloidal photonic superlattices *Physical Review B*, **2001**, *64*, 20513.
- [32] Zeng, H., Li, J., Liu, J.P., Wang, Z.L., Sun, S. Exchange-coupled nanocomposite magnets by nanoparticle self-assembly *Nature*, **2002**, *420*, 395.

- [33] Hermanson, K.D., Lumsdon, S.O., Williams, J.P., Kaler, E.W., Velev, O.D. Dielectrophoretic assembly of electrically functional microwires from nanoparticle suspensions *Science*, **2001**, 294, 1082.
- [34] Decher, G. Fuzzy nanoassemblies: Toward layered polymeric multicomposites *Science*, **1997**, 271, 993.
- [35] Alivisatos, A.P. Semiconductor clusters, nanocrystals, and quantum dots *Science*, **1996**, 271, 933.
- [36] Storhoff, J.J., Lazarides, A.A., Mucic, R.C., Mirkin, C.A., Letsinger, R.L., Schatz, G.C. What controls the optical properties of DNA-linked gold nanoparticle assemblies *Journal of the American Chemical Society*, **2000**, 122, 4640.
- [37] Elghanian, R., Storhoff, J.J., Mucic, R.C., Letsinger, R.L., Mirkin, C.A. Selective colorimetric detection of polynucleotides based on the distance-dependent optical properties of gold nanoparticles *Science*, **1997**, 277, 1078.
- [38] Demers, L.M., Ostblom, M., Zhang, H., Jang, N., Lieberg, B., Mirkin, C.A. Thermal desorption behaviour and binding properties of DNA bases and nucleosides on gold *Journal of the American Chemical Society*, **2002**, 124, 11248.
- [39] Storhoff, J.J., Elghanian, R., Mucic, R.C., Mirkin, C.A., Letsinger, R.L. Sequence-dependent stability of DNA-modified gold nanoparticles *Langmuir*, **2002**, 18, 6666.
- [40] Storhoff, J.J., Elghanian, R., Mucic, R.C., Mirkin, C.A., Letsinger, R.L. One-pot colorimetric differentiation of polynucleotides with single base imperfections using gold nanoparticle probes *Journal of the American Chemical Society*, **1998**, 120, 1959.
- [41] Mann, S., Shenton, W., Li, M., Connolly, S., Fitzmaurice, D. Biologically programed nanoparticle assembly *Advanced Materials*, **2000**, 12, 147.
- [42] Li, M., Wong, K.W., Mann, S. Organization of inorganic nanoparticles using biotin-streptavidin connectors *Chemistry of Materials*, **1999**, 11, 23.

- [43] Caruso, F., Shi, X.Y., Caruso, R.A., Susa, A. Hollow titania spheres from layered precursor deposition on sacrificial colloidal core particles *Advanced Materials*, **2001**, *13*, 740.
- [44] Huang, H., Remsen, E.E., Kowalewski, T., Wooley, K.L. Nanocages derived from shell cross-linked micelle templates *Journal of the American Chemical Society*, **1999**, *121*, 3805.
- [45] Hotz, J., Meier, W. Vesicle-templated polymer hollow spheres *Langmuir*, **1998**, *14*, 1031.
- [46] Fowler, C.E., Shenton, W., Stubbs, G., Mann, S. Tobacco mosaic virus liquid crystals as templates for the interior design of silica mesophases and nanoparticles *Advanced Materials*, **2001**, *13*, 1266.
- [47] Zoltesi, C.I., Imhof, A. Synthesis of monodisperse colloidal spheres, capsules, and microballoons by emulsion templating *Advanced Materials*, **2005**, *17*, 924.
- [48] Maya, L., Muralidharan, G., Thundat, T.G., Kenik, E.A. Polymer-mediated assembly of gold nanoclusters *Langmuir*, **2000**, *16*, 9151.
- [49] Dinsmore, A.D., Hsu, M.F., Nikolaides, M.G., Marquez, M., Bausch, A.R., Weitz, D.A. Colloidosomes: Selectively permeable capsules composed of colloidal particles *Science*, **2002**, *298*, 1006.
- [50] Hsu, M.F., Nikolaides, M.G., Dinsmore, A.D., Bausch, A.R., Gordon, V.D., Chen, X., Hutchinson, J.W., Weitz, D.A. Self-assembled shells composed of colloidal particles: Fabrication and Characterization *Langmuir*, **2005**, *21*, 2963.
- [51] Philippot, J.R., Schuber, F. *Liposomes as Tools in Basic Research and Industry*; CRC Press: Boca Raton, **1995**.
- [52] Wilcox, D.L., Sr., Berg, M., Bernat, T., Kellerman, D., Cochran, J.K., Jr. *Hollow and Solid Spheres and Microspheres: Science and Technology Associated with Their Fabrication and Application*; Materials Research Society: Pittsburgh, **1995**.
- [53] Gibbs, B.F., Kermasha, S., Alli, I., Mulligan, C.N. Encapsulation in the food industry: A review *International Journal of Food Science and Nutrition*, **1999**, *50*, 213.

- [54] Uludag, H., De Vos, P., Tresco, P.A. Technology of mammalian cell encapsulation *Advanced Drug Delivery Reviews*, **2000**, 42, 29.
- [55] Barenholz, Y. Liposome application: Problems and prospects *Current Opinion in Colloid and Interface Science*, **2001**, 6, 66.
- [56] Caruso, F. Nanoengineering of particle surfaces *Advanced Materials*, **2001**, 13, 11.
- [57] Chah, S., Fendler, J.H., Yi, J. Nanostructured gold hollow microspheres prepared on dissolvable ceramic hollow sphere templates *Journal of Colloid and Interface Science*, **2002**, 250, 142.
- [58] Yang, M., Ma, J., Zhang, C., Yang, Z., Lu, Y. General synthetic route toward functional hollow spheres with double-shelled structures *Angewandte Chemie-International Edition*, **2005**, 44, 6727.
- [59] Miller, R.E., Brown, R.W. Pressure-sensitive record material, Appleton Papers, Inc., United States Patent 4,675,706, **1987**.
- [60] Arshady, R. *Microspheres, Microcapsules & Liposomes - Preparation & Chemical Applications*; Citus: London, **2003**.
- [61] Southwest Research Institute ([www.swri.edu](http://www.swri.edu))
- [62] Caruso, F., Spasnova, M., Saigueirino-Maceira, V., Liz-Marzan, L.M. Multilayer assemblies of silica-encapsulated gold nanoparticles on decomposable colloid templates *Advanced Materials*, **2001**, 13, 1090.
- [63] Wang, Y.J., Yu, A.M., Caruso, F. Nanoporous polyelectrolyte spheres prepared by sequentially coating sacrificial mesoporous silica spheres *Angewandte Chemie-International Edition*, **2005**, 44, 2888.
- [64] Caruso, F., Antonietti, M. Sol-gel nanocoating: An approach to the preparation of structured materials *Chemistry of Materials*, **2001**, 13, 3272.

- [65] Kawahashi, N., Matijevic, E. Preparation and properties of uniform coated colloidal particles: V. Yttrium basic carbonate on polystyrene latex *Journal of Colloid and Interface Science*, **1990**, *138*, 534.
- [66] Zhong, Z.Y., Yin, Y.D., Gates, B., Xia, Y.N. Preparation of mesoscale hollow spheres of TiO<sub>2</sub> and SnO<sub>2</sub> by templating against crystalline arrays of polystyrene beads *Advanced Materials*, **2000**, *12*, 206.
- [67] Liu, S., Zhang, Z., Han, M.-Y. Nanometer-sized gold-loaded gelatin/silica nanocapsules *Advanced Materials*, **2005**, *17*, 1862.
- [68] McKelvey, C.A., Kaler, E.W., Zasadzinski, J.A., Coldren, B., Jung, H.T. Templating hollow polymeric spheres from catanionic equilibrium vesicles: Synthesis and characterization *Langmuir*, **2000**, *16*, 8285.
- [69] Kawahashi, N., Matijevic, E. Preparation of hollow spherical particles of yttrium compounds *Journal of Colloid and Interface Science*, **1991**, *143*, 103.
- [70] Schacht, S., Huo, Q., Martin-Voigt, I., Stucky, G.D., Schuth, F. Oil-water interface templating of mesoporous macroscale structures *Science*, **1996**, *273*, 768.
- [71] Marinakos, S.M., Novak, J.P., Brousseau, L.C., House, A.B., Edeki, E.M., Feldhaus, J.C., Feldheim, D.L. Gold particles as templates for the synthesis of hollow polymer capsules. Control of capsule dimensions and guest encapsulation *Journal of the American Chemical Society*, **1999**, *121*, 8518.
- [72] Jiang, P., Bertone, J.F., Colvin, V.L. A lost-wax approach to monodisperse colloids and their crystals *Science*, **2001**, *291*, 453.
- [73] Schmidt, H.T., Ostafin, A.E. Liposome directed growth of calcium phosphate nanoshells *Advanced Materials*, **2002**, *14*, 532.
- [74] Jain, R.A. The manufacturing techniques of various drug loaded biodegradable poly(lactide-co-glycolide) (PLGA) devices *Biomaterials*, **2000**, *21*, 2475.
- [75] Dowding, P.J., Atkin, R., Vincent, B., Bouillot, P. Oil core-polymer shell microcapsules prepared by internal phase separation from emulsion droplets. I:

Characterization and release rates for microcapsules with polystyrene shells *Langmuir*, **2004**, *20*, 11374.

- [76] Dowding, P.J., Atkin, R., Vincent, B., Bouillot, P. Oil core/polymer shell microcapsules by internal phase separation from emulsion droplets. II: Controlling the release profile of active molecules *Langmuir*, **2005**, *21*, 5278.
- [77] Loxley, A., Vincent, B. Preparation of poly(methylmethacrylate) microcapsules with liquid cores *Journal of Colloid and Interface Science*, **1998**, *208*, 49.
- [78] Arshady, R. Preparation of biodegradable microspheres and microcapsules. II: Polylactides and related polyesters *Journal of Controlled Release*, **1991**, *17*, 1.
- [79] Jalil, R., Nixon, J.R. Biodegradable poly(lactic acid) and poly(lactic-co-glycolide) microcapsules: Problems associated with preparative technique and release properties *Journal of Microencapsulation*, **1990**, *7*, 297.
- [80] Pathtech Pty. Ltd. ([www.pathtech.com.au](http://www.pathtech.com.au))
- [81] Loscertales, I.G., Barrero, A., Guerrero, I., Cortijo, R., Marquez, M., Ganan-Calvo, A.M. Micro/nano encapsulation via electrified coaxial liquid jets *Science*, **2002**, *295*, 1695.
- [82] Burnham, A.K., Grens, J.Z., Lilley, E.M. Fabrication of polyvinyl alcohol coated polystyrene shells *Journal of Vacuum Science and Technology A*, **1987**, *5*, 3417.
- [83] Gañán-Calvo, A.M., Dávila, J., Barrero, A. Current and droplet size in the electrospraying of liquids. Scaling laws *Journal of Aerosol Science*, **1997**, *28*, 249.
- [84] Antonietti, M., Forster, S. Vesicles and liposomes: A self-assembly principle beyond lipids *Advanced Materials*, **2003**, *15*, 1323.
- [85] Zhang, L.F., Eisenberg, A. Multiple morphologies of crew-cut aggregates of polystyrene-*b*-poly(acrylic acid) block copolymers *Science*, **1995**, *268*, 1728.
- [86] Zhang, L.F., Yu, K., Eisenberg, A. Ion-induced morphological changes in "crew-cut" aggregates of amphiphilic block copolymers *Science*, **1996**, *272*, 1777.

- [87] Discher, B.M., Won, Y.-Y., Ege, D.S., Lee, J.C.-M., Bates, F.S., Discher, D.E., Hammer, D.A. Polymersomes: Tough vesicles made from diblock copolymers *Science*, **1999**, *284*, 1143.
- [88] Schillen, K., Bryskhe, K., Mel'nikova, Y.S. Vesicles formed from a poly(ethylene oxide)-poly(propylene oxide)-poly(ethylene oxide) triblock copolymer in dilute aqueous solution *Macromolecules*, **1999**, *32*, 6885.
- [89] Nardin, C., Hirt, T., Leukel, J., Meier, W. Polymerized ABA triblock copolymer vesicles *Langmuir*, **2000**, *16*, 1035.
- [90] Jenekhe, S.A., Chen, X.L. Self-assembled aggregates of rod-coil block copolymers and their solubilization and encapsulation of fullerenes *Science*, **1998**, *279*, 1903.
- [91] Jenekhe, S.A., Chen, X.L. Self-assembly of ordered microporous materials from rod-coil block copolymers *Science*, **1999**, *283*, 372.
- [92] Holder, S.J., Hiorns, R.C., Sommerdijk, N.A.J.M., Williams, S.J., Jones, R.G., Nolte, R.J.M. The first example of a poly(ethylene oxide) poly(methylphenylsilane) amphiphilic block copolymer: vesicle formation in water *Chemical Communication*, **1998**, *14*, 1445.
- [93] Zhou, S.Q., Burger, C., Chu, B., Sawamura, M., Nagahama, N., Toganoh, M., Hackler, U.E., Isobe, H., Nakamura, E. Spherical bilayer vesicles of fullerene-based surfactants in water: A laser light scattering study *Science*, **2001**, *291*, 1944.
- [94] Stoenescu, R., Meier, W. Vesicles with asymmetric membranes from amphiphilic ABC triblock copolymers *Chemical Communication*, **2002**, *24*, 3016.
- [95] Kaler, E.W., Murthy, A.K., Rodriguez, B.E., Zasadzinski, J.A.N. Spontaneous vesicle formation in aqueous mixtures of single-tailed surfactants *Science*, **1989**, *245*, 1371.
- [96] zu Putlitz, B., Landfester, K., Forster, S., Antonietti, M. Vesicle-forming single-tail hydrocarbon surfactants with sulfonium headgroup *Langmuir*, **2000**, *16*, 3003.



- [97] Schrage, S., Sigel, R., Schlaad, H. Formation of amphiphilic polyion complex vesicles from mixtures of oppositely charged block ionomers *Macromolecules*, **2003**, *36*, 1417.
- [98] Wong, M.S., Cha, J.N., Choi, K.S., Deming, T.J., Stucky, G.D. Assembly of nanoparticles into hollow spheres using block copolypeptides *Nano Letters*, **2002**, *2*, 583.
- [99] Cha, J.N., Birkedal, H., Euliss, L.E., Bartl, M.H., Wong, M.S., Deming, T.J., Stucky, G.D. Spontaneous formation of nanoparticle vesicles from homopolymer polyelectrolytes *Journal of the American Chemical Society*, **2003**, *125*, 8285.
- [100] Cha, J.N., Bartl, M.H., Wong, M.S., Popitsch, A., Deming, T.J., Stucky, G.D. Microcavity lasing from block peptide hierarchically assembled quantum dot spherical resonators *Nano Letters*, **2003**, *3*, 907.
- [101] Murthy, V.S., Cha, J.N., Stucky, G.D., Wong, M.S. Charge-driven flocculation of poly(L-lysine)-gold nanoparticle assemblies leading to hollow microspheres *Journal of the American Chemical Society*, **2004**, *126*, 5292.
- [102] Murthy, V.S., Rana, R.K., Wong, M.S. Nanoparticle-assembled capsule synthesis: Formation of colloidal polyamine-salt intermediates *Journal of Physical Chemistry B*, **2006**, submitted.

## Chapter 2. Hollow microspheres from flocculation assembly of gold and silica nanoparticles\*

### 2.1. Introduction

There has been a revived interest in the synthesis of inorganic hollow microspheres (submicron and micron diameters) for potential use in therapeutic, storage, and catalytic applications [1-5]. Various chemical approaches to inorganic hollow sphere fabrication can be broadly classified into (1) sacrificial core method [1,6,7] and (2) interfacial synthesis [8,9], in which the inorganic (or organic) shell can be considered to form around a solid or liquid core, respectively. These approaches can involve multiple steps and severe synthesis conditions in the formation of the shell and requires the removal of the sacrificial core after shell formation. By comparison, organic hollow spheres such as vesicles [10-12], “knedels,” [13,14] and “polymersomes” [15] are formed more easily from the self-assembly of amphiphilic molecules, but they are generally less stable and smaller in size.

Notable examples of hollow spheres composed of nanoparticles (NPs) have been reported recently. The layer-by-layer assembly of NPs into hollow microspheres was shown to be a versatile preparation route by Caruso and co-workers; the thin shell wall tended to deform and collapse after removal of the sacrificial latex core in many cases, though [16-19]. SiO<sub>2</sub> NPs were used to coat and stabilize micrometer-sized oil droplets by Binks and co-workers [20]. These structures are not stable after removal of the oil core because the shell wall is too thin and the NPs are not bound together. Crosslinking the particles was shown to be a successful method for a stable hollow sphere structure, in the

---

\* Murthy, V.S.; Cha, J.N.; Stucky, G.D.; Wong, M.S. *J. Am. Chem. Soc.*, **2004**, 126, 5292-5299.

case where latex microparticles were adsorbed around the water droplets and slightly sintered together (to form “colloidosomes”) [9].

Wong *et al.* recently reported on the synthesis of inorganic NP-based hollow spheres under ambient conditions and without a sacrificial template [21]. Silica/gold hollow spheres were generated through the formation of Au NP-poly(*L*-lysine-*b*-*L*-cysteine) copolymer aggregates and their subsequent encasement within a shell composed of SiO<sub>2</sub> NPs. It was proposed that Au NPs reacted with the poly(*L*-cysteine) block to form gold-thiolate covalent bonds and that negatively charged SiO<sub>2</sub> NPs interacted electrostatically with the positively charged poly(*L*-lysine). It was found that the synthesis chemistry permitted the formation of silica hollow spheres containing silver NPs [21] and CdSe/CdS quantum dots [22]. For the latter material, it was suggested that electrostatic interactions contributed significantly to the formation of quantum dot-poly(*L*-lysine-*b*-*L*-cysteine) copolymer aggregates. Stucky and coworkers subsequently found that poly(*L*-lysine) formed hollow spheres with quantum dots and SiO<sub>2</sub> NPs without the poly(*L*-cysteine) block; they hypothesized the formation of quantum dots/PLL vesicle structures as the intermediate precursor to the hollow spheres [23]. In this chapter, we provide new results indicating that the formation of NP-based hollow spheres may be described as a type of flocculation of NPs by charged polymers.

The phenomenon of particle flocculation as a route to functional materials has not been emphasized thus far. Flocculation is generally a random process in which polyelectrolytes bind non-selectively and non-directionally to oppositely-charged particles. Charge neutralization and formation of inter-particle polymer bridges are identified as the two key mechanistic steps involved in flocculation [24], but the lack of

spatial and directional control of the binding and bridging results in randomly structured, fractal-like particle/polymer precipitate [25-27]. Flocculation of (sub-micron to micron sized, 100's–1000's nm) particles has been studied over the last fifty years and has seen applications in refining mineral ores, paper manufacture, water remediation, food industry, and pharmaceuticals, for example. Extensive experimental and theoretical work continues today to understand better the kinetics of flocculation and the internal structure of the flocculent material (e.g., floc size distribution and interparticle distances), particularly for NPs (<100 nm) [28-30]. A better understanding and control of the flocculation process would ultimately be needed to construct NP-based flocculated materials of controlled structure.

In this chapter, we report the formation of spherical, submicron flocs of Au NPs and poly(*L*-lysine) (PLL), and demonstrate that the gold-thiolate bonds proposed for the poly(*L*-lysine-*b*-*L*-cysteine) copolymer system is not required in the synthesis of hollow microspheres. We investigate the unusual aggregation properties of Au NPs with PLL through confocal microscopy and dynamic light scattering, and discuss their effect on the hollow sphere structure resulting from shell formation.

## **2.2. Experimental section**

### **2.2.1. Materials**

Poly(*L*-lysine) (PLL) was procured as a hydrogen bromide salt (Sigma-Aldrich) and was used as-received. PLL1 and PLL2 are polymers with two different lengths, and PLL3 is a longer polymer covalently conjugated to fluorescein isothiocyanate (FITC) through

the  $\epsilon$ -amino group (Table 2.1). Starting polymer solutions (2 mg/ml) were prepared with 18.2 M $\Omega$  deionised water and kept refrigerated when not in use (pH  $\sim$  6.2).

**Table 2.1.** List of various poly-*L*-lysines used for experiments along with their size and polydispersity information.

Poly- <i>L</i> -Lysine	Molecular Weight, kD <sup>a</sup>	Dispersity Index, $M_w/M_n$ <sup>a</sup>	Contour Length, nm	Hydrodynamic Diameter, nm <sup>b</sup>
PLL1	27.4	1.3	$\sim$ 49	$\sim$ 30
PLL2	57.9	1.15	$\sim$ 104	$\sim$ 45
PLL3 <sup>c</sup>	68.6	NA	$\sim$ 123	NA

<sup>a</sup> Data provided by the supplier

<sup>b</sup> Measured by dynamic light scattering

<sup>c</sup> FITC content: 0.006 mol/(mol lysine unit), reported by supplier

Au NPs were synthesized through the citrate reduction method [31,32]. The NPs were  $14 \pm 2$  nm in diameter as characterized by transmission electron microscopy and dynamic light scattering. The number concentration of the stock colloidal sol (pH  $\sim$  7.0) was estimated from the optical density at the plasmon resonance frequency (520 nm) using an extinction coefficient of  $2.4 \times 10^8$  M<sup>-1</sup>cm<sup>-1</sup>; an optical density value of 1.064 gave a concentration of  $4.43 \times 10^{-9}$  M ( $2.67 \times 10^{12}$  NP/ml) [33]. SiO<sub>2</sub> NPs (Snowtex O, Nissan Chemicals) were supplied as a colloidal sol (20.4 wt % solids, pH 3.4); the number concentration was calculated to be  $1.14 \times 10^{17}$  NP/ml. These NPs measured  $13 \pm 3$  nm in diameter as characterized by dynamic light scattering. The zeta ( $\zeta$ ) potentials of Au and SiO<sub>2</sub> NPs were calculated from their electrophoretic mobility (measured in their native solution) using Henry's equation [34], respectively (Table 2.2). The value for the Au NP zeta potential is underestimated [35], but does not affect the conclusions of our work.

**Table 2.2** List of nanoparticles used for experiments.

Nanoparticle	Hydrodynamic Diameter, nm	Zeta Potential, mV	Concentration, particles/ml
<b>Au NP</b>	14 ± 2	- 45.26	2.67 X 10 <sup>12</sup>
<b>SiO<sub>2</sub> NP</b>	13 ± 3	- 15.65	1.14 X 10 <sup>17</sup>

### 2.2.2. Synthesis

The synthesis of SiO<sub>2</sub>/Au NP-based hollow spheres is accomplished in two steps, similar to that described by Wong *et al.* [21]. 125 µl of the Au colloidal sol was micropipetted into a 1.5 ml microcentrifuge test tube that contained 21 µl of a PLL solution (2 mg/ml). The synthesis mixture was agitated at low speed (“4” speed on a 1–10 scale) for 10 seconds using a vortex mixer (Fisher Scientific), to provide thorough and rapid homogenization and mixing of the Au NP-PLL suspension. To this suspension, 125 µl of SiO<sub>2</sub> sol was added immediately and vigorously vortex-mixed (“8” speed) for 20 seconds, resulting in water-containing microspheres. The final pH of the synthesis mixture was measured to be 4.9.

For the hollow sphere size control experiments, the floc suspension was left to stand for 3 min, 20 min, or 2 hr before the SiO<sub>2</sub> sol was added.

For studying the pH effect on the hollow sphere structure, the as-prepared sphere suspension (pH ~ 4.9) was acidified by adding 40 µl of 1 N HCl and vortex-mixed at “8” speed for 10 seconds (final pH ~ 0.5). The cloudy suspension turned clear. It was then combined with 60 µl of 1 N NaOH and vortex-mixed at “8” speed for 10 seconds (final pH ~ 10), with the suspension turning cloudy again.

### 2.2.3. Characterization

**Confocal Laser Scanning Microscopy.** Confocal images were captured with Carl Zeiss LSM 410 inverted microscope equipped with a 100× oil immersion objective (NA = 1.4). The laser excitation wavelength of 488 nm was chosen for FITC ( $\lambda_{\text{ex}} = 494.5$  nm,  $\lambda_{\text{em}} = 519$  nm). Samples were mounted on conventional glass slides and sealed under a cover slip to prevent drying. All samples were prepared 1–2 hrs prior to imaging.

**Image Processing.** A freely available NIH image processing software called “*ImageJ*” [36] was used for calculating the line intensity profile across the sphere. Also, the size distribution of spheres (>300 spheres were analyzed for each sample) from confocal microscopy images was measured with this software. Adobe Photoshop V6.0 was used to enhance the images; it was ensured that there was no loss of information or incorporation of any image processing artifacts.

**Dynamic Light Scattering.** Size distribution and zeta potential analysis were carried out with Brookhaven ZetaPALS dynamic light scattering (DLS) equipment with BI-9000AT digital autocorrelator at 656 nm wavelength. All studies were done at a 90° scattering angle and temperature controlled at 25 °C; standard 50  $\mu$ l cuvettes were used for size distribution analysis. Two types of size analysis studies were performed in this work. Time-averaged particle size distributions were collected over an analysis time of at least 15 min using the software package “*9KDLSW*.” For studying the evolution of Au NP–PLL flocs with time, time dependent size measurements were taken of Au NP–PLL floc suspensions immediately after vortex mixing, at 1-minute intervals using the software package “*9KPSDW*.” Measurements of Au NP–PLL flocs started three minutes

after the 10-second vortex mixing (the three-minute time gap was due to transferring the suspension from the synthesis vial to the DLS cuvette and parameter set-up).

**Zeta Potential Analysis.** Zeta potentials were calculated using phase analysis light scattering (PALS), a variation of electrophoretic dynamic light scattering (DLS) [37], from electrophoretic mobility measurements using Henry's equation [34] (i.e.,  $0.1 \leq \kappa a \leq 100$ , where  $\kappa$  is the Debye-Hückel parameter and  $a$  is the particle radius). A dip-in (Uzgiris type) electrode system [38] with 4 ml polystyrene cuvettes was used.

**Fluorescence Spectroscopy.** Fluorescence measurements were taken with Jobin-Yvon Horiba Fluoromax 3 spectrophotometer. Standard quartz cells with a path length of 1 cm were used. Solutions were constantly stirred during analysis with a magnetic Teflon bar; it was verified that the stirring did not contribute to any interference in the fluorescence spectrum.

**UV-Vis Spectroscopy.** Absorption spectroscopy was carried out in Shimadzu 2401-PC UV-Vis spectrophotometer to characterize the Au NP. Standard quartz cuvettes with a path length of 1 cm were used.

**Coulter Counter.** Sphere size distribution was measured with a Beckman Coulter counter having an orifice diameter of 50  $\mu\text{m}$ . The lower limit for measuring sizes for this equipment was 1  $\mu\text{m}$ . 10  $\mu\text{l}$  of a hollow sphere suspension (as synthesized) was diluted in 10 ml of aqueous Isotone solution (composition: 7.93g/l NaCl, 0.38g/l  $\text{Na}_2\text{EDTA}$ , 0.40g/l KCl, 0.19g/l  $\text{H}_2\text{NaPO}_4$ , 1.95g/l  $\text{HNa}_2\text{PO}_4$ , 0.30g/l NaF; Beckman Coulter).

**Scanning Electron Microscopy.** Scanning electron microscopy (SEM) was carried out in JEOL6500 field emission microscope equipped with in-lens thermal field emission electron gun. Secondary electron image (SEI) was taken at 15 kV electron beam with a



working distance of 10 mm. The microsphere suspension was aged for two days, washed with Isotone solution, and suspended in isopropanol before being loaded and air-dried onto carbon tape for imaging.

**Transmission Electron Microscopy.** Transmission electron microscopy was performed on JEOL2010 FasTEM system at 100 kV electron beam accelerating voltage. Microspheres aged for two days were washed with Isotone solution, suspended in isopropanol, and loaded on a 200 mesh copper grid.

## 2.3. Results and discussions

We first describe the formation of SiO<sub>2</sub>/Au NP-based hollow microspheres using dye-tagged PLL, and then discuss the formation of the Au NP-polymer flocs and its importance to microsphere formation.

### 2.3.1. Hollow microsphere formation

Fig. 2.1a shows the confocal image of a homogeneous aqueous solution of PLL3, in which no visible aggregates in the solution were observed. The conformation of PLL ( $pK_a \sim 11.1$ ) in aqueous solution depends on the degree of protonation of the  $\epsilon$ -amino group of the side chain. At neutral pH, the polymer would be in an extended, random coil conformation due to complete protonation. The addition of the negatively charged Au NPs to PLL3 clearly led to the formation of Au NP-PLL3 flocs, observed as discrete fluorescent spots at different focal planes in the z-direction (Fig. 2.1b). Most of the flocs appeared larger than their actual sizes in solution, likely due to their spreading on contact

with glass (cover slip and glass slide). The larger flocs were spherical in shape and uniformly fluorescent within each floc.

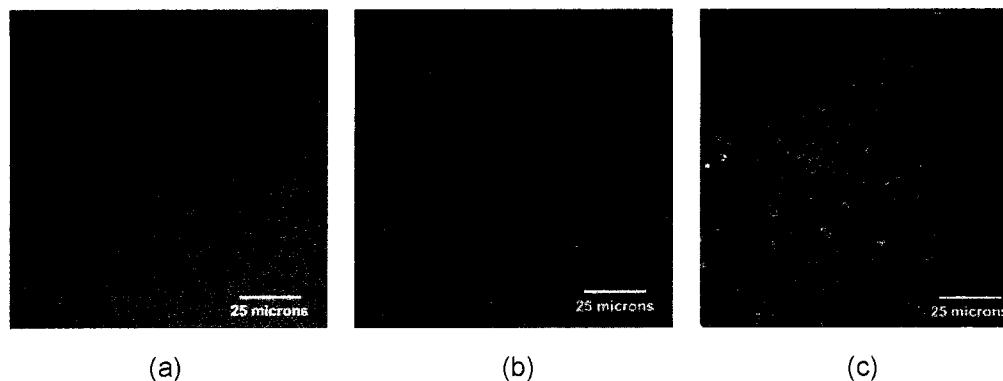


**Figure 2.1.** Confocal microscopy images showing the step-by-step formation of microspheres using PLL, Au NP, and SiO<sub>2</sub> NP. (a) PLL3 (conjugated to FITC dye) in solution, (b) globular flocs formed from Au NP-PLL3, and (c) microspheres formed after addition of SiO<sub>2</sub> NP to Au NP-PLL3 flocs.

SiO<sub>2</sub> NP addition to the Au NP-PLL3 suspension resulted instantaneously in hollow spheres, in which the SiO<sub>2</sub> NPs adsorbed around the Au NP-PLL3 flocs. The observed fluorescent ring structure (Fig. 2.1c) indicated the presence of PLL3 within the SiO<sub>2</sub> shell wall. The core region of the hollow spheres exhibited weak but non-zero fluorescence, which was verified through line intensity profile analysis (Fig. 2.2). The hollow sphere interior contained PLL3, but apparently at a lower concentration than that in the shell wall. PLL1 and PLL2 gave rise to hollow microspheres also.

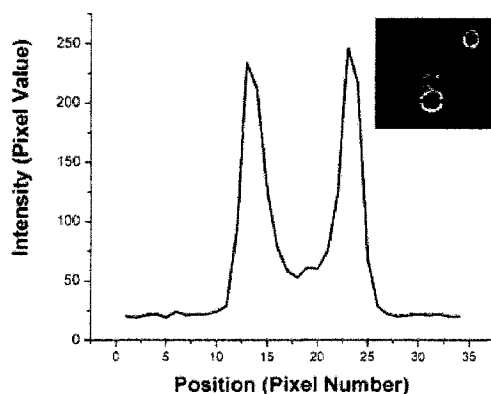


**Figure 2.2.** Line intensity profile across a microsphere showing the core-shell structure. Note that the fluorescence intensity is non-zero in the core and in the background.

When the spheres were air-dried overnight after aging for two days in suspension, and subjected to reduced pressure for 10 min, the microspheres decreased roughly by 50% in diameter (Fig. 2.3); the size reduction was verified to result from drying and not from the low pressure.

The dried spheres exhibited fluorescence from the shell wall and, curiously, from the core interior also (Fig. 2.3b). Confocal microscopy eliminates fluorescence contributions from sample features not in the focal plane, and so the observed fluorescence from the microsphere interior indicated the presence of the FITC-tagged PLL suspended within the center of the spheres. TEM images of PLL3-Au NP-SiO<sub>2</sub> NP hollow spheres confirmed the presence of the hollow (Fig. 2.4). The TEM image also provides evidence that hollow spheres as small as ~700 nm in diameter can be prepared.

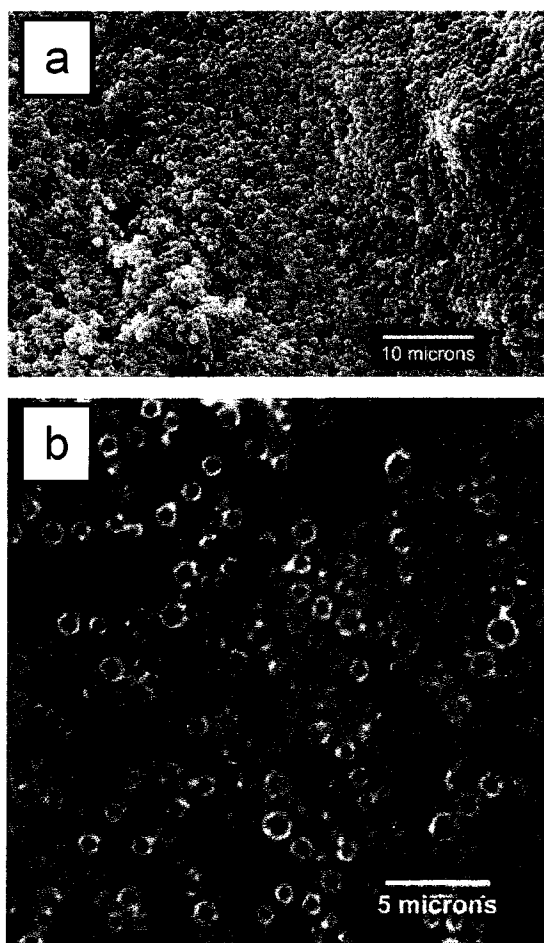


**Figure 2.3.** (a) Scanning electron microscopy image and (b) confocal microscopy image of microspheres (made from PLL3) after they have been dried and subjected to a vacuum of  $5 \times 10^{-5}$  torr at room temperature. Autoquant deblurring software was used to process the raw image in Fig. 2.3(b).

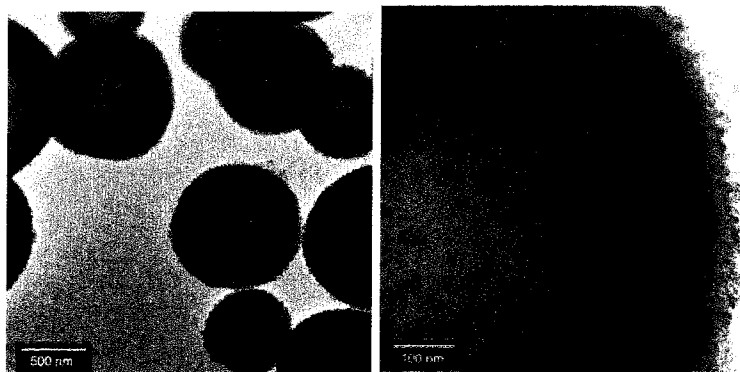


**Figure 2.4.** TEM images of hollow spheres made from PLL-FITC-Au NP-SiO<sub>2</sub> NP. The spheres were aged for six days before imaging.

### 2.3.2. Au NP-PLL floc formation

Charge-driven flocculation occurs when a colloidal sol is destabilized by the adsorption of oppositely charged polyelectrolytes, which neutralizes particle surface charge and leads to inter-particle polymer bridging [39-42]. The initial flocculation period for Au NPs in the presence of salts under rapid coagulation conditions (von Smoluchowski kinetics) is known to be very short, with a characteristic aggregation time of about 59 milliseconds and a coagulation rate constant of  $12.6 \times 10^{-18} \text{ m}^3/\text{s}$  (at 298 K [42]). We expect the initial stages of Au NP-PLL flocculation to follow rapid coagulation kinetics also, in which PLL binds to several NPs (to form a “multiplet” [43,44]). Floc growth after initial formation is generally not well understood still, as non-equilibrium conditions combined with the simultaneous fast dynamics of polymer adsorption, floc restructuring, and interparticle collisions under turbulent mixing conditions complicate the study of flocculation [45]. Still, some conclusions can be made for the Au NP-PLL floc system.

Light scattering experiments were performed on the floc suspension to study the Au NP-PLL floc size as a function of aging time. Larger Au NP-PLL flocs were found with longer aging times and with larger molecular weights (Fig. 2.5). The floc sizes ranged from a hydrodynamic diameter of 440 nm (at 3 min with the shortest PLL chain, PLL1) to 1.1  $\mu\text{m}$  (at 21 min with the longest PLL chain, PLL3), much larger than the measured hydrodynamic diameters of the polymer and Au NPs (Tables 2.1 and 2.2). The hydrodynamic diameter was found to increase monotonically with time for all three PLL chain lengths, with fluctuations appearing after 15 min. Such time-growth behavior of polymer-colloidal particle flocs has been observed before [25,46,47].

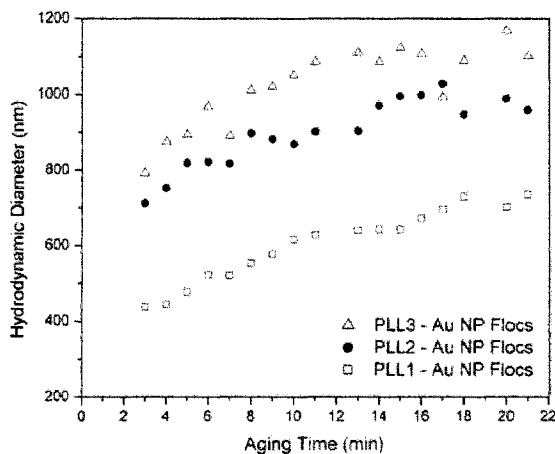


**Figure 2.5.** DLS time measurements of Au NP-PLL floc suspensions prepared with different PLL chain lengths. The error bar at each data point was  $\pm 20$  nm.

The shape of the floc growth curves can provide insights into the aggregation process of the polymer and the Au NPs. Assuming irreversible aggregation of PLL and NPs upon contact, a linear increase in floc diameter with time indicates the flocculation is reaction-limited, in which the adsorption of polymer and/or NP onto the floc occurs at a slower rate than their bulk diffusion to the floc outer surface. A sub-linear, square-root dependence of diameter to time, on the other hand, indicates a diffusion-limited flocculation process. In our case, Au NP-PLL floc growth appears better described as a diffusion-limited process than a reaction-limited one.

Additional mechanisms may be involved during floc growth and cannot be ruled out yet: (1) the internal restructuring of smaller flocs of higher density into larger flocs of lower density (at constant floc population) to minimize the ensemble entropy [43], (2) coalescence of smaller flocs into larger flocs (with decreasing floc population), (3) Ostwald ripening, in which the larger flocs grow at the expense of smaller flocs (with decreasing floc population), and (4) a combination of some or all of these processes.

Spectroscopy measurements of the Au NP-PLL3 floc suspensions before and after vortex mixing and aging for 5 min indicated ~90% of the polymer was incorporated into the floc structures. This percentage did not change when the flocs were aged for 15 hrs, suggesting that floc growth occurs through some process other than the incorporation of free polymer. Additional findings have also indicated that floc formation is sensitive to other factors, such as ionic strength and temperature of the suspending aqueous medium. Comprehensive studies to understand better the Au NP-PLL flocculation process, particularly at short aging times, is currently underway.

### 2.3.3. Sphere size control

The strong dependence of aging time on Au NP-PLL floc size suggested a method to control the size of the silica hollow spheres. This hypothesis was tested by synthesizing spheres from Au NP-PLL3 floc suspensions aged for different times (*i.e.*, 3 min, 20 min, and 2 hr), and indeed, a distinct size difference was observed among the resultant hollow spheres (Fig. 2.6).

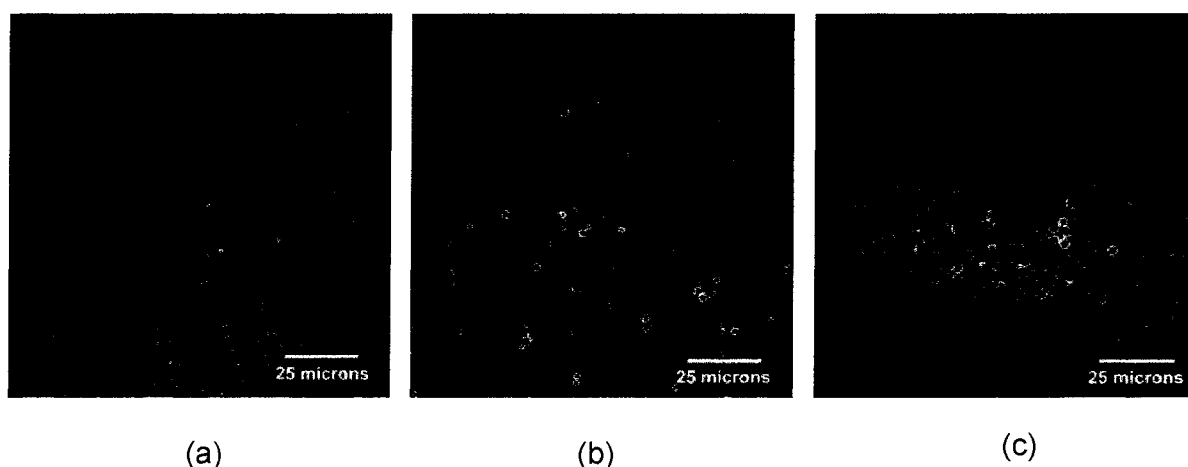


**Figure 2.6.** Confocal images of hollow microspheres prepared from Au NP-PLL3 floc suspensions aged from (a) 3 min, (b) 20 min, and (c) 2 hr.

Coulter counter measurements revealed that, with increased floc aging time, (1) the average sphere size increased, (2) the size distribution broadened, and (3) the sphere population decreased (Fig. 2.7). The size and size distribution of the hollow microspheres are several times larger than those of the corresponding Au NP-PLL flocs, which could point to a rapid floc-floc aggregation during SiO<sub>2</sub> shell formation which leads to the several-fold larger hollow spheres (Fig. 2.7, inset). From Coulter counter and confocal image analyses, the hollow sphere yields were estimated at 25, 14, and 3.5 million spheres per batch, prepared from floc suspensions aged at 3 min, 20 min, and 2 hr, respectively.

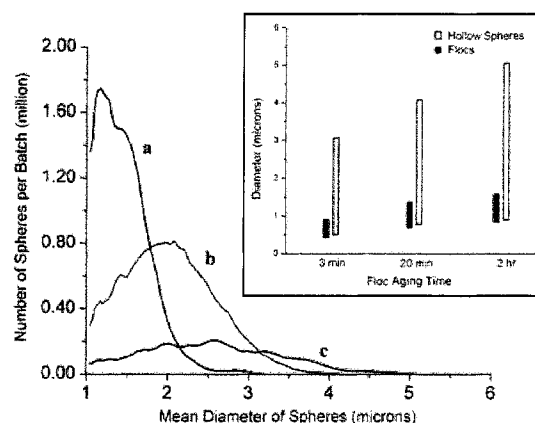


**Figure 2.7.** Coulter counter analysis of hollow microspheres prepared from Au NP-PLL3 floc suspensions aged for (a) 3 min, (b) 20 min, and (c) 2 hr. The lower limit of detection was 1.04  $\mu\text{m}$ . Inset: comparison of size distributions of the Au NP-PLL3 flocs (from DLS) and resultant hollow microspheres (from Coulter counter and confocal image analysis).

Interestingly, the fluorescence emanating from the hollow sphere core appeared to vary with sphere diameter, based on intensity profile analysis of different sized spheres within a single confocal image frame (Fig. 2.6b,c). The hollow spheres exhibited little to no fluorescence from the interior when the diameter exceeded  $\sim 4 \mu\text{m}$ . The Au NP-PLL



floc core may be structurally unstable inside the larger spheres even when suspended in a water medium, resulting in adsorption of PLL chains and Au NPs onto the inner wall of the sphere.

#### 2.3.4. Proposed formation mechanism of hollow spheres

Floc formation is the key step in microsphere synthesis, which was confirmed by changing the reaction order of the precursors. Combining SiO<sub>2</sub> NPs and PLL3 led to sheet-like aggregates, which did not lead to hollow spheres after Au NP addition (Fig. 2.8b). Combining PLL3 with a mixed SiO<sub>2</sub> and Au NP sol led to sheet-like aggregates also (Fig. 2.8c), indicating the importance of the Au NP-PLL3 floc to the formation of hollow spheres.

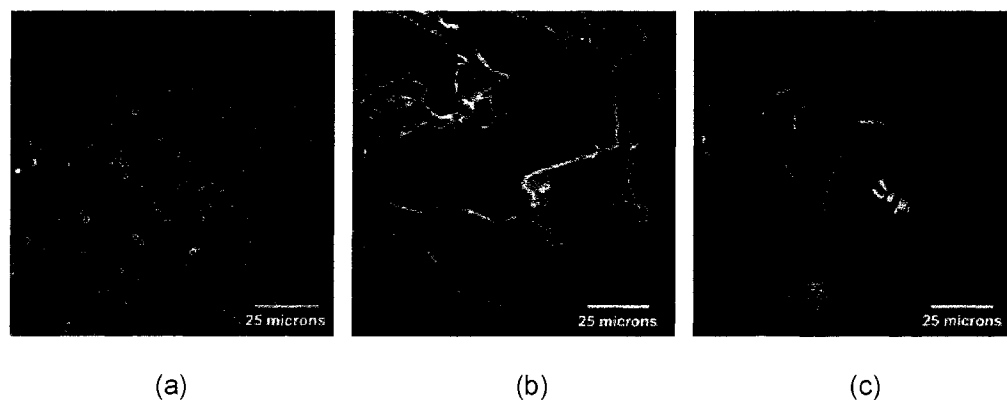


**Figure 2.8.** Confocal images of resultant suspensions (a) after SiO<sub>2</sub> NPs were added to Au NP-PLL3 flocs, (b) after Au NPs were added to SiO<sub>2</sub> NP-PLL3, and (c) after PLL3 was added to a combined Au NP-SiO<sub>2</sub> NP sol.

A formation mechanism that accounts for the dynamic growth of the Au NP-PLL floc intermediate is proposed (Fig. 2.9). In the two-step formation process, the PLL molecules bind electrostatically to negatively charged Au NPs. The PLL chain can bind to multiple NPs and NPs can serve as docking sites for multiple PLL chain adsorption, thereby

leading to bridging flocculation [24,25,48]. Poly(allylamine) was also observed to form flocs with Au NPs, which leads to the contention that Au NP-polymer floc aggregates can be induced by cationic polyelectrolytes. The floc assemblies continue to grow with time after combining and mixing the two precursors together, in a dynamic process that can be exploited to form larger hollow spheres. The floc acquires a positive charge due to an excess of polymer concentration over the Au NPs (confirmed through zeta potential measurements). On the addition of silica sol, the negatively charged  $\text{SiO}_2$  NPs adsorb onto the floc surface and initiates the formation of the shell structure. The  $\text{SiO}_2$  shell wall is thick and contains multiple layers of  $\text{SiO}_2$  NPs (Fig. 2.4), and PLL chains are incorporated within the shell to bind the  $\text{SiO}_2$  NPs together (Fig. 2.1c); how the PLL and the NPs combine to form the thick shell is still under investigation. The final, as-synthesized hollow spheres contain the Au NP-PLL floc and water in the center, of which the relative amounts depend on the sphere size.

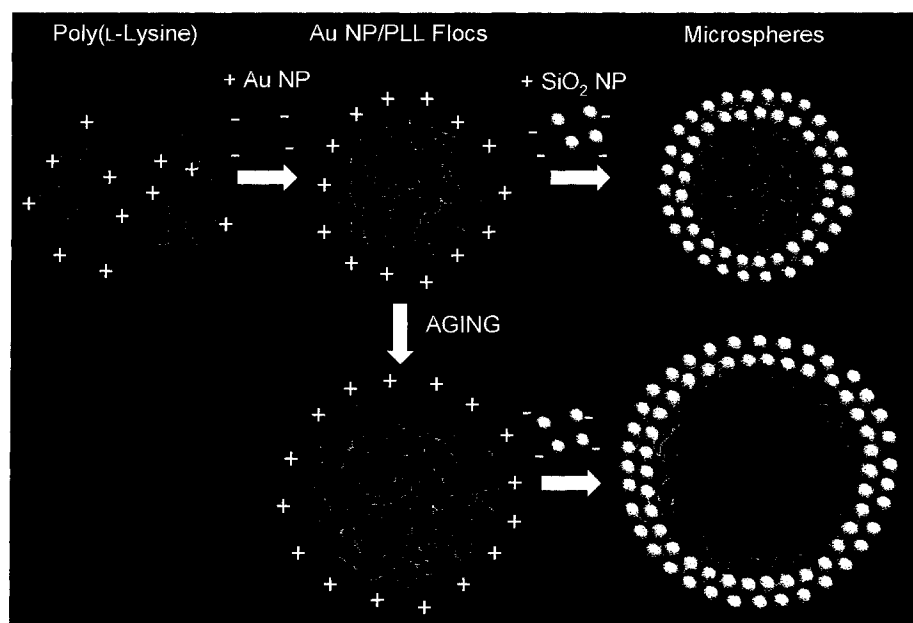


**Figure 2.9.** Proposed flocculation-based self-assembly of organic-inorganic hollow spheres from PLL, Au NPs, and  $\text{SiO}_2$  NPs.

### 2.3.5. Reversible assembly of hollow spheres

An interesting feature of the as-prepared hollow spheres is their ability to disassemble and re-assemble in response to pH variations in the suspension medium. It was conjectured that, if electrostatics were primarily the driving force in the shell formation, the shell could be broken apart by “turning” off or reversing the SiO<sub>2</sub> surface charge. The point-of-zero charge of SiO<sub>2</sub> is  $\sim 2$ , so the net surface charge would be negative at pH's above this value (e.g., the final synthesis pH of 4.9). When the original hollow sphere suspension (Fig. 2.10a) was acidified and subsequently imaged through confocal microscopy, only bright spots and a fluorescent background were observed (Fig. 2.10b). Hollow spheres were concluded to be broken down, releasing Au NP-PLL3 flocs and free PLL3 into solution. The pH of the suspension was then increased to  $\sim 10$ , at which hollow spheres were again detected, thus indicating re-assembly (Fig. 2.10c). A higher pH than the original synthesis pH of 4.9 was required to counteract the increased ionic strength of the suspension due to the additions of acid and base.

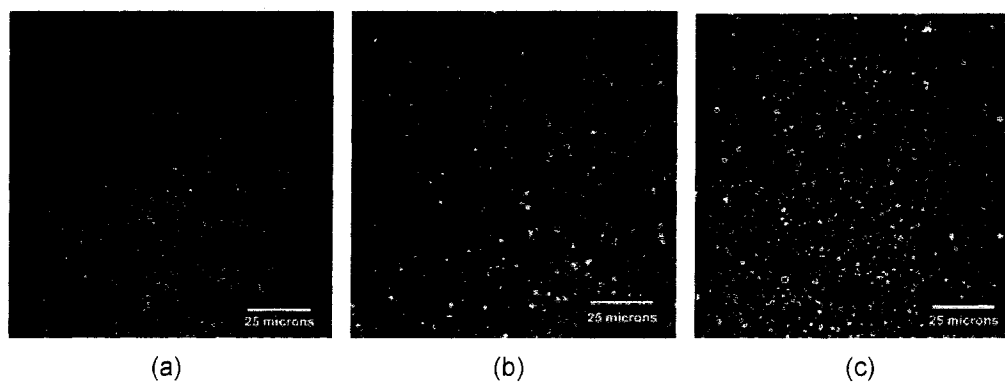


**Figure 2.10.** Images from confocal microscopy showing the structural reversibility of microspheres using a pH trigger. (a) As prepared hollow sphere suspension (pH  $\sim 4.9$ ), (b) acidification of suspension (final pH  $\sim 0.5$ ) causes the spheres to break due to re-dispersion of SiO<sub>2</sub> NP wall, and (c) addition of base to the acidified suspension re-assembles the microspheres (final pH  $\sim 10.0$ ).

## 2.4. Conclusions

In this chapter we have demonstrated that PLL and Au NPs form (sub)micron-sized flocculated aggregates that are critical to the formation of organic-inorganic NP-based hollow spheres. The formation of the spherical floc structures is consistent with charge-driven flocculation, in which polyelectrolyte molecules can adsorb onto several oppositely charged colloidal particles, and the particles can bind to more than one polyelectrolyte chain. The Au NP-PLL flocs act as a template around which SiO<sub>2</sub> NPs and PLL molecules adsorb to form a thick silica shell. The sizes of the hollow spheres can be roughly adjusted by the size of the Au NP-PLL floc (determined by aging time of the floc suspension). The floc structure within the sphere appear to span the volume of the hollow sphere interior, except if the spheres are larger than  $\sim 4\ \mu\text{m}$ . The formation of Au NP-polymer flocs may be generalized (from PLL and poly(allylamine)) to any cationic polyelectrolyte.

The two-step formation of these Au and SiO<sub>2</sub> NP-based hollow spheres can be considered an NP self-assembly process induced by the presence of polyelectrolytes, in which the hollow spheres are rapidly generated at room temperature, near neutral pHs, in water, without the need of a solid template, and with minimal human intervention. These attributes of the flocculation based self-assembly (or “flocculation assembly”) of NPs into hollow microspheres provide new opportunities in encapsulation and release not available to other types of hollow sphere materials. It is intriguing that a hierarchically structured material can be built from NPs even though the electrostatic interactions between the charged NP surface and polymer molecule are non-specific and non-

directional. Clearly, some concepts of flocculation help to explain the formation of these hollow spheres, particularly the first step of Au NP-polymer spherical floc formation.

## 2.5. References

- [1] Caruso, F., Caruso, R.A., Mohwald, H. Nanoengineering of inorganic and hybrid hollow spheres by colloidal templating *Science*, **1998**, 282, 1111.
- [2] Duan, H.W., Chen, D.Y., Jiang, M., Gan, W.J., Li, S.J., Wang, M., Gong, J. Self-assembly of unlike homopolymers into hollow spheres in nonselective solvent *Journal of the American Chemical Society*, **2001**, 123, 12097.
- [3] Fowler, C.E., Khushalani, D., Mann, S. Interfacial synthesis of hollow microspheres of mesostructured silica *Chemical Communications*, **2001**, 19, 2028.
- [4] van Bommel, K.J.C., Jung, J.H., Shinkai, S. Poly(L-lysine) aggregates as templates for the formation of hollow silica spheres *Advanced Materials*, **2001**, 13, 1472.
- [5] Tsapis, N., Bennett, D., Jackson, B., Weitz, D.A., Edwards, D.A. Trojan particles: Large porous carriers of nanoparticles for drug delivery *Proceedings of National Academy of Sciences of the United States of America*, **2002**, 99, 12001.
- [6] Zhong, Z.Y., Yin, Y.D., Gates, B., Xia, Y.N. Preparation of mesoscale hollow spheres of TiO<sub>2</sub> and SnO<sub>2</sub> by templating against crystalline arrays of polystyrene beads *Advanced Materials*, **2000**, 12, 206.
- [7] Jiang, P., Bertone, J.F., Colvin, V.L. A lost-wax approach to monodisperse colloids and their crystals *Science*, **2001**, 291, 453.
- [8] Kulak, A., Davis, S.A., Dujardin, E., Mann, S. Controlled assembly of nanoparticle-containing gold and silica microspheres and silica/gold nanocomposite spheroids with complex form *Chemistry of Materials*, **2003**, 15, 528.

- [9] Dinsmore, A.D., Hsu, M.F., Nikolaides, M.G., Marquez, M., Bausch, A.R., Weitz, D.A. Colloidosomes: Selectively permeable capsules composed of colloidal particles *Science*, **2002**, 298, 1006.
- [10] Checot, F., Lecommandoux, S., Gnanou, Y., Klok, H.A. Water-soluble stimuli-responsive vesicles from peptide-based diblock copolymers *Angewandte Chemie-International Edition*, **2002**, 41, 1339.
- [11] Walker, S.A., Kennedy, M.T., Zasadzinski, J.A. Encapsulation of bilayer vesicles by self-assembly *Nature*, **1997**, 387, 61.
- [12] Antonietti, M., Forster, S. Vesicles and liposomes: A self-assembly principle beyond lipids *Advanced Materials*, **2003**, 15, 1323.
- [13] Huang, H.Y., Remsen, E.E., Kowalewski, T., Wooley, K.L. Nanocages derived from shell cross-linked micelle templates *Journal of the American Chemical Society*, **1999**, 121, 3905.
- [14] Thurmond, K.B., Kowalewski, T., Wooley, K.L. Water-soluble knedel-like structures: The preparation of shell-cross-linked small particles *Journal of the American Chemical Society*, **1996**, 118, 7239.
- [15] Discher, B.M., Won, Y.Y., Ege, D.S., Lee, J.C.M., Bates, F.S., Discher, D.E., Hammer, D.A. Polymersomes: Tough vesicles made from diblock copolymers *Science*, **1999**, 284, 1143.
- [16] Khopade, A.J., Caruso, F. Electrostatically assembled polyelectrolyte/dendrimer multilayer films as ultrathin nanoreservoirs *Nano Letters*, **2002**, 2, 415.
- [17] Schuler, C., Caruso, F. Decomposable hollow biopolymer-based capsules *Biomacromolecules*, **2001**, 2, 921.
- [18] Park, M.K., Xia, C.J., Advincula, R.C., Schutz, P., Caruso, F. Cross-linked, luminescent spherical colloidal and hollow-shell particles *Langmuir*, **2001**, 17, 7670.
- [19] Caruso, F., Yang, W.J., Trau, D., Renneberg, R. Microencapsulation of uncharged low molecular weight organic materials by polyelectrolyte multilayer self-assembly *Langmuir*, **2000**, 16, 8932.

- [20] Binks, B.P., Lumsdon, S.O. Stability of oil-in-water emulsions stabilised by silica particles *Physical Chemistry Chemical Physics*, **1999**, *1*,
- [21] Wong, M.S., Cha, J.N., Choi, K.S., Deming, T.J., Stucky, G.D. Assembly of nanoparticles into hollow spheres using block copolypeptides *Nano Letters*, **2002**, *2*, 583.
- [22] Cha, J.N., Bartl, M.H., Wong, M.S., Popitsch, A., Deming, T.J., Stucky, G.D. Microcavity lasing from block peptide hierarchically assembled quantum dot spherical resonators *Nano Letters*, **2003**, *3*, 907.
- [23] Cha, J.N., Birkedal, H., Euliss, L.E., Bartl, M.H., Wong, M.S., Deming, T.J., Stucky, G.D. Spontaneous formation of nanoparticle vesicles from homopolymer polyelectrolytes *Journal of the American Chemical Society*, **2003**, *125*, 8285.
- [24] Dickinson, E., Eriksson, L. Particle flocculation by adsorbing polymers *Advances in Colloid and Interface Science*, **1991**, *34*, 1.
- [25] Biggs, S., Habgood, M., Jameson, G.J., Yan, Y.D. Aggregate structures formed via a bridging flocculation mechanism *Chemical Engineering Journal*, **2000**, *80*, 13.
- [26] Glover, S.M., Yan, Y.D., Jameson, G.J., Biggs, S. Bridging flocculation studied by light scattering and settling *Chemical Engineering Journal*, **2000**, *80*, 3.
- [27] Thomas, D.N., Judd, S.J., Fawcett, N. Flocculation modelling: A review *Water Research*, **1999**, *33*, 1579.
- [28] Berlin, A.A., Solomentseva, I.M., Kislenko, V.N. Suspension flocculation by polyelectrolytes: Experimental verification of a developed mathematical model *Journal of Colloid and Interface Science*, **1997**, *191*, 273.
- [29] Larsson, A., Walldal, C., Wall, S. Flocculation of cationic polymers and nanosized particles *Colloid and Surfaces A: Physicochemical and Engineering Aspects*, **1999**, *159*, 65.
- [30] Wong, K., Cabane, B., Somasundaran, P. Highly ordered microstructure of flocculated aggregates *Colloid and Surfaces*, **1988**, *30*, 355.

- [31] Verkleij, A.J., Leunissen, L.M., Insler, V., *Immuno-gold Labeling in Cell Biology*, CRC Press, Boca Raton, **1989**.
- [32] Frens, G. Controlled nucleation for the regulation of the particle size in monodisperse gold suspensions *Nature Physical Science*, **1973**, 243, 20.
- [33] Mirkin, C.A. Programming the assembly of two- and three-dimensional architectures with DNA and nanoscale inorganic building blocks *Inorganic Chemistry*, **2000**, 39, 2258.
- [34] Rajagopalan, R., Hiemenz, P.C., *Principles of Colloid and Surface Chemistry*, 3rd ed., Marcel Dekker, New York, **1997**.
- [35] Kimura, K., Takashima, S., Ohshima, H. Molecular approach to the surface potential estimate of thiolate-modified gold nanoparticles *Journal of Physical Chemistry B*, **2002**, 106, 7260.
- [36] National Institute of health (<http://rsb.info.nih.gov/ij/>)
- [37] McNeil-Watson, F., Tschamuter, W., Miller, J. A new instrument for the measurement of very small electrophoretic mobilities using phase analysis light scattering (PALS) *Colloid and Surfaces A: Physicochemical and Engineering Aspects*, **1998**, 140, 53.
- [38] Instruction Manual for BI-Zeta Potential Option: Brookhaven Instrument Corporation, 2000
- [39] Spalla, O. Nanoparticle interactions with polymers and polyelectrolytes *Current Opinion in Colloid and Interface Science*, **2002**, 7, 179.
- [40] Finch, C.A. *Industrial Water Soluble Polymers*; Royal Society of Chemistry: Cambridge, U.K., **1996**
- [41] Sonntag, H., Strenge, K., *Coagulation Kinetics and Structure Formation*, Plenum Press, New York, **1987**.
- [42] Dobias, B. *Coagulation and Flocculation*; Marcel Dekker: New York, **1993**



- [43] Nowicki, W. Kinetic behaviour of the system composed of nanosized gold particles and very-high-molecular-weight polyacrylamide *Colloid and Surfaces A: Physicochemical and Engineering Aspects*, **2001**, 194, 159.
- [44] Spalla, O., Cabane, B. Growth of colloidal aggregates through polymer bridging *Colloid and Polymer Science*, **1993**, 271, 357.
- [45] Adachi, Y., Matsumoto, T., Stuart, M.A.C. Effects of hydrodynamic mixing intensity coupled with ionic strength on the initial stage dynamics of bridging flocculation of polystyrene latex particles with polyelectrolyte *Colloid and Surfaces A: Physicochemical and Engineering Aspects*, **2002**, 207, 253.
- [46] Ovenden, C., Xiao, H.N. Flocculation behaviour and mechanisms of cationic inorganic microparticle/polymer systems *Colloid and Surfaces A: Physicochemical and Engineering Aspects*, **2002**, 197, 225.
- [47] Spicer, P.T., Pratsinis, S.E. Shear-induced flocculation: The evolution of floc structure and the shape of the size distribution at steady state *Water Research*, **1996**, 30, 1049.
- [48] Akinchina, A., Linse, P. Monte Carlo simulations of polyion-macroion complexes. 1. Equal absolute polyion and macroion charges *Macromolecules*, **2002**, 35, 5183.

## **Chapter 3. Nanoparticle-assembled capsule synthesis: Formation of colloidal polyamine-salt intermediates\***

### **3.1. Introduction**

We recently reported a new approach to preparing stable microcapsules through a simple two-step mixing procedure involving negatively charged nanoparticles (NPs), cationic polymer, and multivalent anions [1] (also see Appendix A). Termed “tandem self-assembly” or “polymer aggregate templating,” this process involves combining the polymer and salt to form polymer-salt aggregates, and subsequently combining these with NPs to form the hollow sphere structures. Stucky and co-workers recently reported on a similar materials synthesis approach [2]. The spheres are nominally in the 1-4 micron diameter range, the shell walls are made of NPs and polymer, and the core interior can contain either water or polymer. These spheres are called nanoparticle-assembled capsules, or NACs. This synthesis is rapid and scalable, and it occurs under ambient conditions, in water, and at mild pH values. NAC synthesis further allows the non-destructive encapsulation of water-soluble compounds. Thus NP assembly offers new possibilities for engineering microcapsules for encapsulation applications, relative to the preparation methods of self-assembly, sacrificial templating, and physical formation.

In this paper, we focus on understanding the non-covalent chemistry involved in the first step of NAC synthesis, namely the formation of polymer-salt aggregates. We use poly(allylamine hydrochloride) (PAH) as the model cationic polyelectrolyte, to study its aggregation behavior as induced by multivalent anions as a function of charge ratio, pH, and aging time. We discuss the electrostatic interactions between PAH and anions in terms of counterion condensation, and the growth of the PAH-salt aggregates in terms of

---

\* Murthy, V.S., Rana, R.K., Wong, M.S., submitted to *J. Phys. Chem. B*.

charged colloid stability. Finally, we analyze the effect of polymer aggregate aging time on NAC size.

## **3.2. Experimental section**

### **3.2.1. Materials**

Poly(allylamine hydrochloride) (70,000 g/mol, chloride counterion, “PAH”), tetrasodium ethylenediaminetetraacetate (98%, “edta”), disodium citrate (98%), monosodium citrate (99%), and sodium acetate (99.8%, all from Sigma-Aldrich), and trisodium citrate (“cit”) and disodium sulfate (99+%) (all from Fisher Scientific) were used as-received. Polyelectrolyte stock solution and all subsequent diluted precursor solutions were made using deionized water (18.2 MΩ, Barnstead Nanopure Diamond System). Glutaraldehyde (25% aqueous solution, Sigma-Aldrich) was used as-received. The fluorescent dyes of fluorescein isothiocyanate (FITC) and rhodamine B isothiocyanate (RITC) were procured from Sigma-Aldrich. SiO<sub>2</sub> NPs (Snowtex-O, Nissan Chemicals) was available as aqueous colloidal suspension (20.5 wt%, pH 3.4, ionic strength  $I = 16.9$  mM). The NPs measured  $13 \pm 3$  nm in diameter, according to dynamic light scattering. Zeta potential ( $\xi$ ) of SiO<sub>2</sub> NP in the original sol condition was calculated from its electrophoretic mobility ( $-1.4$  (μm/sec)/V/cm)) to be -16 mV in the Henry’s limit.

### **3.2.2. Synthesis**

All experiments with polyelectrolyte-salt solutions were done at specific charge ratio  $R$ , which is defined as the ratio of total negative charge of the added salt to the total positive charge of the polymer ( $R = [\text{anion}] \times |z_-| / [\text{polymer}] \times |z_+|$ , where  $z_-$  is negative

charge per anion and  $z_+$  is positive charge per chain). A typical preparation of PAH-cit suspension was carried out by combining 1 ml of PAH precursor solution (precursor concentration range of 0.01 mg/ml to 40 mg/ml) with 2.5 ml of cit solution (precursor concentration range of  $1.4 \times 10^{-2}$  mM to 71.3 mM) in a polystyrene centrifuge tube, resulting in final PAH concentration of  $2.9 \times 10^{-3}$  mg/ml to 11.4 mg/ml. Immediately, the resulting aliquot became turbid, except in cases of low PAH precursor concentration ( $\leq 0.1$  mg/ml) in which turbidity was not apparent by eye. This turbid reaction mixture was vortex-mixed for 10 seconds at low speed ('5' speed on a 1-10 scale, Fisher Scientific Mini Vortexer); aging time of the suspension started at the end of mixing. The NACs were prepared by adding 2.5 ml of the stock SiO<sub>2</sub> NP sol to the-above polymer-salt suspension (aged for 30 min) and vigorously vortex-mixing at '7' speed for 20 seconds.

Dye conjugation of PAH was performed in the following manner: 4 mg of FITC was dissolved in 500  $\mu$ l of dimethylsulfoxide (DMSO, 99.8+%, EM Science). 500 mg of PAH was dissolved in 6 ml deionized water, with the solution pH adjusted to 8.4 using NaOH. The two solutions were combined and stirred for two days at room temperature in the dark. The resulting solution was dialyzed against deionized water for 48 hr (molecular cut-off of 2000 Da, POR<sup>®</sup> 7 dialysis membrane, Spectrum Laboratories), with the final product dried and recovered in a rotary evaporator. A similar procedure was carried out for the synthesis of PAH-RITC, except that 2 mg of the RITC dye was dissolved in 250  $\mu$ l DMSO, and 250 mg of PAH was dissolved in 3 ml deionized water (pH adjusted to 9.5). PAH-FITC and PAH-RITC stock solutions (50 mg/ml) were prepared in water and refrigerated. The average number of dye molecules per PAH chain was  $\sim 2$ , as determined through fluorescence spectroscopy.

### 3.2.3. Characterization

**Atomic Force Microscopy.** Tapping mode atomic force microscopy (AFM) was performed on Digital Instrument Nanoscope IIIA Atomic Force Microscope using a 125 micrometer TESP tip. After aging for 30 min, 100  $\mu$ l of a prepared suspension (1 ml of PAH solution (5 mg/ml) + 2.5 ml of cit solution (14.26 mM,  $R = 2$ )) was placed on a freshly cleaved mica surface. After 1 min of deposition time, the mica substrate was rinsed with deionized water and dried overnight ( $\sim$ 12 hr) before imaging.

**Chloride Ion Selective Electrode Measurements.** Potentiometric measurements for detecting free chloride ions were performed using Thermo Orion Model 720A Plus benchtop meter and chloride Ionplus electrode (Orion Cat. No. 9617BN) at room temperature. Each measurement was taken immediately after sample preparation, lasting *ca.* 1 min. Free chloride concentration was measured for PAH-salt suspensions in the range of  $R = 0.1$  to 10. Measurements were inaccurate above  $R = 5$  for the PAH-edta case due to high ionic strength effects. Three-point calibration was performed using NaCl solutions (100 mM, 10 mM, and 1 mM).

**Cryo-Transmission Electron Microscopy.** Transmission electron microscopy (TEM) was performed on JEOL2010 FasTEM system at 100 kV electron beam accelerating voltage. 1 ml of PAH solution (0.1 mg/ml) was combined with 2.5 ml of cit solution (0.713 mM,  $R = 5$ ) and vortex mixed for 10 sec. Immediately afterwards, a drop of the suspension was cast onto a holey carbon copper TEM grid, followed by vitrification in liquid ethane. The grid was then transferred to liquid nitrogen and stored (for approximately 30 min) until imaging.

**Dynamic Light Scattering.** Size distribution analysis was carried out with Brookhaven ZetaPALS dynamic light scattering (DLS) equipment with BI-9000AT digital autocorrelator at 656 nm wavelength. All studies were done at a 90° scattering angle and temperature controlled at 25 °C in standard 4 ml polystyrene cuvettes.

For studying the evolution of PAH-salt aggregates with time, size measurements were taken of suspensions using the software package “*9KPSDW*.” Measurements began three minutes after vortex mixing, and were carried out for a total of 30 min, with each consecutive run (as one data point) lasting for 2 minutes. The three-minute time gap was due to transferring the suspension from the synthesis tube to the DLS cuvette and instrument set-up.

**Electrophoretic Mobility Analysis.** Electrophoretic mobility was measured by phase analysis light scattering (PALS) in the Brookhaven ZetaPALS setup. A dip-in (Uzgiris type) electrode system with 4 ml polystyrene cuvettes was used, and measurements were taken at 25 °C.

**Laser Scanning Confocal Microscopy.** Confocal images were captured with Carl Zeiss LSM 510 inverted microscope equipped with a 100× oil immersion objective (NA = 1.4). The laser excitation wavelength of 488 nm was chosen for FITC ( $\lambda_{ex} = 494$  nm,  $\lambda_{em} = 519$  nm) and excitation wavelength of 543 nm for RITC ( $\lambda_{ex} = 560$  nm,  $\lambda_{em} = 580$  nm). Samples were mounted on conventional glass slides and sealed under a cover slip to prevent drying. All samples were prepared approximately 0.5-1 hr prior to imaging. For two-color simultaneous imaging, it was confirmed (by confocal microscopy and fluorescence spectroscopy) that there was negligible emission spectrum overlap between the two dyes.

**Scanning Electron Microscopy.** Scanning electron microscopy (SEM) was carried out in JEOL6500 field emission microscope equipped with in-lens thermal field emission electron gun. Secondary electron image (SEI) was taken at 15 kV electron beam with a working distance of 10.0 mm. The microcapsule suspension was washed with water, and loaded on an SEM stub. After drying overnight, the sample was sputter-coated with gold.

**Ultramicrotome.** Samples were initially washed, dried, and suspended in a fluid resin medium (Pelco Eponate 12<sup>TM</sup> Kit with BDMA, Ted Pella, Inc.) and heated at 65 °C for 16 hrs. The hardened resin block was then cut into 500 nm thick wafers approximately 0.5×0.5 mm<sup>2</sup> in size using a glass knife on a Leica Ultracut microtome.

### 3.3. Results and discussions

#### 3.3.1. Morphology of PAH-cit aggregates

A clear PAH-FITC solution (5 mg/ml) immediately turned turbid when combined with a cit solution ( $R = 2$ ), indicating the formation of the light-scattering PAH-cit aggregate domains. After aging for 30 min, the PAH-cit suspension was imaged through optical microscopy (Fig. 3.1a,b). Adhering to the glass coverslip, the aggregates were 1 to 8.5  $\mu\text{m}$  in size and were homogeneously fluorescent, indicating they were composed of PAH-FITC. Addition of silica NPs to the PAH-cit suspension led to the formation of microcapsules with NP/polymer shell walls and polymer-filled core (Fig. 3.1d-f).

Under dried conditions during AFM measurement, the aggregates were dome-shaped, indicating a flattening of the spherical aggregates (Fig. 3.1c). The wide range in dried aggregate height (100-800 nm) and the deviation from the hydrodynamic diameter of the aggregate suspension (2.7-3.8  $\mu\text{m}$ ) are the result of uncontrolled aggregate spreading

across the mica surface and evaporative loss of internal water. High resolution scanning of a small surface area of the domains ( $50 \times 50 \text{ nm}^2$  area, data not shown) showed a smooth surface devoid of any notable surface features at a height resolution of 10 nm, suggesting a compact packing of the dried polymer-salt aggregate.

Cryo-TEM was used to capture aggregate morphology in suspension and to eliminate surface spreading effects. Dilute solutions of the precursors and no aging aided in the imaging of small aggregates (Fig. 3.2). The clusters were spherical, ranging in size from 70 to 210 nm. The average diameter was measured to be 120 nm and the standard deviation to be 45 nm (based on >175 aggregates).

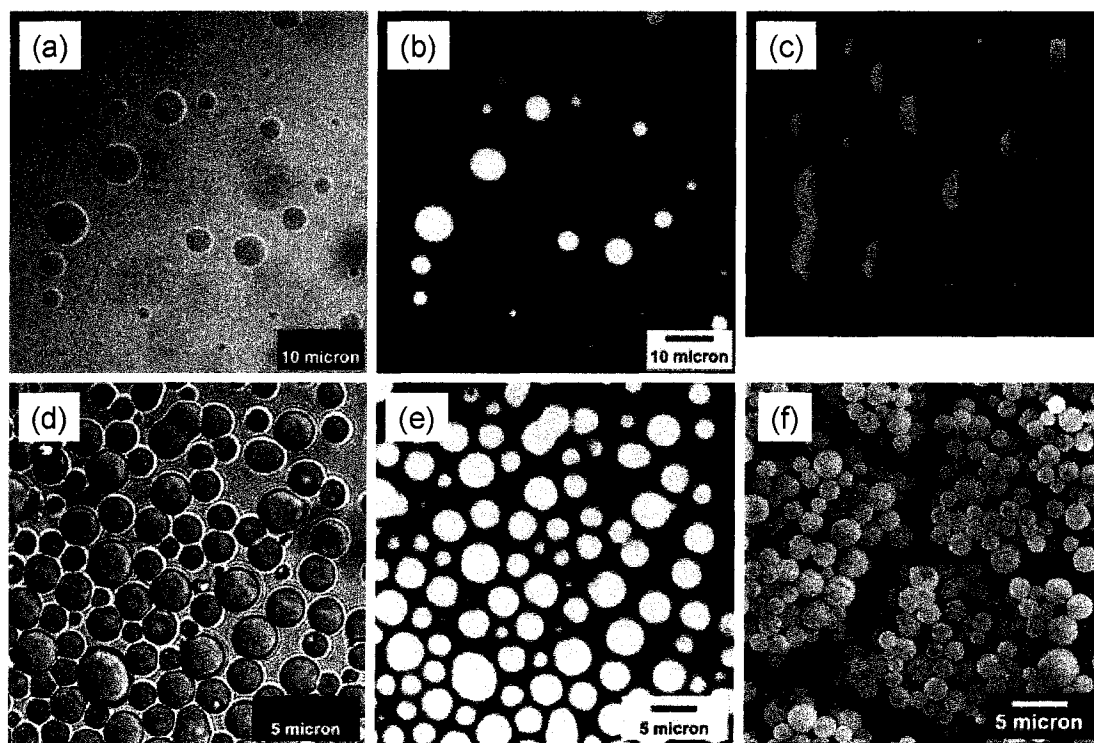


**Figure 3.1.** (a) Brightfield and (b) confocal microscopy images of surface-bound PAH-FITC-cit aggregates in a water environment. (c) AFM images of air-dried PAH-cit aggregates supported on freshly cleaved mica surface. Synthesis conditions:  $[\text{PAH}]_{\text{final}} = 1.43 \text{ mg/ml}$ ,  $[\text{cit}]_{\text{final}} = 10.19 \text{ mM}$ ,  $R = 2$ , aging time of PAH-cit suspension = 30 min. (d) Brightfield, (e) confocal microscopy, and (f) SEM images of the resultant capsules, after addition of SiO<sub>2</sub> NPs to the-above PAH-cit suspension.



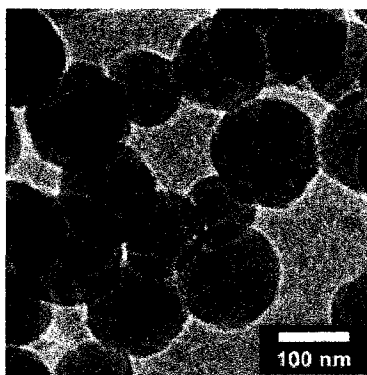


**Figure 3.2.** Cryo-TEM image of PAH-cit aggregate suspension. Synthesis conditions:  $[\text{PAH}]_{\text{final}} = 0.029 \text{ mg/ml}$ ,  $[\text{cit}]_{\text{final}} = 0.2 \text{ mM}$ ,  $R = 2$ , no aging of PAH-cit suspension.

We note that others have recently reported similar experimental observations in which polyamines formed aggregates in the presence of multivalent anions [3-6]. Kröger *et al.* reported that the cationic polypeptides isolated from diatom cell walls formed polymer aggregates if the polymer carried covalently-bound phosphate groups or if a phosphate buffer was used [6]. Patwardhan and Clarkson remarked that PAH was “not fully soluble in phosphate-citrate buffer” in their study on silica synthesis [3].

### 3.3.2. Charge ratio $R$ effect on PAH-salt aggregate formation

PAH aggregation was observed for all salts, except the acetate anion (Fig. 3.3). At very low  $R$  ratios, the addition of small amounts of monovalent (acetate), divalent (succinate), trivalent (cit), or tetravalent (edta) salt negligibly increased the free Cl concentration (Fig. 3.4). Above  $R = 0.01$ , the free Cl concentration increased for the four salts.

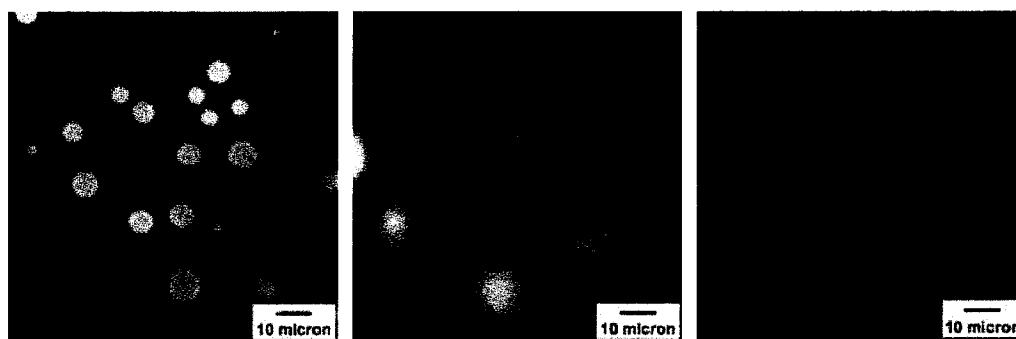


**Figure 3.3.** Confocal microscopy images of aggregates formed from PAH and various multivalent salts. Aggregates were formed with (a) tetravalent  $\text{EDTA}^{4-}$  and (b) divalent  $\text{SO}_4^{2-}$ , but acetate $^{1-}$  (c) did not result in any clusters. Synthesis conditions:  $[\text{PAH}]_{\text{final}} = 1.43 \text{ mg/ml}$ ,  $R = 2$ , aging time = 30 min.

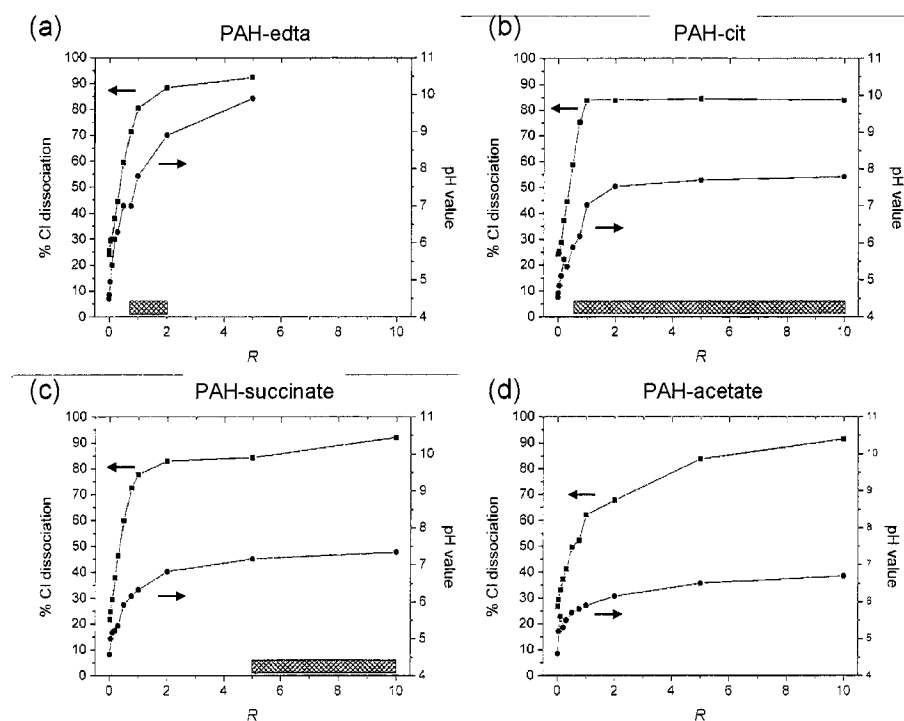


**Figure 3.4.** Percentage of total Cl in PAH solution as free ions (square data points) and corresponding pH values (round data points) as a function of charge ratio for multivalent salts: (a) edta, (b) cit, (c) succinate, and (d) acetate. Hatched marks indicate the  $R$  values at which aggregate formation occur. Synthesis:  $[\text{PAH}]_{\text{final}} = 1.43 \text{ mg/ml}$ , no aging.

We consider the process of salt-induced PAH aggregate formation to proceed with counterion condensation [7] followed by aggregation of the polyelectrolyte chains [8-10]. For polyelectrolyte solutions, it is well known through the Manning theory on counterion condensation that a fraction of the polymer counterions are bound or condensed onto the polyelectrolyte backbone in order to reduce the electrostatic repulsion energy of adjacent charged polymer units ( $e^2/4\pi\epsilon b$ ) relative to thermal energy levels ( $k_B T$ ) [7,11].  $\epsilon$  is the dielectric constant of pure bulk solvent,  $k_B$  is the Boltzmann constant,  $T$  is the absolute temperature, and  $b$  is the length of a polymer unit. The Manning theory provides a starting point as a simple theoretical model for understanding counterion condensation and polyelectrolyte solution behavior [7].

The Manning parameter is given as  $\zeta = l_B/b$ , where  $l_B$  is the Bjerrum length ( $= e^2/4\pi\epsilon k_B T$ ) which represent the effective distance between charged polymer units at which electrostatic energy equals thermal energy. The Bjerrum length in water at 25 °C is 7.14 Å. If  $\zeta$  of a polyelectrolyte solution is calculated to be  $>1$ , then counterion condensation is expected. For a PAH solution ( $b = 3.8$  Å, estimated from Chem3D) at 25 °C, we calculated  $\zeta$  to be 1.89 and the percentage of Cl as condensed ions to be  $1-(1/\zeta) = 47\%$  [7]. By measuring the free Cl concentration of a PAH solution (5 mg/ml), we determined that 75% of the total Cl content was bound to the PAH backbone, clearly demonstrating Cl condensation (Fig. 3.4). The discrepancy between the predicted and measured values is attributed to oversimplifications in the Manning theory, *e.g.*, the polymer molecule is modeled as infinitely long and infinitely thin chain of point charges separated by distance  $b$ , and there are no interactions among polymer chains [12].

As determined from the low  $R$  regime ( $R < 1$ ), 1.8, 1.5, 1.0, and 0.3 Cl anions were displaced per molecule of edta, cit, succinate, and acetate, respectively. The maximum Cl displacement was in the range of 80-90% up to salt concentrations of  $R = 10$ . 100% Cl dissociation is not expected, due to incomplete substitution of monovalent counterions by the multivalent ones [12,13].

It is helpful to consider multivalent anions as ionic crosslinkers between the polymer chains due to their multiple negatively-charged carboxylate “binding sites,” [1] of which the acetate anion has only one binding site. We presume that specific ion-pair site-binding occurs, *e.g.*, carboxylate and ammonium salt bridges in polycarboxylate-polyammonium complexes [14-17]. The electrostatic interaction may be non-specific also, in that the ions are bound to, but delocalized about, the polyelectrolyte chain [18].

Characterized by an immediate ten-fold increase in scattering intensity according to DLS, multivalent salt-crosslinked polymer aggregates were formed once a “critical” charge ratio  $R_c$  was reached (Fig. 3.4). The  $R_c$  values for edta and cit were smaller than 1 (0.75 and 0.6, respectively), indicating that a one-to-one charge stoichiometry was not required for aggregation to occur. It is not clear, though, why the  $R_c$  for divalent succinate was  $>1$ . For comparison, divalent sulfate was found to have a  $R_c$  of 0.75 (Fig. 3.5), indicating that anion molecular structure has a strong effect on  $R_c$ .

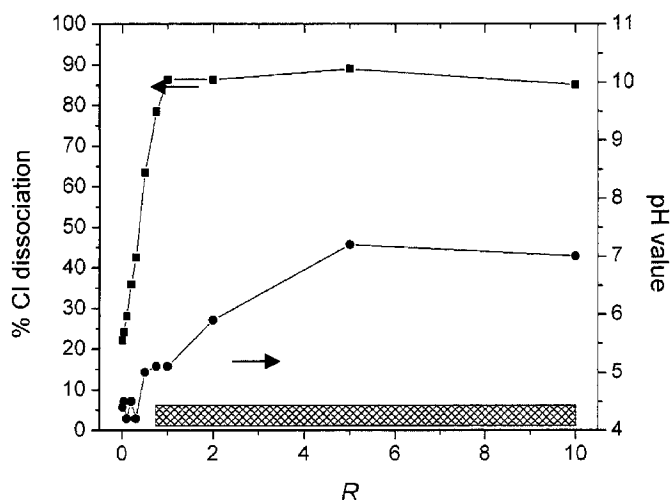


**Figure 3.5.** Percentage of total Cl in PAH solution as free ions (square data points) and corresponding pH values (round data points) as a function of charge ratio for sulfate salt. Hatched bar shows the  $R$  values at which aggregate formation occurs. Synthesis conditions:  $[\text{PAH}]_{\text{final}} = 1.43 \text{ mg/ml}$ , no aging.

In the case of the PAH-edta system, there was an upper critical charge ratio ( $R = 2$ ), above which aggregate formation did not occur. This was due to the high suspension pH resulting from the use of tetrasodium form of edta. Above  $R = 2$ , pH was greater than 9.0, which exceeded the  $\text{pK}_a$  of the protonated amine group of PAH ( $\sim 8.5$  [19]). The very high pH value “turned off” the positive charge of the polymer, thereby removing the electrostatic driving force between the edta and PAH.

### 3.3.3. Charge ratio $R$ effect on PAH-salt aggregate growth rate

PAH-citrate aggregates had growth rates that were dependent on charge ratios (Fig. 3.6a). Aggregation was observed at  $R_c = 0.8$ , which was slightly higher than the  $R_c = 0.6$  value indicated earlier, due to the lower final PAH concentration used (0.029 mg/ml vs.

1.43 mg/ml, Fig. 3.7). The lower polymer concentration was needed to reduce aggregate growth rates so that relative growth rates could be calculated accurately.

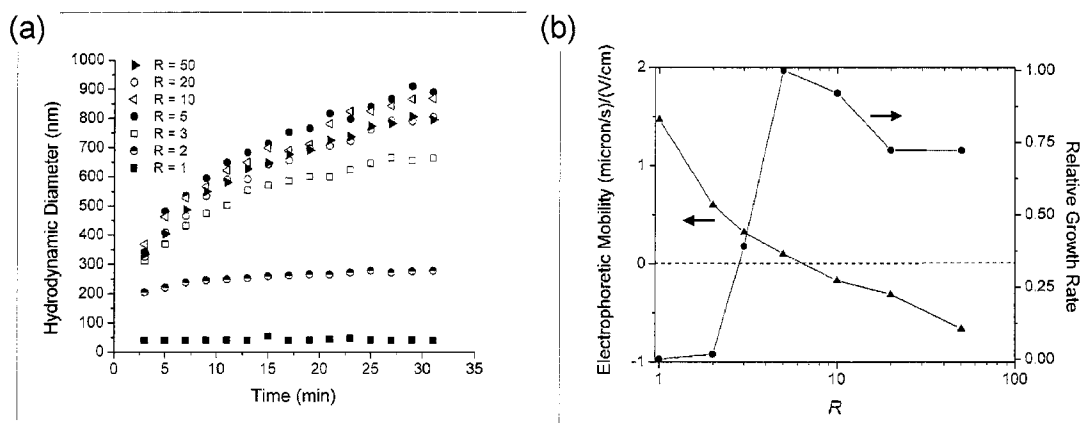


**Figure 3.6.** (a) Hydrodynamic diameter-time curves and (b) electrophoretic mobility and relative growth rates of PAH-cit aggregates as a function of  $R$ . Synthesis:  $[\text{PAH}]_{\text{final}} = 0.029 \text{ mg/ml}$ .

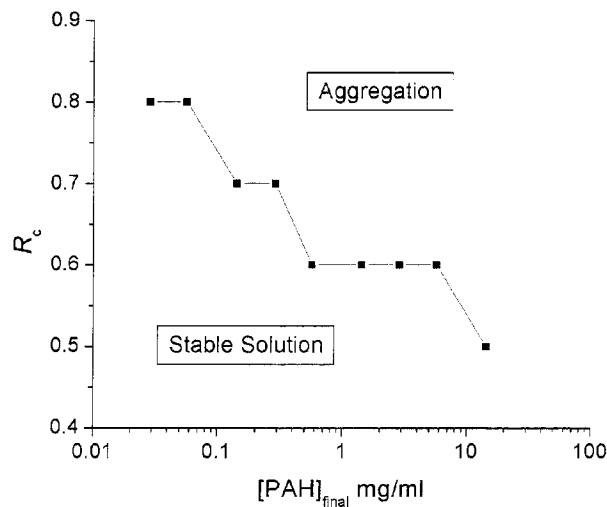


**Figure 3.7.** Critical  $R$  values plotted against polymer concentration for PAH-cit system. Data points were collected by visual inspection and laser light scattering.

The aggregate growth rate increased from near-zero at  $R = 1$  to a maximum at  $R = 5$ , decreased above  $R = 5$ , and leveled off at 75% of the maximum growth rate at  $R = 20$

(Fig. 3.6b). To understand this growth rate dependence on  $R$ , we characterized the polymer aggregate surface charge via electrophoretic mobility ( $\mu_E$ ) measurements. Calculated from the measured velocity  $v$  of the charged colloids in an applied external electric field ( $E = \mu_E \times v$ ), electrophoretic mobility reflects the overall charge of a colloidal surface and surface-bound counterions. The large  $\mu_E$  values of the PAH-cit aggregates at low  $R$  ratios indicated the aggregate surface was highly positively charged (Fig. 3.6b). As the  $R$  ratios increased, the surface charge became less positively charged until about  $R = 5$ , at which point the aggregates had an overall neutral surface charge. Above  $R = 5$ , the aggregates assumed a net negative charge, arising from citrate anions binding to the surface.

We found that the growth rate of the PAH aggregates could be correlated to their surface charge, by treating the aggregates as charged colloidal particles. According to the DLVO theory of colloidal stability, charged particles are most susceptible to aggregation when their surfaces are the least charged, or equivalently, when the van der Waals attractive energy between the particles overcomes the repulsive energy of the charged surfaces [20,21]. Thus, it stood to reason that PAH aggregates had slow growth rates at low  $R$  ratios because their surfaces were charge stabilized against aggregation. The aggregate growth rate increased with higher  $R$  ratios as the surface charge reduced in magnitude, and reached a maximum when the net surface charge was nearly zero (Fig. 3.6b).

The growth rate then decreased as the aggregate surface became negatively charged. Higher  $R$  ratios led to a more negatively charged surface, but the growth rate did not decrease above  $R = 20$ . The presence of free, unbound citrate anions may have been

responsible for these high growth rates by increasing the overall salt concentration of the suspension, as high salt concentrations are known to reduce the electrostatic repulsion between charged particles (which leads to colloid destabilization) [22].

### 3.3.4. pH effect on PAH-salt aggregate formation

We studied the pH effect at constant salt concentration by using the three different sodium salts of citrate (trisodium, disodium, monosodium) and citric acid, and preparing PAH-cit samples at  $R = 5$  and low polymer concentrations. The salt forms all led to aggregate formation (Fig. 3.8a, curves i, iii, and iv). Citric acid did not though, as the scattering intensity of the citric acid-PAH solution was only slightly higher than that of a pure PAH solution and was similar to that of a PAH solution containing NaCl (Fig. 3.8b, samples v-vii).

The measured pH values of the PAH-cit solutions/suspensions were 7.4, 5.3, 3.9, and 3.4 for the tri-, di-, mono-sodium and citric acid samples, respectively, which indicated that pH affected the ability of polymer aggregates to form. We propose that the pH of the PAH-cit suspension dictated the ionic state of the citrate anion and therefore the population of multi-charged anions. Citric acid has  $pK_a$  values of 3.14, 4.77, and 6.39, resulting in a distribution of differently-charged citrate species as a function of solution pH (Fig. 3.8c). According to acid-base equilibrium calculations, the citrate anions were mostly in the form of trivalent  $\text{cit}^{3-}$  species when the trisodium salt was used and in the form of divalent  $\text{Hcit}^{2-}$  for the disodium salt (Fig. 3.8d). When the monosodium citrate was used, the citrate anions were mostly monovalent  $\text{H}_2\text{cit}^-$  but  $\sim 10\%$  were in divalent



form. Thus, the formation of aggregates correlated with the presence of 2- and 3- charged citrate species.

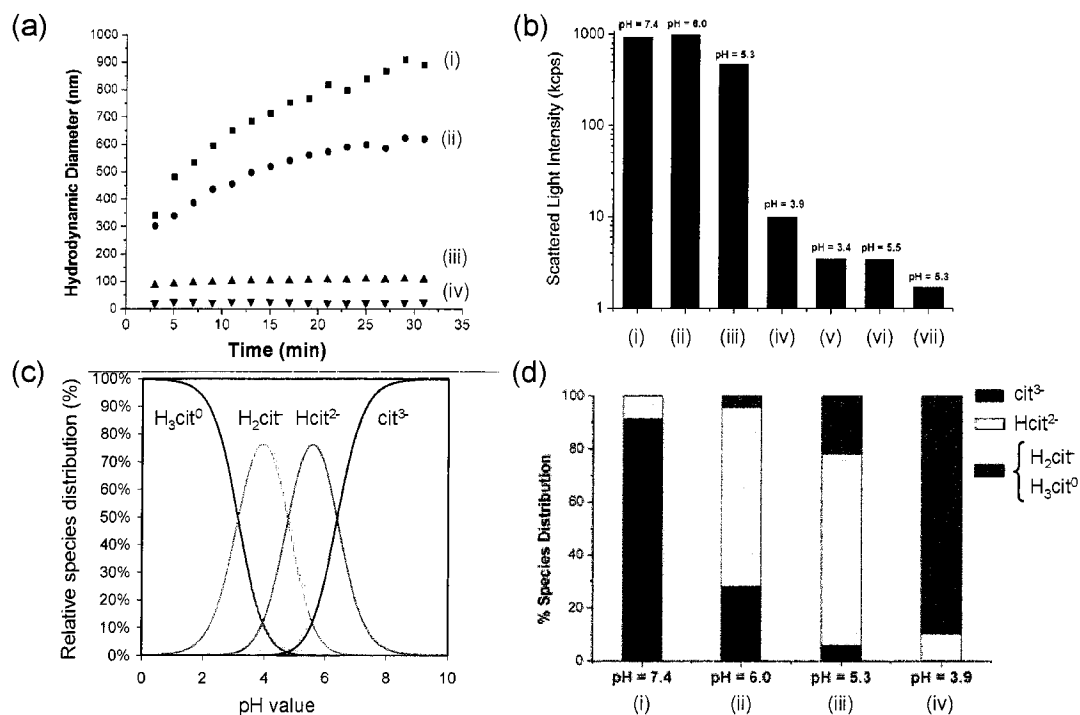


**Figure 3.8.** Effect of suspension pH on PAH-cit aggregate growth using different salts ( $[PAH]_{final} = 0.029$  mg/ml,  $[cit]_{final} = 0.51$ ,  $R = 5$ ): (a) Aggregate size as a function of aging time. (b) Scattered light intensity (log-scale) of the different PAH-citrate systems. (c) Citrate species distribution calculated as a function of pH, and (d) the calculated species distribution at the pH values of PAH-citrate systems shown in (a). The samples were prepared using (i) trisodium citrate, (ii) 50% trisodium citrate + 50% disodium citrate, (iii) disodium citrate, (iv) monosodium citrate, (v) citric acid, (vi) NaCl ( $R = 5$ ), and (vii) no salt.

In contrast to those in PAH-trisodium citrate case, the PAH-disodium citrate aggregates did not grow with time. The aggregate hydrodynamic diameter was 110 nm, according to DLS. To verify their existence, we aged the suspension for 30 min and treated with glutaraldehyde to form covalently crosslinked aggregates that could be imaged outside the water suspension. SEM analysis indicated the aggregates were ~100

nm spheres (Fig. 3.9). The PAH-monosodium citrate aggregates also did not grow with time. The scattering intensity of this suspension was significantly less than that of the PAH-disodium citrate case but higher than that of a PAH solution (Fig. 3.8b). The measured  $D_h$  of  $\sim 25$  nm suggested the presence of stable PAH-citrate aggregates composed of  $\sim 8$ -9 PAH chains.

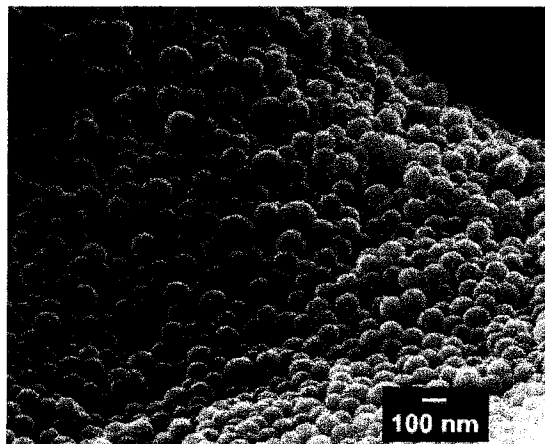


**Figure 3.9.** SEM image of spheres formed by addition of glutaraldehyde to PAH-disodium citrate aggregates. Synthesis conditions:  $[PAH]_{final} = 0.026$  mg/ml,  $[disodium\ citrate]_{final} = 0.46$  mM, aging time = 30 min,  $[glutaraldehyde]_{final} = 0.26$  M, glutaraldehyde treatment time = 24 hrs.

The aggregate growth rates varied as a function of pH value (Fig. 3.8a). Electrophoretic mobility measurements of the faster-growing PAH-trisodium citrate (pH 7.4) and slower-growing PAH-disodium citrate (pH 5.3) suspensions yielded  $\mu_E$  values of +0.09 and +0.48 ( $\mu\text{m/s}/(\text{V/cm})$ ), respectively. The (fast growth rate)/(low surface charge) and (slow growth rate)/(high surface charge) observations were thus consistent with the earlier explanation for the  $R$  effect on growth rate. As expected, an equimolar solution of disodium citrate and trisodium citrate (pH 6.0) led to PAH-cit aggregate formation with an intermediate  $\mu_E$  value (+0.37 ( $\mu\text{m/s}/(\text{V/cm})$ )) and an intermediate growth rate (Fig. 3.8a, curve ii). The  $\mu_E$  value for the non-growing, higher-pH PAH-monosodium citrate

system (pH 3.9) was expected to be greater than  $+0.48 \text{ (}\mu\text{m/s)/ (V/cm)}$ , but it could not be determined accurately due to low scattering intensity.

### **3.3.5. PAH-cit aggregate growth mechanism**

PAH-cit aggregates were found to grow in size while maintaining their spherical shape, as visualized through confocal microscopy of FITC-tagged PAH-cit (Figs. 3.10a-c) and RITC-tagged PAH-cit aggregates as a function of aging time (Figs. 3.10f-h). The growth mechanism was unclear, though. So, separate suspensions of FITC-tagged PAH-cit and RITC-tagged PAH-cit aggregates were prepared and aged for 19 min. They were combined, aged for 1 min, and imaged. The suspension was found to comprise small aggregates ( $<3 \text{ }\mu\text{m}$ ) that mostly contained either FITC (green) or RITC (red), and larger aggregates ones ( $>3 \text{ }\mu\text{m}$ ) that contained mixtures of the two dyes (Fig. 3.10d). A longer aging time led to aggregates that were larger and more homogeneous in composition (Fig. 3.10e). These images indicated that aggregate growth could have been the result of coalescence, in which the aggregates merge to form larger aggregates, or Ostwald ripening, in which larger aggregates grow while the smaller ones dissolve.

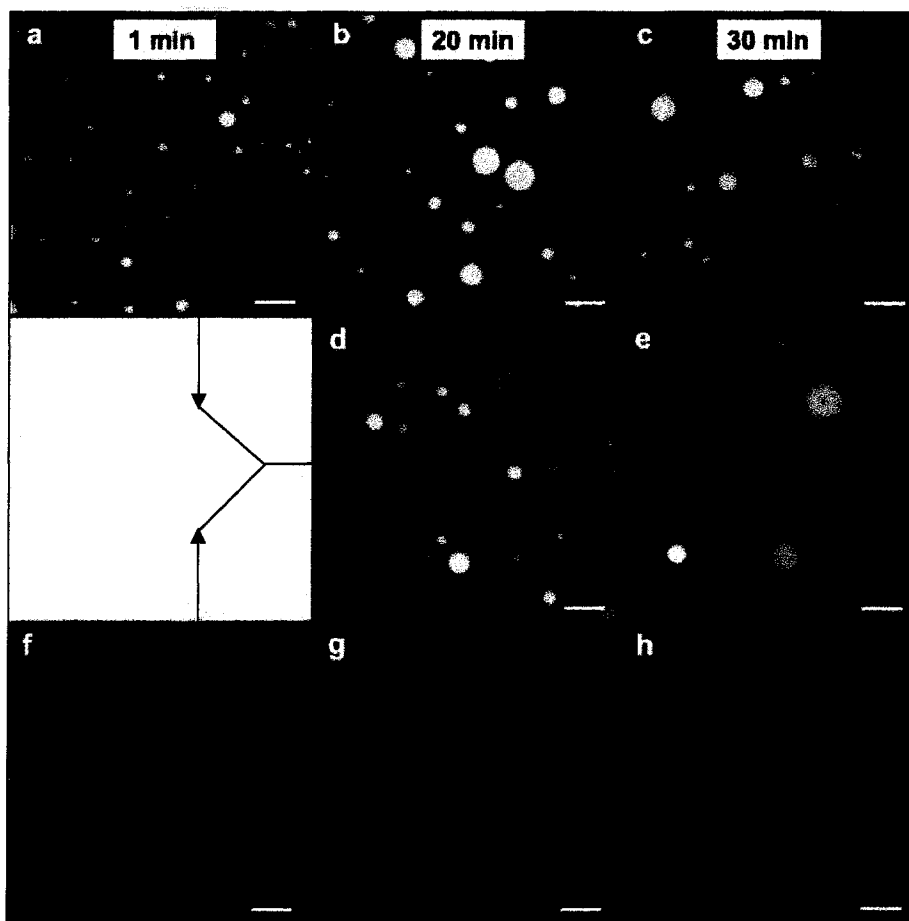


**Figure 3.10.** Confocal microscopy images of PAH-cit aggregates aged for various times (1 min, 20 min, and 30 min): FITC-tagged PAH-cit aggregates aged for (a) 1 min, (b) 20 min, and (c) 30 min; RITC-tagged PAH-cit aggregates aged for (f) 1 min, (g) 20 min, and (h) 30 min; and the resultant aggregates after combining the 19-minute-aged FITC- and RITC-tagged suspensions from (a) and (f), respectively, and aging for (d) 1 min and (e) 11 min. Synthesis:  $[\text{PAH}]_{\text{final}} = 1.43 \text{ mg/ml}$ ,  $[\text{cit}]_{\text{final}} = 10.19 \text{ mM}$ ,  $R = 2$ . Scale bars:  $10 \mu\text{m}$ .

We tested the hypothesis that the aggregates grew through coalescence, by examining the effect of PAH concentration on  $D_h$ -time curves at constant  $R$ . Based on the treatment developed for polymer melt systems by Crist and Nesarikar [23], spherical droplets with diameter  $D$  grow via coalescence or Ostwald ripening with a cube-root time dependence,  $D^3 = D_0^3 + Kt$ , where  $D_0$  is initial diameter and  $K$  is a growth mechanism-dependent rate

constant. It was shown that  $K \propto \phi$  for coalescence and  $K \propto 1/(1+0.74\sqrt{\phi})^3$  for Ostwald ripening, where  $\phi$  is the total volume fraction of the droplets in suspension.

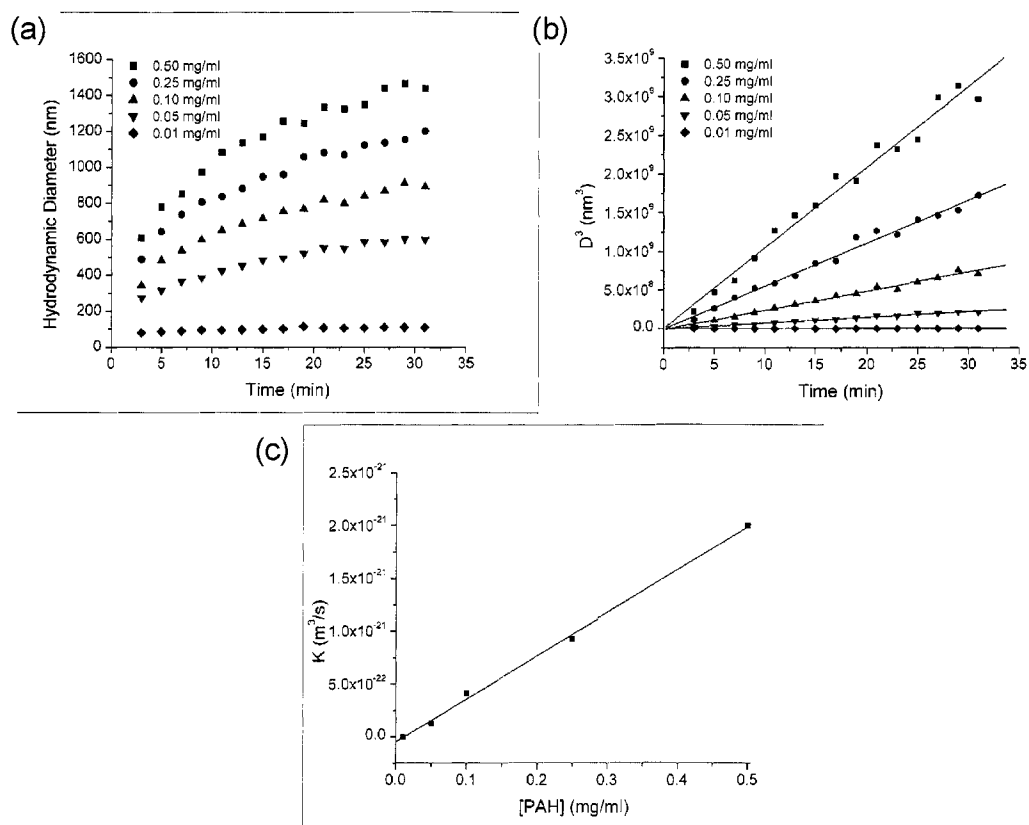
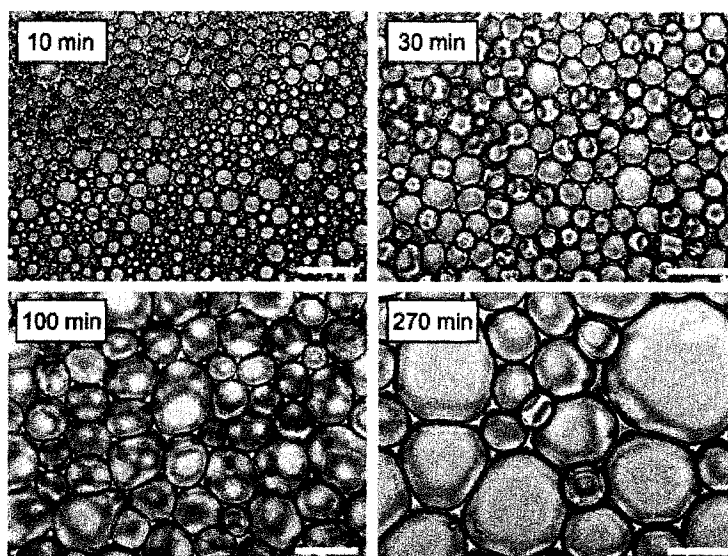


**Figure 3.11.** PAH-cit aggregate growth as a function of PAH precursor concentration: (a)  $D_h$  vs. time, (b)  $D_h^3$  vs. time, and (c) rate constant vs. polymer concentration. The highest precursor PAH concentration tested was 0.50 mg/ml, due to multiple scattering of the PAH-cit suspensions at higher PAH concentrations. Synthesis:  $[\text{PAH}]_{\text{final}} = [\text{PAH}]_{\text{precursor}} \div 3.5$ ;  $R = 5$ .

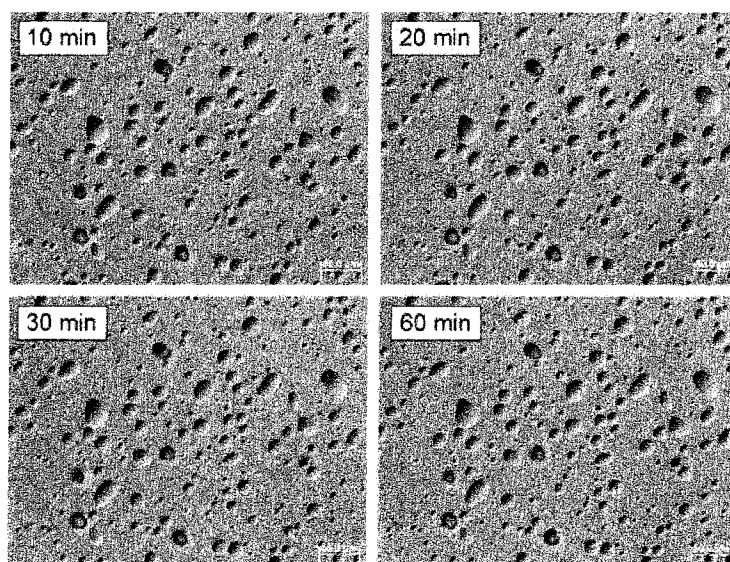
The PAH-cit aggregates were found to grow more rapidly at higher PAH concentrations (Fig. 3.11a). It could be seen that the  $D_h^3$ -time curves were linear, allowing for reasonably accurate  $K$  estimates (Fig. 3.11b). The curves extrapolated to a common  $D_0$  value of 80 nm, which suggested a common PAH-cit aggregate size after the 10-second vortex-mixing step. With the assumption that the volume fraction of PAH-cit

aggregates was proportional to the initial PAH concentration, the observation that the  $K$  rate constants increased linearly with PAH concentration (Fig. 3.11c) strongly suggested the coalescence growth mechanism.

Real-time studies on PAH-cit aggregate growth through optical microscopy provided additional evidence for coalescence. A concentrated PAH-cit suspension was made by adding 125  $\mu\text{l}$  of  $\text{Na}_3\text{cit}$  solution (71.3 mM,  $R = 1.2$ ) to 50  $\mu\text{l}$  of PAH solution (40 mg/ml), and vortex-mixed for 10 sec. A drop of the highly turbid suspension was deposited on a glass slide and left sitting for 2 min, and excess suspension was lightly rinsed with water [24]. The high PAH concentration ensured a dense packing of aggregates on the glass slide, which was difficult to prepare using lower PAH concentrations. The glass slide-bound aggregates appeared as droplets at early times (Fig. 3.12a). They deformed upon contact with one another, and underwent coalescence very slowly (Fig. 3.12b-d). This coalescence behavior is reminiscent of surfactant-containing oil-in-water emulsions [22,25,26]: (i) droplets approach one another and deform; (ii) the liquid film between the flat surfaces of the droplets starts draining; (iii) the surfaces make physical contact and fuse to form a neck, and (iv) the neck grows such that the two droplets re-form into a spherical droplet. PAH-cit aggregate coalescence may be slow due to the charged nature of the droplet surface. We then probed the existence of Ostwald ripening by depositing PAH-cit aggregates (same concentrations as above) on a glass slide at a low surface density such that there was no droplet-droplet contact (Fig. 3.13) [27]. We did not observe any change in aggregate size expected for Ostwald ripening.



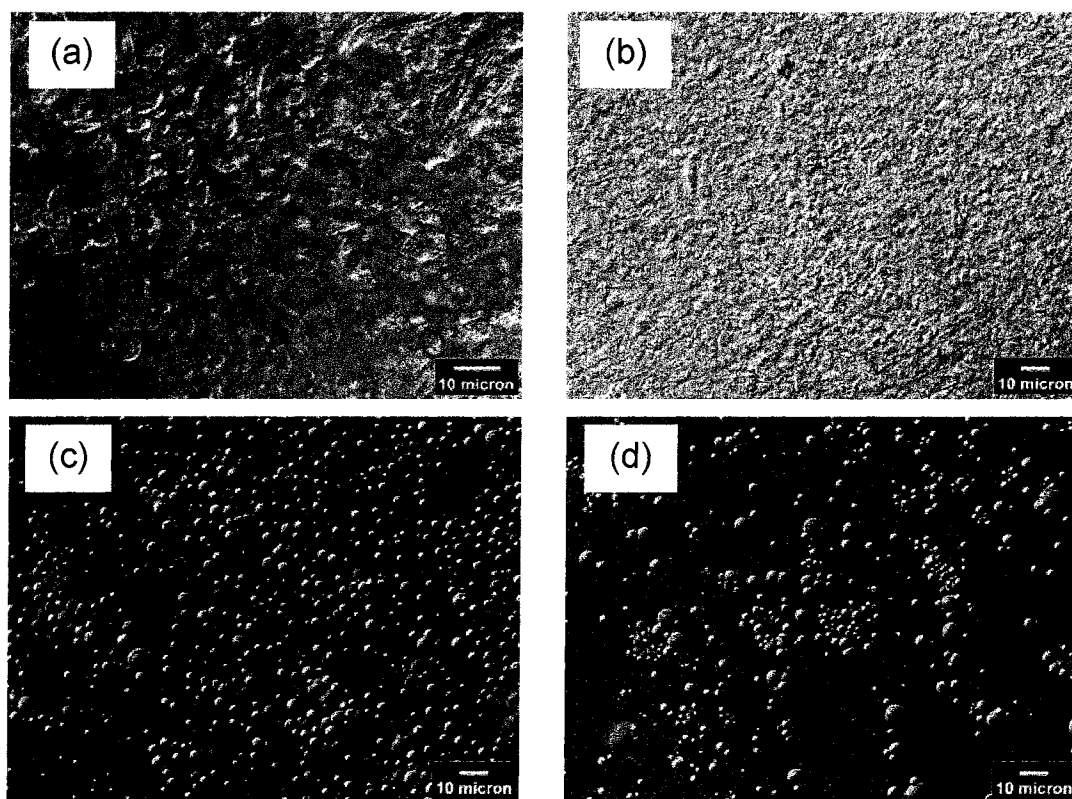
**Figure 3.12.** Time-lapse brightfield microscopy images of concentrated PAH-cit aggregate "droplets." The field of view did not change. Time zero corresponds to when the 10-second vortex mixing stopped. Synthesis:  $[\text{PAH}]_{\text{final}} = 11.43 \text{ mg/ml}$ ,  $[\text{cit}]_{\text{final}} = 50.9 \text{ mM}$  ( $R = 1.2$ ). Scale bar:  $50 \text{ }\mu\text{m}$ .



**Figure 3.13.** Time-lapse differential interference contrast images of PAH-cit aggregates (low coverage of glass slide). Time  $t = 0$  corresponds to the time when the 10 sec vortex mixing of PAH-cit solution was stopped. Synthesis conditions:  $[\text{PAH}]_{\text{final}} = 11.4 \text{ mg/ml}$ ,  $[\text{cit}]_{\text{final}} = 50.9 \text{ mM}$ ,  $R = 1.2$ . Scale bar:  $50 \text{ }\mu\text{m}$ .

### 3.3.6. Effects of PAH-cit aggregate aging time and $R$ ratio on capsule size

The formation of the NAC shell depended on the  $R$  ratio of the PAH-cit samples (Fig. 3.14). After  $\text{SiO}_2$  NP sol addition, disordered silica/polymer precipitate resulted at  $R = 0$  and  $R = 0.3$ , since no PAH-cit aggregates were formed below the critical  $R$  ratio of 0.6. Silica/polymer microcapsules, on the other hand, resulted for  $R$  ratios greater than the critical  $R$  ratio. No obvious morphological differences in the NACs synthesized at the different  $R$  values were observed. The capsules were formed whether the electrophoretic mobilities were positive or negative in value, reinforcing the fact that electrophoretic mobility measurements provide only average values and do not account for charge heterogeneity of the surface.





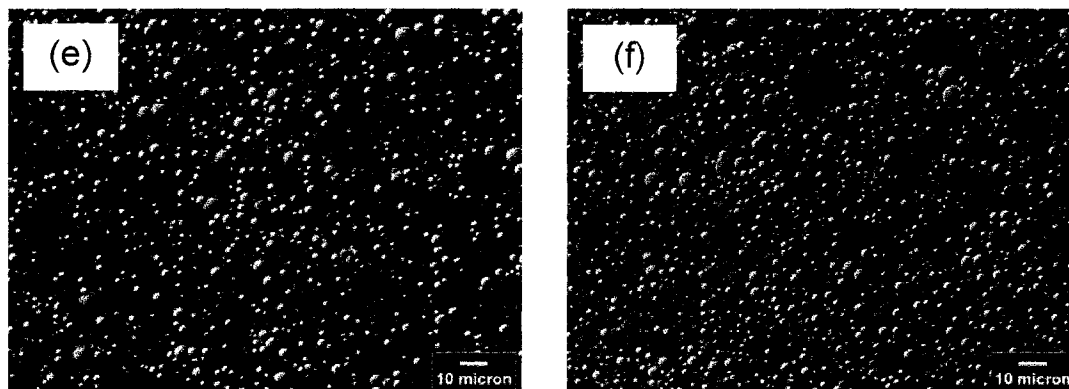


**Figure 3.14.** Optical microscopy images of product formed after combining SiO<sub>2</sub> NPs with PAH-cit samples of varying  $R$  ratios: (a)  $R = 0$ , (b)  $R = 0.3$ , (c)  $R = 1$ , (d)  $R = 5$ , (e)  $R = 10$ , and (f)  $R = 20$ . Critical ratio  $R_c = 0.6$ .  $[\text{PAH}]_{\text{final}} = 0.83 \text{ mg/ml}$ ,  $[\text{SiO}_2 \text{ NP}]_{\text{final}} = 8.5 \text{ wt.}\%$ , aging time after NP addition = 30 min.

Finally, we studied the effect of PAH-cit aggregate aging time on microcapsule size (Fig. 3.15). Based on SEM analysis of >1000 glutaraldehyde-treated PAH-cit aggregates, they had a mean diameter of  $0.85 \mu\text{m}$  (standard deviation  $\sigma = 0.38 \mu\text{m}$ ) after aging for 10 sec, and a mean diameter of  $2.93 \mu\text{m}$  ( $\sigma = 1.10 \mu\text{m}$ ) after aging for 30 min (Fig. 3.15c,f). The polymer aggregates broadened in size with aging time. Addition of SiO<sub>2</sub> NPs to 10-sec-aged and 30-min-aged aggregates led to NACs with mean diameters of  $2.1 \mu\text{m}$  ( $\sigma = 1.1 \mu\text{m}$ ) and  $3.3 \mu\text{m}$  diameter ( $\sigma = 1.8 \mu\text{m}$ ), respectively. The capsule structure were similar (*i.e.*, spherical shell shape and core interior contained polymer), and the NAC sizes correlated to aggregate aging time.

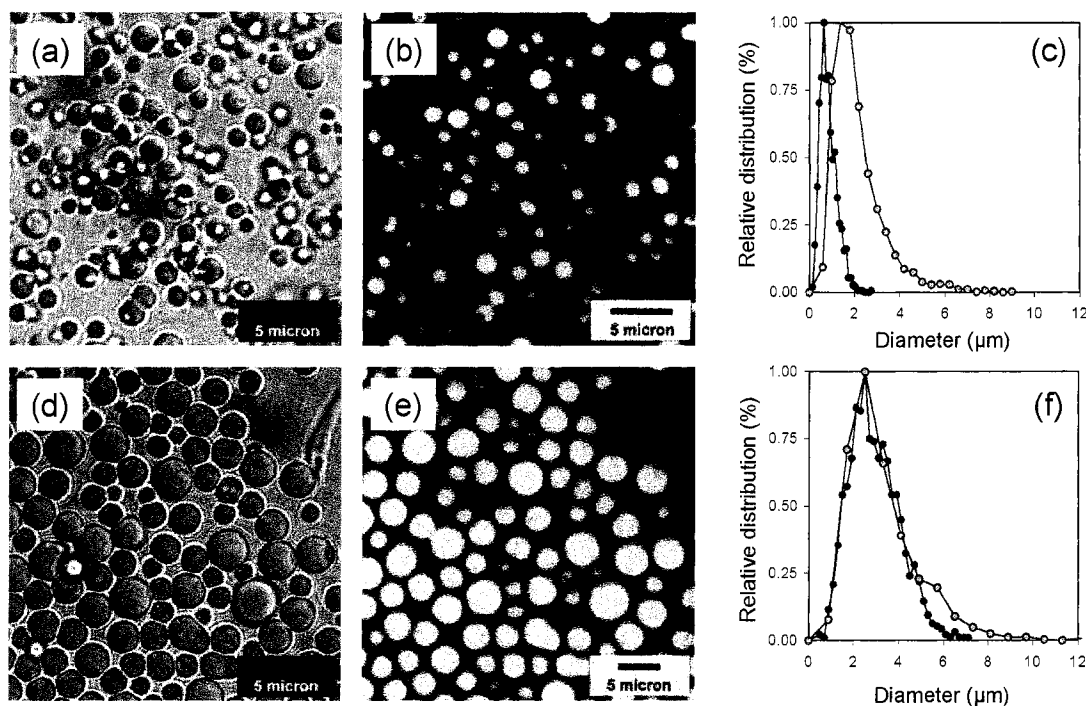


**Figure 3.15.** Brightfield and confocal microscopy images of NACs prepared from PAH-FITC-cit aggregates aged for 10 sec (a,b) and 30 min (d,e). (c,f) Size distributions of PAH-cit aggregates (filled circles) aged for 10 sec and 30 min, respectively, and the resultant NACs (open circles).  $[\text{PAH}]_{\text{final}} = 0.83 \text{ mg/ml}$ ,  $[\text{cit}]_{\text{final}} = 5.94 \text{ mM}$ ,  $[\text{SiO}_2 \text{ NP}]_{\text{final}} = 8.5 \text{ wt\%}$ , aging time after NP addition = 30 min.

The relationship between NAC and aggregate diameters was less clear. For the 10-sec-aged system, the difference in aggregate and NAC diameters suggested a shell thickness of 600 nm, which was larger than the 100-250 nm thicknesses typically observed in PAH-based NACs (Fig. 3.16). For the 30-min-aged system, the difference in diameters suggested a shell thickness of 200 nm. This calculation may be misleading as the size distributions of the aggregates and NACs mostly coincided but the positive skew of the size distribution led to a larger NAC mean diameter. A detailed study of the shell formation step and the NAC structure is ongoing.

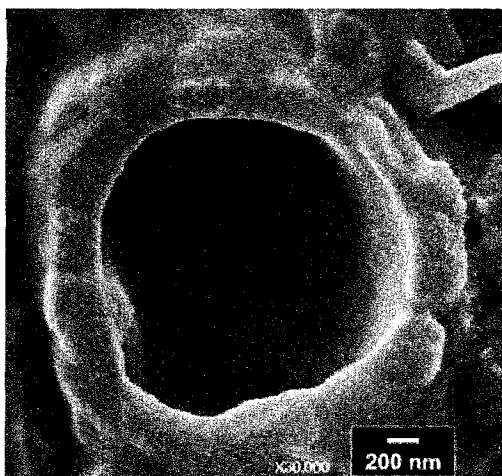


**Figure 3.16.** SEM image of an ultramicrotomed capsule. The NACs were prepared from PAH-cit aggregates and SiO<sub>2</sub> NPs. [PAH]<sub>final</sub> = 0.83 mg/ml, [cit]<sub>final</sub> = 5.94 mM,  $R = 2$ , aggregate aging time = 30 min, [SiO<sub>2</sub> NP]<sub>final</sub> = 8.5 wt%.

### 3.4. Conclusions

The room-temperature formation of PAH-salt aggregates is readily performed by mixing the respective solutions together at appropriate charge ratio  $R$  and pH values. To the first approximation, the formation can be understood on the basis of electrostatic attractions between positively charged PAH and multiply charged anions, and of electrostatic interactions between the charged PAH-salt aggregates. The anions bind to the PAH backbone via counterion condensation, and the resulting PAH-salt complexes combine to form colloidal aggregates. These aggregates grow as a function of time with the growth rates dependent on their surface charge. The coalescence mechanism for aggregate growth is supported by DLS measurements and optical studies of concentrated PAH-citrate aggregate suspensions that resemble emulsions. The polymer aggregates behave as soft templates for NACs formation, such that aggregate aging time controls capsule diameter. This fuller understanding of the electrostatic chemistry involved in polymer aggregate formation is important in controlling microcapsule structure, and should be

helpful in understanding the formation of other charge-assembled materials, like DNA-salt aggregates and complex coacervates.

### 3.5. References

- [1] Rana, R.K., Murthy, V.S., Yu, J., Wong, M.S. Nanoparticle self-assembly of hierarchically ordered microcapsule structures *Advanced Materials*, **2005**, *17*, 1145.
- [2] McKenna, B.J., Birkedal, H., Bartl, M.H., Deming, T.J., Stucky, G.D. Micrometer-sized spherical assemblies of polypeptides and small molecules by acid-base chemistry *Angewandte Chemie-International Edition*, **2004**, *43*, 5652.
- [3] Patwardhan, S.V., Clarson, S.J. Silicification and biosilicification - Part 1. Formation of silica structures utilizing a cationically charged synthetic polymer at neutral pH and under ambient conditions *Polymer Bulletin*, **2002**, *48*, 367.
- [4] Brunner, E., Lutz, K., Sumper, M. Biomimetic synthesis of silica nanospheres depends on the aggregation and phase separation of polyamines in aqueous solution *Physical Chemistry Chemical Physics*, **2004**, *6*, 854.
- [5] Rodriguez, F., Glawe, D.D., Naik, R.R., Hallinan, K.P., Stone, M.O. Study of the chemical and physical influences upon in vitro peptide-mediated silica formation *Biomacromolecules*, **2004**, *5*, 261.
- [6] Kröger, N., Lorenz, S., Brunner, E., Sumper, M. Self-assembly of highly phosphorylated silaffins and their function in biosilica morphogenesis *Science*, **2002**, *298*, 584.
- [7] Manning, G.S. Counterion binding in polyelectrolyte theory *Accounts of Chemical Research*, **1979**, *12*, 443.
- [8] Bhuiyan, L.B., Vlachy, V., Outhwaite, C. Understanding polyelectrolyte solutions: macroion condensation with emphasis on the presence of neutral co-solutes *International Reviews in Physical Chemistry*, **2002**, *21*, 1.

- [9] Olvera de la Cruz, M., Belloni, L., Delsanti, M., Dalbiez, J.P., Spalla, O., Drifford, M.J. Precipitation of highly-charged polyelectrolyte solutions in the presence of multivalent salts *Journal of Chemical Physics*, **1995**, *103*, 5781.
- [10] Spohr, E., Hribar, B., Vlachy, V. Mechanism of macroion-macroion clustering induced by the presence of trivalent counterions *Journal of Physical Chemistry B*, **2002**, *106*, 2343.
- [11] Schmitz, K.S., *Macroions in Solution and Colloidal Suspension*, VCH, New York, **1993**.
- [12] Xia, J.L., Dubin, P.L., Havel, H.A. Electrophoretic light-scattering study of counterion condensation on polylysine *Macromolecules*, **1993**, *26*, 6335.
- [13] Solis, F.J., Olvera de la Cruz, O. Collapse of flexible polyelectrolyte in multivalent salt solutions *Journal of Chemical Physics*, **2000**, *112*, 2030.
- [14] De Robertis, A., De Stefano, C., Giuffre, O., Sammartano, S. Binding of carboxylic ligands by protonated amines *Journal of Chemical Society-Faraday Transactions*, **1996**, *92*, 4219.
- [15] De Stefano, C., Giuffre, O., Sammartano, S. Delta G degrees and T Delta S degrees charge relationships for the binding of carboxylic anions by open-chain polyammonium cations *Journal of Chemical Society-Faraday Transactions*, **1998**, *94*, 2395.
- [16] De Robertis, A., De Stefano, C., Giuffre, O., Sammartano, S. Dependence on ionic strength of polyamine protonation in NaCl aqueous solution *Journal of Chemical and Engineering Data*, **2001**, *46*, 1425.
- [17] Nordmeier, E. Advances in polyelectrolyte research - Counterion binding phenomenon, dynamic processes, and the helix-coil transition of DNA *Macromolecular Chemistry and Physics*, **1995**, *196*, 1321.
- [18] Porasso, R.D., Benegas, J.C., van den Hoop, M., Paoletti, S. Chemical bonding of divalent counterions to linear polyelectrolytes: Theoretical treatment within the counterion condensation theory *Physical Chemistry Chemical Physics*, **2001**, *3*, 1057.

- [19] Lefaux, C.J., Zimmerlin, J.A., Dobrynin, A.V., Mather, P.T. Polyelectrolyte spin assembly: Influence of ionic strength on the growth of multilayered thin films *Journal of Polymer Science Part B-Polymer Physics*, **2004**, 42, 3654.
- [20] Hiemenz, P.C., Rajagopalan, R., *Principles of Colloid and Surface Chemistry*, 3rd ed., Marcel Dekker, Inc., New York, **1997**.
- [21] Hunter, R.J., *Foundations of Colloid Science*, 2nd ed., Oxford University Press, New York, **2001**.
- [22] Evans, D.F., Wennerstrom, H., *The Colloidal Domain: Where Physics, Chemistry, Biology, and Technology Meet*, 2nd ed., Wiley-VCH, New York, **1999**.
- [23] Crist, B., Nesarikar, A.R. Coarsening in polyethylene copolymer blends *Macromolecules*, **1995**, 28, 890.
- [24] The high PAH concentration ensured a dense packing of aggregates on the glass slide.
- [25] Sjoblom, J. *Encyclopedic Handbook of Emulsion Technology*; Marcel Dekker: New York, **2001**
- [26] Bibette, J., *Emulsion science: Basic principles: Overview*, Springer, New York, **2002**.
- [27] Kabalnov, A.S., Pertzov, A.V., Shchukin, E.D. Ostwald ripening in emulsions. 1. Direct observation of Ostwald ripening in emulsions *Journal of Colloid and Interface Science*, **1987**, 118, 590.

## **Chapter 4. Encapsulation of enzymes in nanoparticle-assembled capsules\***

### **4.1. Introduction**

Immobilization of enzymes in robust solid supports has captured the attention of material scientists and biochemists for almost three decades [1,2]. Broadly speaking, bioimmobilization involves either trapping the individual enzyme molecules within solid support materials or physically binding the enzymes on the surface of the supports in order to restrict their freedom of movement. The evident advantages of such a procedure are: enhanced enzymatic stability in deleterious environments such as in the presence of inhibitors or proteases, recoverability and re-use (especially if the enzyme is scarce and expensive), increase in enzyme shelf life, prevention of product contamination, and not to mention the ease of handling and storage [3-5]. Furthermore, these enzyme-containing supports can be used as sensors, devices for diagnostics, for therapeutics, and even in the form of artificial tissues or organ implants [6-9]. The ever-increasing applications and markets for immobilized enzymes are providing a conducive environment for development of new and improved immobilization techniques.

A few of the prerequisites expected of this process to be of any practical utility are: the enzyme should retain its activity while trapped, the reactant molecules should be able to freely diffuse in and out of the solid substrate, and the support material itself should not be susceptible to environmental degradation. Currently, the overriding goals in this field have been to carry out the immobilization under mild conditions (aqueous medium, near-neutral pH, room temperature) involving minimum number of synthesis steps,

---

\* Murthy, V.S. and Wong, M.S. *ACS Symposium Series on Nanoscale Science and Technology in Biomolecular Catalysis*, book chapter to be submitted.

increasing enzyme loading, increasing surface area of the support material to improve enzyme–reactant contact, decreasing the inactivation or leaking of the enzyme, and to scale up the immobilization process making it amenable to commercial set-up [4,7,10]. In order to accomplish these, a number of techniques for immobilizing enzymes have been developed which can be categorized under five headings: (1) covalent binding to the support, (2) physical adsorption, (3) microencapsulation, (4) physical entrapment, and (5) crosslinking [1,4,5,7].

#### **4.1.1. Covalent binding**

This method is the most widespread and involves the formation of covalent bonds between the enzyme and the support material. The groups participating in the bond formation are the amino acid residues on the enzyme and the functional groups on the support. The selection of conditions for immobilization by covalent binding is more difficult than in other carrier binding methods. The reaction conditions required are relatively complicated and not usually mild [7]. The bond formation with the support matrix should involve only functional groups of the enzyme that are not essential for its catalytic action and thus the active site should be unaffected by the various reagents used. Another requirement for good enzyme coupling is the physical adsorption of the enzyme on the substrate prior to covalent coupling [5]. A large number of support materials are available commercially such as polysaccharide polymers (alginate, chitosan, agarose, cellulose, dextran, starch), proteins (silk, gelatin, collagen), porous silica, synthetic polymers (polyacrylamide, polyamides, methacrylates), and inorganic minerals (clay, Kieselgur, bentonite) [7]. The wide variety of binding reactions and a plethora of



matrices with functional groups capable of covalent coupling, or susceptible to being activated to give such groups, makes this a generally applicable method of immobilization.

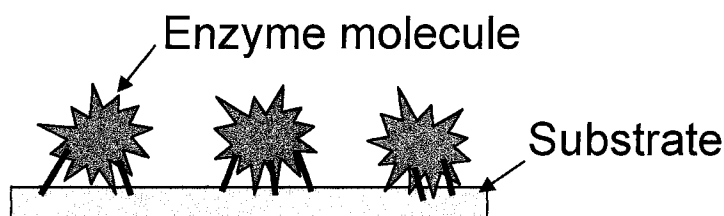


**Figure 4.1.** Schematic showing the enzyme molecules covalently bound to the substrate.

#### 4.1.2. Physical adsorption

Immobilization by surface adsorption is the simplest of all techniques. The forces involved are a combination of ionic, van der Waals, hydrogen bonding, and hydrophobic interactions. Even though each of these forces is weak compared to covalent binding, put together, they are sufficient to achieve a strong enough adhesion for practical systems. Since the existing non-covalent interactions between the enzymes and support is utilized, no chemical modifications is required and little damage is done to enzymes *via* this technique. The procedure consists of mixing together the enzymes and a support material with favorable adsorption properties under suitable conditions of pH and ionic strength for a certain period of incubation, followed by washing steps to remove any excess unbound molecules. Commonly used supports are alumina, glass, mesoporous silica, titania, collagen, derivatives of carbon (activated carbon, charcoal) and lectin [7,11,12]. Thus, this technique is simple, low-cost, quick to yield the final product, and allows for facile regeneration of the support. On the other hand, weak and non-specific binding leads to desorption of enzymes under high ionic strength or drastic pH and temperature

conditions. This desorption can also be caused during a reaction, either when the conformation of the enzyme changes, or during accumulation of the product. Physical working conditions such as agitation, high flow rates, and particle-particle abrasion can also lead to desorption of the enzymes. Under conditions where the substrate or the product is charged and interacts with the support, the desorption gets aggravated. The diffuse layer of substrate and product electrostatically bound to the enzyme and support can also lead to mass transfer limitations. The ionic binding of protons can lead to local pH inhomogeneities which may be an important consideration for enzymes with specific pH requirements. These constraints make the general applicability of the physical adsorption technique quite low.

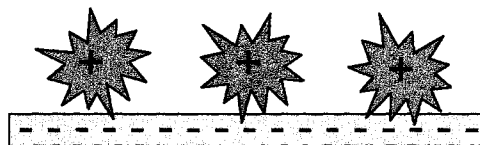


**Figure 4.2.** Schematic showing physical adsorption of enzyme molecules on the substrate.

#### 4.1.3. Encapsulation

Encapsulation may be considered as trapping the enzyme molecules in tiny containers whose shell walls are semi-permeable. The large proteins cannot leak out but at the same time smaller substrate molecules can readily diffuse inside the shell, react with the enzyme, and the products can diffuse out. A variety of materials have been used to synthesize capsules in the size range of 100 nm to 100  $\mu\text{m}$  (collectively called “microcapsules”). Microcapsules, due to their small size, and hence larger surface area, become especially useful for therapeutics where they can be administered to the body intravenously or through dermal absorption [13]. Encapsulation of enzymes can be

achieved by coacervation (or phase separation), interfacial polymerization, liquid drying, or within thermodynamically self-assembled hollow structures such as liposomes and vesicles [14-16]. Liposomes in general are not physically stable in high ionic strength solutions or even when they are taken out of solution conditions and dried. This makes it mandatory to crosslink their shell, which is a non-trivial process. Recently, Caruso et al. reported a new technique wherein oppositely charged polyelectrolytes were sequentially adsorbed onto enzyme crystals by a layer-by-layer technique [17]. This technique, even though appears quite general, is time intensive and leads to physically unstable spheres. Compared to other techniques, the synthesis conditions involved in microencapsulation are relatively mild. However, challenges with diffusion limitations across the semi-permeable membranes due to stagnant boundary layer formation, both outside and inside the capsule, are yet to be surmounted.

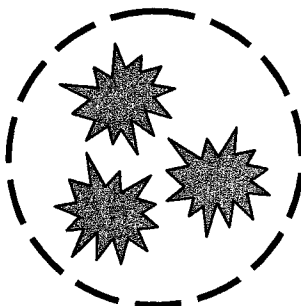


**Figure 4.3.** Schematic showing encapsulation of enzymes.

#### **4.1.4. Physical entrapment**

Immobilization by entrapment differs from adsorption and covalent binding in that the enzyme molecules are free in solution, but greatly restricted in movement by the lattice structure of the matrix. The pore sizes of the solid matrix is such as to ensure that the structure is tight enough to prevent leakage of the enzyme, yet at the same time allow

free movement of the substrate and product. Inevitably, the support will act as a mass transfer barrier, and although can lead to serious implications, it can have useful advantages since harmful cells and proteases are prevented from interaction with the immobilized enzyme [7]. The general methods of entrapment are by gelation of macromolecules (e.g., alginate, gelatin, agarose, chitin), organic polymerization (e.g., polyacrylamide), and precipitation from an immiscible solvent (e.g., polystyrene) [7,18,19]. Sol-gel techniques (mainly with silicate matrix in the form of xerogels and aerogels) have seen tremendous growth recently owing to the bridging of well known chemistry of ceramics and other inorganic materials on one hand with the current interest in bioactive materials on the other [6,10,20-27]. Enzyme entrapment in mesoporous silica [28,29] and supports made from biomimetic polymers/silica [30] have also been investigated. However, the issues with material brittleness, narrow pore structure imposing diffusion limitations, and leaking of the enzymes remain with this technique. In addition, there is a likelihood of physical adsorption of the enzyme on the support material.

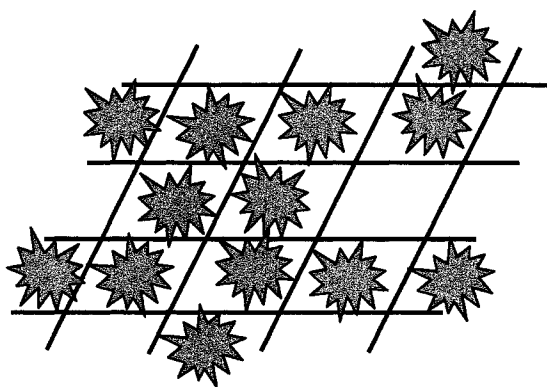


**Figure 4.4.** Schematic showing physical entrapment of enzymes in a substrate matrix.

#### 4.1.5. Crosslinking

This type of immobilization is devoid of any support and relies on coupling the individual enzyme molecules to form macroscopic aggregates. This can be achieved by chemical techniques (covalent crosslinking by glutaraldehyde or toluene diisocyanate) or physical methods (flocculation). The toxicity of chemical reagents becomes a limiting factor at industrial scales. Physical methods such as flocculation are well known in the biotechnology arena. Flocculating agents such as polyamines, polystyrene sulfonates, and various phosphates have been used extensively and well characterized. Physical or chemical crosslinking is rarely used as the only means of immobilization due to their lack of mechanical properties and poor stability [1].

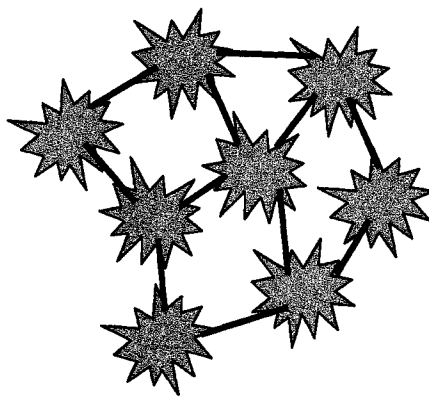


**Figure 4.5.** Schematic showing the crosslinking of enzyme molecules.

It becomes apparent that there is an impending need to use a combination of different immobilization approaches in order to overcome the challenges posed by any single technique. With that in mind, we have developed a new enzyme immobilization route which marries the techniques of encapsulation, adsorption, and physical entrapment [31]. This new route is based on the concept of trapping enzymes within capsular structures prepared from the assembly of nanoparticles (NPs) and cationic polymers. We recently

demonstrated a facile two-step synthesis of nanoparticle-assembled capsules (NACs). In this synthesis route aqueous polyamine solutions when combined with multivalent anions yield spherical polymer-salt aggregates. Upon combining these aggregates with negatively charged NPs, robust NACs were obtained almost instantaneously. The benign synthesis conditions (aqueous environment, room temperature, no organic solvents involved, near neutral pH) and rapid generation of NACs (within minutes) combined with easily obtainable precursors should lead to non-damaging encapsulation of sensitive molecules such as enzymes [31,32].

In this Chapter, I discuss the synthesis and characterization of enzyme-containing NACs. The general strategy is to introduce the enzyme molecules to the polymer-salt aggregates prior to NP shell formation. Acid phosphatase was used as the model enzyme and its encapsulation in NACs was demonstrated successfully. Results on catalytic activity of encapsulated enzyme will be presented along with studies on encapsulation efficiency and loading. Recoverability and re-use of the encapsulated enzyme will be demonstrated as well.

It was not apparent as to whether the enzyme was located in the NAC core, shell, or even both. In order to ascertain the region of localization of acid phosphatase in NACs, studies were carried out with a model protein with similar size and charge parameters as the enzyme molecule. By substituting acid phosphatase with bovine serum albumin (BSA) conjugated to a fluorescent dye, fluorescein isothiocyanate, we were able to visually establish to the first approximation, the assembly of enzyme molecules within the NACs.

## 4.2. Experimental Section

### 4.2.1. Materials

Poly(*L*-lysine hydrobromide) (195,000 g/mol, bromide counterion, “PLL”), poly(*L*-lysine hydrobromide) conjugated with fluorescein isothiocyanate (68,600 g/mol, bromide counterion, “PLL-FITC”), acid phosphatase (from potato, 7 units/mg of solid, “AP”), 4-nitrophenyl phosphate (disodium salt, “4-NPP”), citrate buffer solution (pH 4.8, 0.09 M), bovine serum albumin conjugated to fluorescein isothiocyanate (67,000 g/mol, “BSA-FITC”), protease solution (from *Bacillus* sp.,  $\geq 16$  U/g) were all procured from Sigma-Aldrich and were used without further purification. Stock solutions of BSA-FITC (20 mg/ml) and enzyme (10.6 mg/ml) were prepared in 0.01 wt % sodium azide aqueous solution to prevent microbial degradation. Trisodium citrate (“cit”) was obtained from Fisher Scientific. A 10 mM solution of fluorescein diphosphate (purchased from Anaspec, “FDP”) was prepared using citrate buffer solution (pH 4.8), divided into 100  $\mu$ l aliquots and frozen. SiO<sub>2</sub> NP (Snowtex-O, Nissan Chemicals) was available as aqueous colloidal suspension (20.5 wt.%, pH 3.4, ionic strength  $I = 16.9$  mM). The NPs measured  $13 \pm 3$  nm in diameter, according to dynamic light scattering. Zeta potential of SiO<sub>2</sub> NPs in the original sol condition was calculated from its electrophoretic mobility ( $-1.4$  ( $\mu$ m/sec)/V/cm)) to be -16 mV in the Henry’s limit.

### 4.2.2. Synthesis and enzyme assay

A typical synthesis protocol for enzyme-containing NACs was as follows: 21  $\mu$ l of PLL (2 mg/ml in water) was mixed with 125  $\mu$ l of cit (5.36 mM) by vortex mixing at low speeds (“5” speed on a scale from 1 to 10) for 10 seconds. The lightly turbid suspension

was aged for 20 min without stirring or shaking. 50  $\mu$ l of acid phosphatase solution (initial concentration varying from 0.1 to 1.6 mg/ml) was then added and the solution was mixed gently. After aging for 10 min, 125  $\mu$ l of silica NP sol was added and rapidly vortex mixed for 20 seconds at “7” speed. The resulting enzyme-containing NACs were aged for 2 hrs and thoroughly washed with DI water to get rid of excess enzyme and SiO<sub>2</sub> NPs. For encapsulating BSA protein, the enzyme was substituted with 50  $\mu$ l of BSA-FITC solution (initial concentration of 20 mg/ml).

Enzyme content was determined through a standard enzyme activity assay [33]. The enzyme-containing NACs were washed two times with water. The supernatant from the NAC washes was added to 15 ml of 4-NPP (2 mM solution in citrate buffer, pH 4.8) and magnetically stirred at room temperature. 30  $\mu$ l aliquots of the resulting solution were taken at different times (0, 2, 4, 6, 8, and 10 min) and added to 3 ml of NaOH solution (resulting in a pH of 10.0). After mixing the solutions, the absorbance at 405 nm was measured via UV-vis spectroscopy. Proper control experiments were carried out to ensure that residual SiO<sub>2</sub> NPs, PLL, and cit did not affect enzyme activity. The concentration of the enzyme and relative enzymatic activity was calculated by comparing the slope of the curve with the calibration curve.

Encapsulation efficiency was defined as the percentage of enzyme molecules encapsulated in the NACs out of the total enzyme added, which was calculated from assay explained above. Enzyme loading was defined as the ratio of the weight of the enzyme encapsulated to the total weight of the enzyme-containing NACs.



For *in situ* fluorescence microscopy, FDP solution (0.1 mM solution in citrate buffer) was added to a suspension of enzyme-containing NACs. The suspension was deposited on a poly-lysine coated glass slide and observed through fluorescence microscope.

#### 4.2.3. Characterization

**Confocal Laser Scanning Microscopy.** Confocal images were captured with Carl Zeiss LSM 510 inverted microscope equipped with a 100× oil immersion objective (NA = 1.4). The laser excitation wavelength of 488 nm was chosen for FITC ( $\lambda_{\text{ex}} = 494.5$  nm,  $\lambda_{\text{em}} = 519$  nm). Samples were mounted on conventional glass slides and sealed under a cover slip to prevent drying. All samples were prepared 1-2 hrs prior to imaging.

**Electrophoretic mobility measurement.** Electrophoretic mobility was measured using phase analysis light scattering (PALS), a variation of electrophoretic dynamic light scattering (DLS). Zeta potential measurements were calculated from electrophoretic mobility measurements using Henry's equation (i.e.,  $0.1 \leq \kappa a \leq 100$ , where  $\kappa$  is the Debye-Hückel parameter and  $a$  is the particle radius). A dip-in (Uzgiris type) electrode system with 4 ml polystyrene cuvettes was used.

**UV-vis Spectroscopy.** Absorption spectroscopy was carried out in Shimadzu 2401-PC UV-vis spectrophotometer. Standard poly(methyl methacrylate) cuvettes with a path length of 1 cm were used.

**Scanning Electron Microscopy.** Scanning electron microscopy (SEM) was carried out in JEOL 6500 field emission microscope equipped with in-lens thermal field emission electron gun. Secondary electron image (SEI) was taken at 15 kV electron beam with a

working distance of 10 mm. The samples were loaded on aluminum stubs, dried and sputter-coated with gold for 1 min.

**Fluorescence Microscopy.** Fluorescence microscopy was performed on a Leica DM2500 upright microscope equipped with 100 $\times$  oil immersion objective (NA 1.4). Excitation wavelength of 488 nm was chosen for fluorescein.

### **4.3. Results and discussions**

#### **4.3.1. Encapsulation of acid phosphatase**

The three-step synthesis protocol of enzyme-containing NACs is shown in Fig. 4.6. This immobilization route involves combining an aqueous solution of cationic polyamines with multivalent anions to yield spherical polymer-salt aggregates. Each of these aggregates can be considered to be a three-dimensional network of polymer molecules held together by the multivalent anions via salt bridging [31,32]. Combining the suspension of polymer-salt aggregates with an enzyme solution, leads to the formation of polymer-salt-enzyme aggregates which we hypothesize to be driven by a combination of favorable electrostatic interactions between the enzymes and the polymer, concentration gradient between the aggregate interior and external environments, hydrogen bonding, and hydrophobic interactions. Addition of negatively charged SiO<sub>2</sub> NPs leads to the formation of a protective shell wall to produce the enzyme-containing NACs.

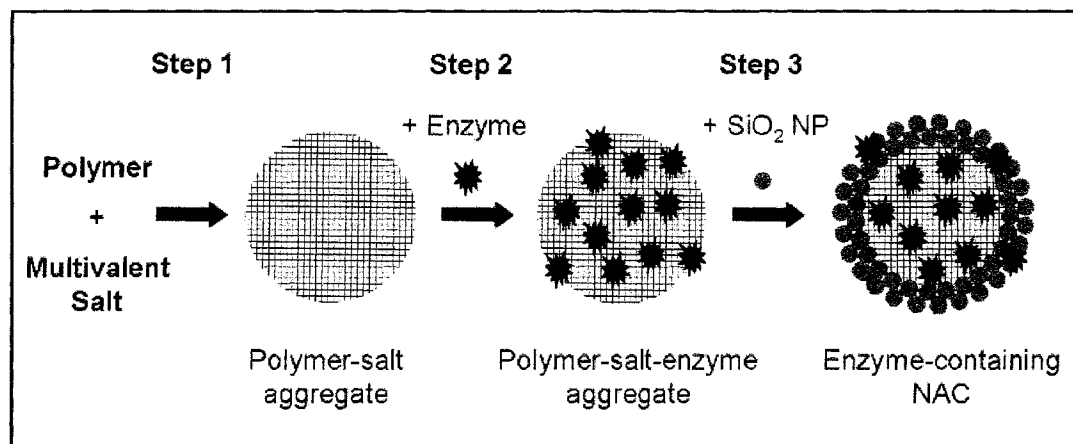


**Figure 4.6.** Conceptual diagram illustrating three-step encapsulation of enzyme in NACs.

In order to validate the proposed encapsulation technique for a real system, we chose acid phosphatase (AP) as our model enzyme. AP is ubiquitous in nature, perhaps one of the most concentrated sources being the human prostate gland, a fact exploited to measure the serum enzyme level as an index of prostate cancer [34]. AP enzyme serves to cleave off phosphate groups from a large variety of molecules and its structure is as shown in Fig. 4.7. The isoelectric point of AP obtained from potato is approximately 5.2 and the optimum working pH is 5.5 (for 4-NPP substrate) [35]. The approximate molecular weight is 55 KDa [34].

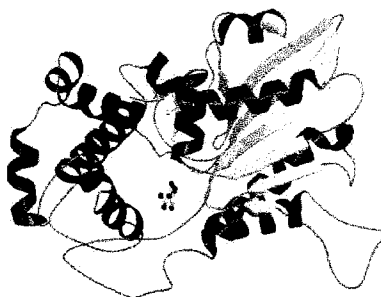


**Figure 4.7.** Three-dimensional structure of rat acid phosphatase [36,37].

Combining AP with PLL-cit aggregates resulted in PLL-cit-AP aggregates (Fig. 4.8a,b). Solid, micron-sized aggregates were seen to be in Brownian motion. In larger aggregates, a thin shell wall was observed through bright-field microscopy. Upon overlaying with the fluorescence image, it was apparent that PLL (conjugated to FITC) was concentrating around the edge of the aggregates. In Chapter 3, it was observed that addition of SiO<sub>2</sub> NPs to PLL-cit aggregates led to the higher concentration of PLL in the shell wall. This was theorized to occur due to disassembly of the PLL-cit aggregates upon the deposition of SiO<sub>2</sub> NPs. We apply similar analogy to the present case where PLL-cit aggregates come in contact with enzyme molecules leading to the concentration of PLL around the periphery, which then suggests that the AP enzyme might be behaving as a charged bio-nanoparticle.

The pH of PLL-cit-AP suspension was measured to be 6.8. This value being above the isoelectric point of the enzyme (pH 5.2) indicated that the enzyme possessed a net negative charge. Also, under these conditions, the electrophoretic mobility of PLL-cit aggregates (prior to introduction of AP enzyme) was measured to be +0.7 (μm/s)/(V/cm). Hence, favorable electrostatic interaction is hypothesized to be the driving force for the immobilization of AP enzyme in PLL-cit aggregates. From the images, though, it could not be determined whether the AP molecules were located in the interior of the PLL-cit-AP aggregates or electrostatically adsorbed to the aggregate surface. The PLL-cit-AP aggregates were unstable to drying and formed a film when taken out of suspension conditions, and so, further structural analysis was not possible.

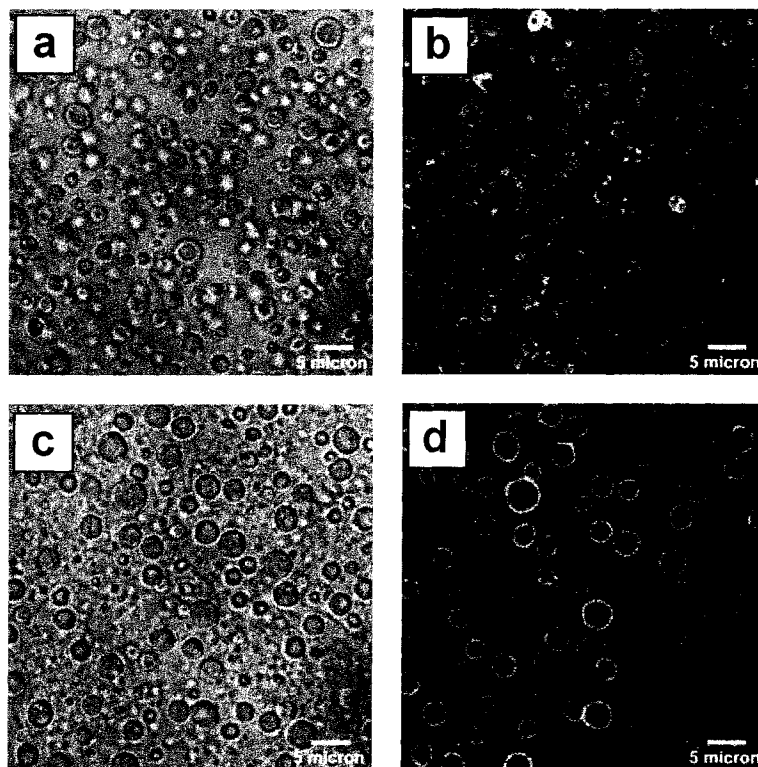


**Figure 4.8.** (a,c) Bright field and (b,d) confocal microscopy images of (a,b) PLL-cit-AP aggregates and (c,d) of AP-containing SiO<sub>2</sub> NACs. [PLL]<sub>final</sub> = 0.13 mg/ml; [cit]<sub>final</sub> = 2.1 mM; [SiO<sub>2</sub> NP]<sub>final</sub> = 7.9 wt.%; [AP]<sub>final</sub> = 0.26 mg/ml. PLL is tagged with FITC.

With the addition of SiO<sub>2</sub> NPs, we obtained phosphatase-containing NACs (Fig. 4.8c,d). Micron-sized spheres were seen under bright-field microscopy. Under fluorescence light, a distinct ring structure indicated that PLL was predominantly located in the NAC shell wall. Similar shell formation and hollowing effect of NACs, albeit without enzymes, has been observed before by Rana *et al.* in PLL-cit-SiO<sub>2</sub> NP NACs [31]. This was attributed to the de-aggregation or collapse of PLL-cit aggregates upon the shell wall formation. Hence, the enzyme was probably located mostly on the inner periphery of the shell wall or within the SiO<sub>2</sub> NP/PLL shell.

The effects of enzyme content on the loading, encapsulation efficiency, and final morphology of NACs were studied. Maximizing the loading of enzymes is useful in concentrating the enzyme to a small volume. Typical loadings obtained with conventional sol-gel techniques are in the range of 0.5 to 5 wt%. Recently, Stone and coworkers reported 20 wt% loading of enzyme in their substrate composed of biomimetic polymer and silica [30]. Table 1 lists data on enzyme loading and encapsulation efficiency as a function of the enzyme added to the PLL-cit aggregate suspension. High loading (16 wt%) and efficiency (70%) were achieved for small concentration of enzyme (0.019 mg/ml). When the enzyme concentration was increased, the loading remained almost constant (within experimental error range). However, a systematic decrease in the encapsulation efficiency was observed. This trend was not unexpected assuming that PLL-cit aggregate may become saturated with the enzyme after a certain weight loading. Therefore, any extra enzyme added would be present as free enzyme in suspension, reflecting a decrease in encapsulation efficiency. Surprisingly, at the highest concentration of enzyme used (0.26 mg/ml), the loading decreased significantly to 9 wt%. This was suspected to be due to the excess free enzyme interfering during the NP shell formation. Any loose surface-bound enzyme molecules would obstruct the deposition of NPs leading to the formation of relatively thinner shell wall. This can result in leakage of enzymes or even breaking of the microcapsules releasing the encapsulated enzymes during the assay process.

**Table 4.1.** Enzyme loading and encapsulation efficiency as a function of acid phosphatase concentration.

[Acid Phosphatase] <sub>final</sub> , mg/ml	Enzyme loading, wt%	Encapsulation efficiency, %
0.019	16	70
0.034	15	52
0.10	18	20
0.26	9	4

In order to observe the effect of enzyme concentration on the morphology of NACs, SEM images of dried phosphatase-containing SiO<sub>2</sub> NACs were taken (Fig. 4.9). In the absence of any enzyme, the SiO<sub>2</sub> NACs were stable to drying with almost no broken structures as shown in Fig. 4.9a. For low concentrations of enzyme, most of the capsules were stable (Fig. 4.9b,c). However, a few of them were found to be punctured or had dents in the shell wall. This puncturing or breaking of the NACs was predominant in samples where a high concentration of enzyme was added to the PAH-cit aggregates (Fig. 4.9d,e). Breakage of NACs may also have aggravated during the washing steps for the assay protocol. Hence, the SEM images confirm our suspicion that NACs become morphologically unstable in the presence of excess enzyme during leading to leakage of the enzyme.

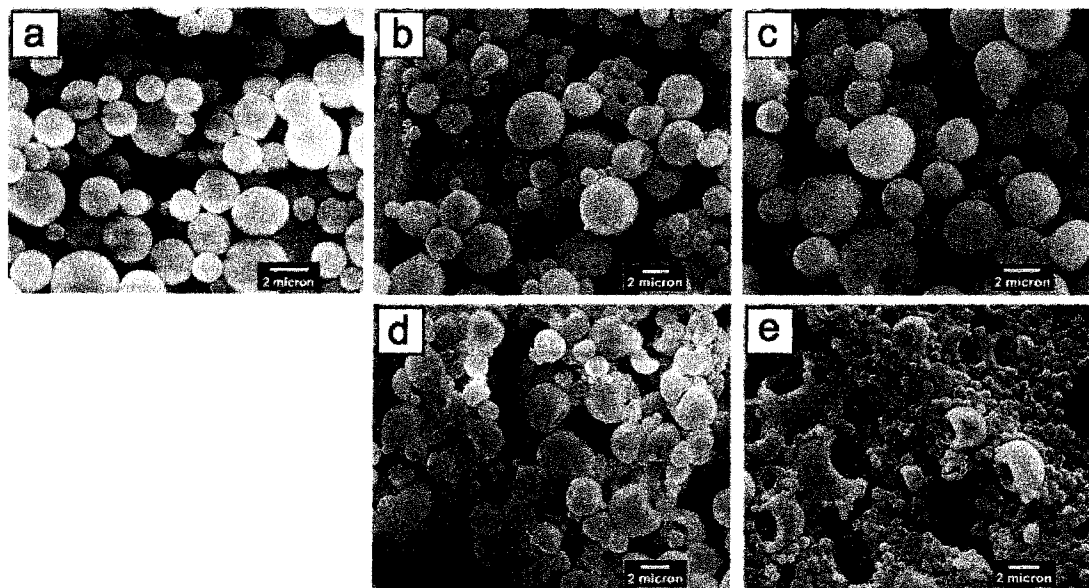


**Figure 4.9.** SEM images of AP-containing  $\text{SiO}_2$  NACs for different amounts of enzyme added to the PLL-cit aggregates. (a)  $[\text{AP}]_{\text{final}} = 0.0$  mg/ml, (b)  $[\text{AP}]_{\text{final}} = 0.019$  mg/ml, (c)  $[\text{AP}]_{\text{final}} = 0.034$  mg/ml, (d)  $[\text{AP}]_{\text{final}} = 0.10$  mg, and (e)  $[\text{AP}]_{\text{final}} = 0.26$  mg.

Another thing to be noted is that at higher concentration of enzymes, the size of the NACs was smaller (Fig. 4.9d,e). This may have resulted due to breakage of bigger NACs, which were structurally weaker than the smaller ones, thereby skewing the size distribution towards a smaller NACs population.

#### 4.3.2. Protein-containing NACs

From our previous observations under confocal microscope (Fig. 4.8d), we suggested that the AP enzyme may be located either on the inner periphery of the shell wall or mixed within the polymer/NP composite shell. In order to test this hypothesis indirectly, we carried out experiments with a protein molecule having similar size and charge as the AP enzyme. BSA was used as the model protein, which was covalently conjugated to a fluorescent dye, fluorescein isothiocyanate (FITC).



The BSA molecule is approximately 7 nm in diameter with an isoelectric point of 4.7 [38]. Combining BSA-FITC and PLL-cit aggregates led to the formation of PLL-cit-BSA aggregates. Bright-field images showed optically opaque spherical particles indicating high solid content in the PLL-cit-BSA aggregate (Fig. 4.10a). This was in contrast to PLL-cit-AP aggregates (Fig. 4.8a) where the aggregates were relatively transparent. Confocal image of PLL-cit-BSA aggregates (Fig. 4.10b) showed fluorescent particles. Fluorescence was observed both on the periphery as well as in the interior of the particles. From this, we could infer that the BSA molecules had not only adsorbed on the PLL-cit aggregates surface but also diffused inside the aggregates to form solid microspheres. However, the concentration of BSA was not homogenous throughout the particle. Fluorescence line intensity profile of a typical microsphere (inset in Fig. 4.10b) showed that the concentration of the BSA was the highest on the periphery, gradually decreasing towards the center.

The solution pH after addition of BSA-FITC was noted to be 8.1, at which the BSA molecule was negatively charged. The PLL-cit aggregate mobility was measured to be  $+0.7 \text{ (}\mu\text{m/s)/(V/cm)}$ . The favorable electrostatic interactions between the BSA molecules and the polymer aggregates aid in the formation of protein aggregates. On drying and subjecting to vacuum, the PLL-BSA microspheres retained their morphology as shown in Fig. 4.10c,d. They were found to be much more stable when compared to PLL-cit-AP aggregates after drying, possibly due to the higher solid content in the former.

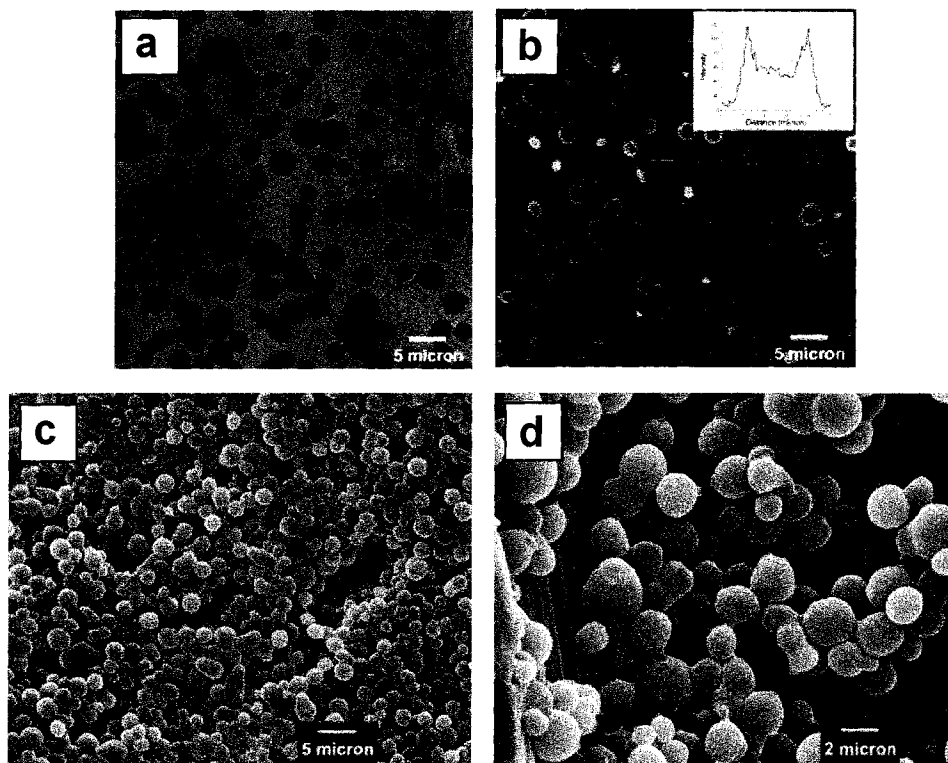


**Figure 4.10.** (a) Bright field, (b) confocal, and (c,d) scanning electron microscopy images of PLL-cit-BSA aggregates. Inset: Fluorescence intensity line profile of a BSA microsphere.  $[\text{PLL}]_{\text{final}} = 0.21 \text{ mg/ml}$ ;  $[\text{cit}]_{\text{final}} = 3.4 \text{ mM}$ ;  $[\text{BSA}]_{\text{final}} = 5.1 \text{ mg/ml}$ .

Upon the addition of  $\text{SiO}_2$  NP, we obtained BSA-containing  $\text{SiO}_2$  NACs (Fig. 4.11a,b). The morphology of these NACs seemed very similar to the PLL-cit-BSA aggregates. The NACs were very stable to drying and low pressure conditions, as shown in the SEM image (Fig. 4.11c,d). From fluorescence spectroscopy and thermogravimetric analysis (TGA), the BSA loading was measured to be 33 wt% and 28 wt% for PLL-cit-BSA aggregates and silica NACs, respectively. From the confocal and SEM images, the presence of  $\text{SiO}_2$  NP shell wall could not be distinguished, however.

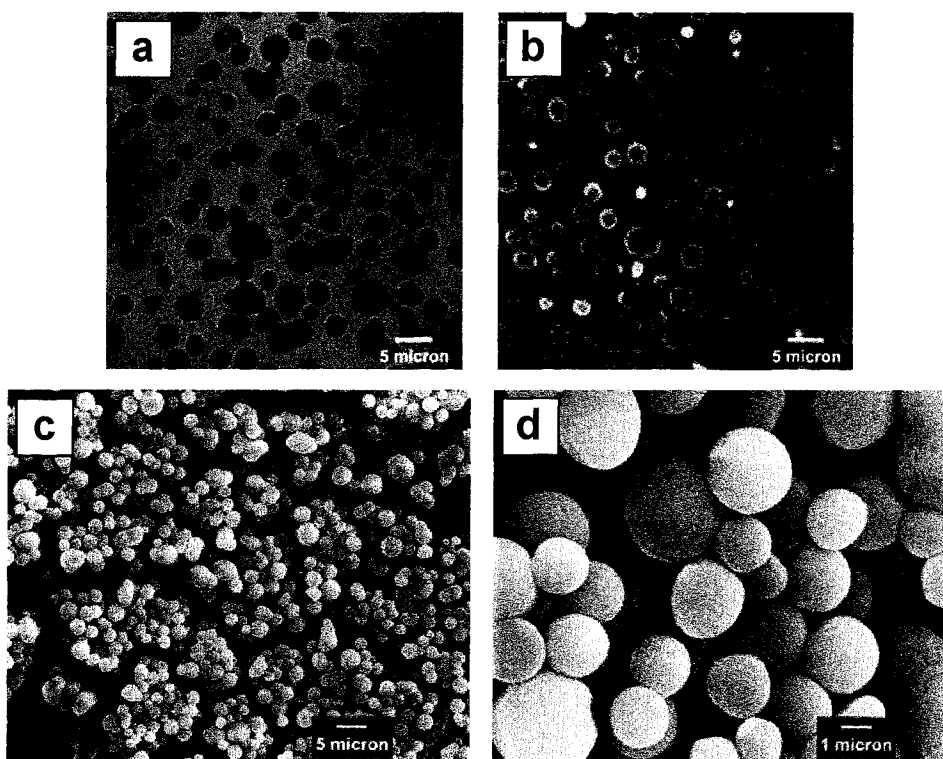


**Figure 4.11.** (a) Bright field, (b) confocal, and (c,d) scanning electron microscopy images of BSA-containing silica NACs.  $[PLL]_{\text{final}} = 0.13 \text{ mg/ml}$ ;  $[cit]_{\text{final}} = 2.1 \text{ mM}$ ;  $[BSA]_{\text{final}} = 3.1 \text{ mg/ml}$ ;  $[SiO_2 \text{ NP}]_{\text{final}} = 7.9 \text{ wt\%}$ .

The presence of the  $SiO_2$  shell was tested when we treated these two samples with a protease enzyme. Proteases are enzymes which break peptide bonds between amino acids in proteins. This process, called as proteolytic cleavage, is a common mechanism of denaturing proteins and enzymes. The PLL-BSA microspheres were incubated in a protease solution. After 15 hrs of aging, it was observed that the BSA microspheres had completely disintegrated leaving behind a homogenously fluorescent solution from the degradation of BSA (Fig. 4.12a,b). This was due to the protease attacking the shell formed by BSA and PLL and proceeding its way inward. On the other hand, when BSA-containing silica NACs were aged with protease for the same period of time, we could

see that the general morphology of the NACs was maintained. (Fig. 4.12c,d). Thus, the presence of a stable  $\text{SiO}_2$  NP shell wall acted as a protective sheath against the protease.

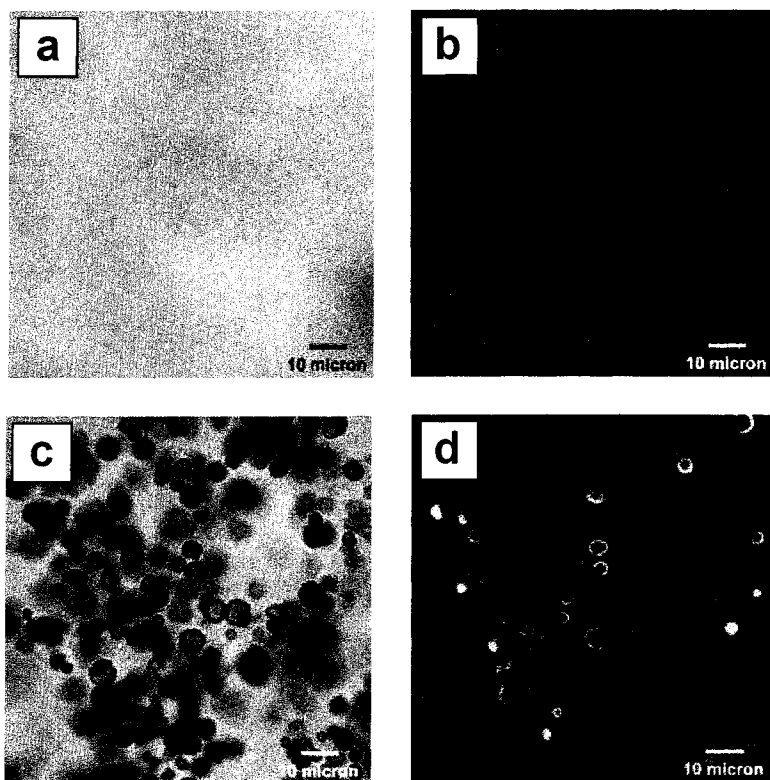


**Figure 4.12.** (a,c) Bright field and (b,d) confocal microscopy images of (a,b) disintegrated PLL-cit-BSA aggregates and (c,d) of BSA-containing  $\text{SiO}_2$  NACs incubated in protease enzyme for 15 hr time period at room temperature.

These BSA-FITC experiments indicate the likely localization of AP molecules in the NAC core interior in addition to a higher concentration of AP on the inner  $\text{SiO}_2$  walls, since both biomolecules are negatively charged. However, we do recognize that the surface charge distribution and the number of charges are different for both molecules.

### 4.3.3. Activity of encapsulated enzyme

The enzyme-containing NACs can be used as tiny reaction vessels (also see Appendix A) [31]. In order to demonstrate the activity of the encapsulated enzyme *in situ*, we carried out time-lapse fluorescence microscopy studies on phosphatase-containing NACs. A suspension of phosphatase-containing NACs was suspended in a solution of non-fluorescent substrate, FDP. A drop of this sample was placed on a glass slide and imaged under a fluorescence microscope.

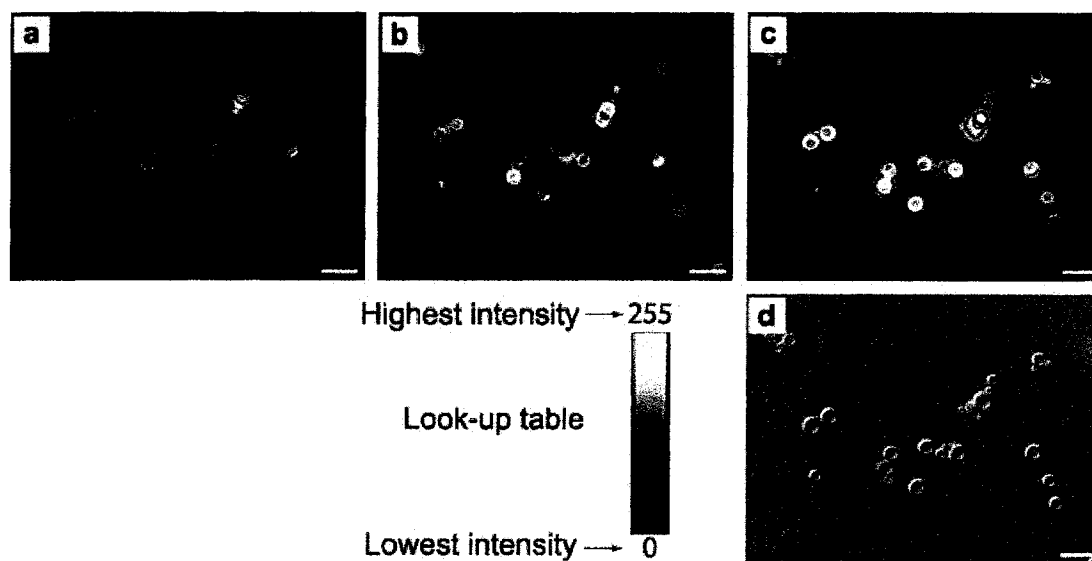


**Figure 4.13.** Series of time-lapse fluorescence microscopy images of phosphatase-containing  $\text{SiO}_2$  NACs suspended in an aqueous solution of FDP ((a) 3 min, (b) 15 min, and (c) 30 min). Non-fluorescent FDP diffuses inside the NACs, interacts with the enzyme, and fluorescent product (fluorescein) diffuses out. The images were pseudo-colored to visually enhance the concentration gradient. (d) DIC image of enzyme-containing NACs after 30 min of reaction time. Scale bars: 10  $\mu\text{m}$ .

The fluorescence emanating from the NACs was observed at different time points and was seen to be increasing with time (Fig. 4.13). The background fluorescence also emerged and grew in intensity with time. This was thought to be occurring due to the diffusion of FDP inside the NACs, and undergoing enzymatic cleavage producing

fluorescein, a highly fluorescent product. Image analysis clearly indicated that the generated fluorescein accumulated inside the shell wall and in the capsules' interior. Due to the concentration gradient, the product diffuses out into the background solution with time. Even after 1 hr of reaction, the NACs were observed to be stable. Hence, the microcapsules allow the confined enzymes to function in a protected environment, and allow the reactant and product molecules to transport across the permeable shell wall.

The possibility of AP adsorbing onto the external surface of NACs could not be discounted in spite of washing the NACs several times prior to testing its activity. In order to denature the surface-bound enzymes to test the activity of only the encapsulated enzymes, we carried out similar fluorescence time-lapse experiments in the presence of protease enzyme. No decrease in enzymatic activity was observed, which suggested that there was no externally bound enzymes. Unfortunately, we discovered through control experiments that AP was resistant to proteolytic attack. In fact, Abdul-Fadl *et al.* [39] reported this unusual resistance of AP back in 1949.

#### **4.3.4. Recoverability studies on encapsulated enzymes**

One of the advantages of immobilized enzyme systems is the ability to recover and re-use the enzyme after the desired reaction has been achieved. In order to show recoverability and reuse for our system, phosphatase-containing NACs were suspended in substrate solution and allowed to react with continuous stirring. The NACs were washed two times with water prior to this experiment, to remove any un-encapsulated enzyme. After 30 min, the reaction vial was centrifuged at 6000 rpm and two-thirds of the supernatant (containing product and reactant) was replaced with a fresh solution of 4-

NPP. This was repeated for three cycles (Fig. 4.14). The activity of the encapsulated enzyme was measured for each run by assaying the 10 ml withdrawn supernatant. A sample of enzyme-containing NACs similar to that shown in Fig. 4.8c was used for the experiment such that the total encapsulated enzyme content was measured to be 0.48 U (0.07 mg). Control experiments to compare the relative activities and recoverability were performed with the same quantity of free enzyme. The reason such an activity protocol was developed was to minimize any mass loss during decantation.

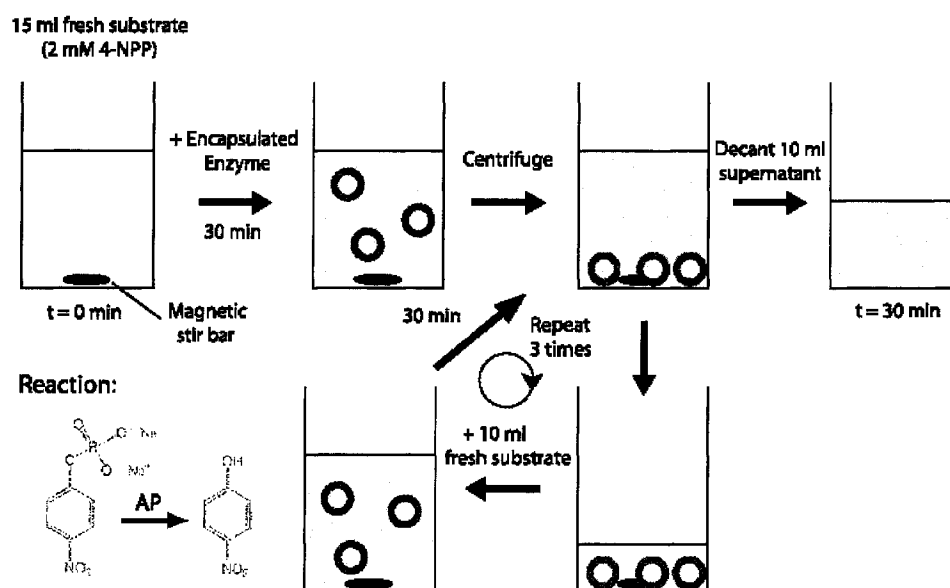


**Figure 4.14.** Schematic showing the step-by-step protocol for conducting recoverability studies of encapsulated enzyme.

Results for the relative activity and recoverability are shown in Fig. 4.15a-c. When the encapsulated enzyme (or the free enzyme) is suspended in the fresh substrate suspension (marked “0”), the 4-NPP gets converted into 4-nitrophenol (4-NP). Aliquot withdrawn after 30 min of reaction time is shown as a data point (marked “1”) at the end of the first cycle (Fig. 4.15a). Since two-thirds of the supernatant was withdrawn after

centrifugation to be replaced by fresh solution of 4-NPP, there was a step-decrease in overall concentration of 4-NP which is shown as the lower data point (marked “2”) at 30 min. As the reaction was continued, the concentration of 4-NP increased again in the second cycle (marked as “3”). Activities of free and encapsulated enzymes can be compared by measuring the slopes of the lines for each of the cycles in Fig. 4.15a,b. Through separate experiments, it was confirmed by taking data points at intermediate time points, that the product concentration increased linearly with time for the first 30 min, for the enzyme concentration used in this experiment. Hence only two data points for product concentrations at  $t = 0$  min and  $t = 30$  min were collected to determine the activities.

For the same amount of enzyme used, the slope (in the first cycle) for the free enzyme was found to be higher than that for the encapsulated enzyme. By comparing the slopes for the first cycle, the molecular activity of the encapsulated enzyme was measured to be 42% of that of the free enzyme. In the area of enzyme catalysis, rate of the reaction is defined in terms of molecular activity which is the number of molecules of substrate converted into product per minute per molecule of enzyme. This decrease in molecular activity of the encapsulated enzyme could have been due to diffusion limitations imposed by the shell wall which will impede the transport of substrate and/or product across the NAC shell.. Indeed, we found that PLL-cit-AP aggregates were as active as free enzyme. The PLL-cit-AP aggregates could be recovered for re-use after centrifugation since they formed a film at the vial bottom.



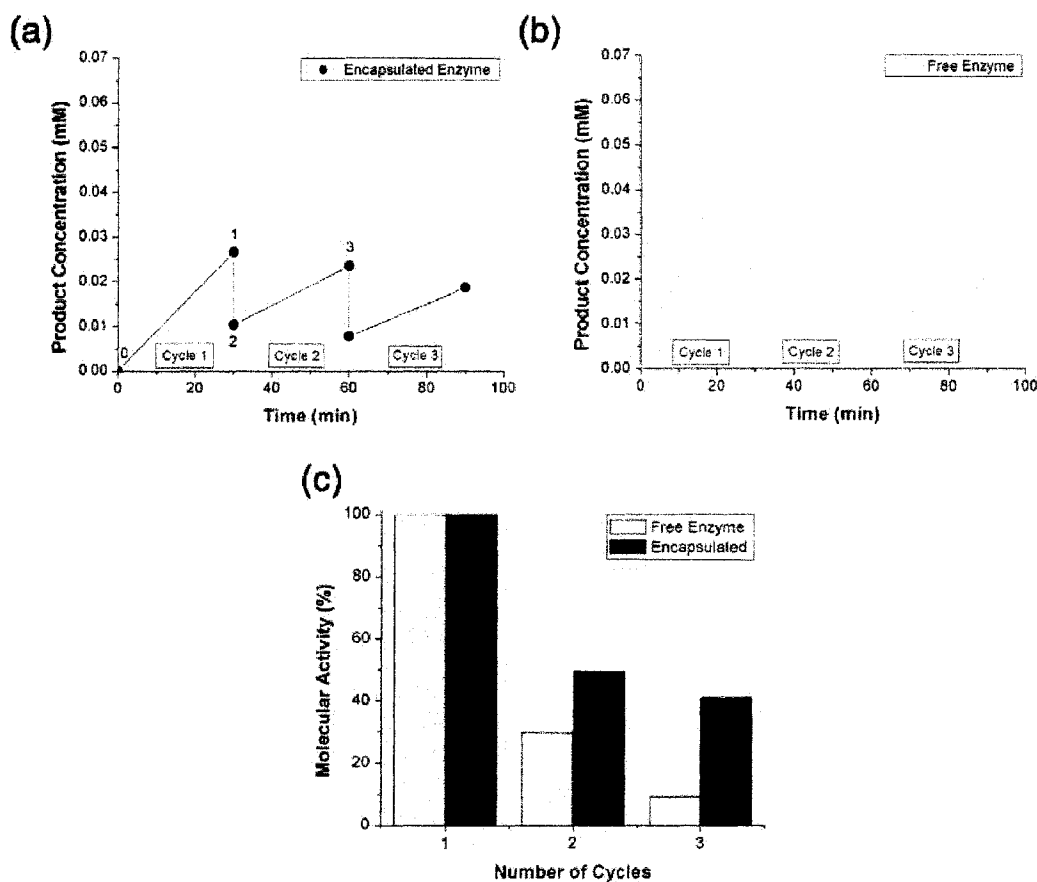


**Figure 4.15.** Graphs showing the increase in product concentration in the presence of (a) encapsulated enzyme and (b) free enzyme for three cycles. The solid lines are guide to the eyes. Bar graph in (c) shows a comparison of the normalized molecular activities of free and encapsulated enzymes.

Also, the possibility of enzyme denatured inside the shell formation was tested. In a separate experiment we disassembled the enzyme-containing NACs by adding saline solution (2 M NaCl), which released the enzyme. This suspension when combined with fresh substrate showed 92% of the molecular activity of the free enzyme. It was also confirmed separately that the enzymatic activity was not affected in the presence of 2 M NaCl (within experimental error range). Thus, the reduced molecular activity was likely not due to denatured enzymes.

The molecular activities of free and encapsulated enzymes for all three cycles were normalized to their respective molecular activities in the first cycle (Fig. 4.15c). It was seen that the activity of the free enzyme dropped more quickly than the encapsulated enzyme for subsequent cycles, due to the loss of ~66% of free enzyme after each cycle. At the end of the third cycle, only 10% of the initial enzyme amount was left. In contrast, we were able to recover 40% of the enzyme encapsulated in the NACs after three cycles indicating some level of recoverability. The loss of ~60% of encapsulated enzyme could have been due to rupturing of the NACs during multiple centrifugation cycles leading to leakage of the enzymes. Microscopy of the centrifuged AP-containing NACs indicated damaged particles. Work is under progress in order to make the shell walls thicker to prevent the breakage of NACs.

#### **4.4. Conclusions**

A facile route for encapsulating sensitive biomolecules such as enzymes in nanoparticle-assembled capsules (NACs) was demonstrated. Combining the enzyme solution with PLL-cit aggregate suspension, and subsequent addition of SiO<sub>2</sub> NPs led to the formation of stable enzyme-containing NACs. Enzyme loadings as high as 18 wt% were achieved under benign synthesis conditions, comparable to the highest enzyme encapsulation reported in literature. Through BSA-FITC encapsulation, the localization of acid phosphatase was suggested to be mostly near the shell wall and to a lesser extent, in the core. Through time-lapse fluorescence microscopy, it was established that the encapsulated enzyme could participate in chemical reactions. This also indicated permeability of shell wall. The observed reaction rate of encapsulated enzymes was less

than that of free enzyme for p-nitrophenyl phosphate dephosphorylation due to mass transport through the shell wall. The encapsulated enzyme could be recovered and re-used. 40% of the enzyme encapsulated in NACs was recovered, compared to 10% for free enzyme.

#### 4.5. References

- [1] Bickerstaff, G.F. *Immobilization of Enzymes and Cells*; Humana Press: New Jersey, **1997**.
- [2] Gemeiner, P. *Enzyme Engineering: Immobilized Biosystems*; Ellis Horwood: New York, **1992**.
- [3] Bornscheuer, U.T. Immobilizing enzymes: How to create more suitable biocatalysts *Angewandte Chemie: International Edition*, **2003**, 42, 3336.
- [4] Wiseman, A. *Handbook of Enzyme Biotechnology*; Ellis Horwood: New York, **1995**.
- [5] Uhlig, H., *Industrial Enzymes and Their Applications*, John Wiley, New York, **1998**.
- [6] Gill, I., Ballesteros, A. Bioencapsulation within synthetic polymers: sol-gel encapsulated biologicals *TIBTECH*, **2000**, 18, 282.
- [7] Taylor, R.F. *Protein Immobilization: Fundamentals and Applications*; Marcel Dekker: New York, **1991**.
- [8] Guilbault, G.G., *Analytical uses of immobilized enzymes*, Marcel Dekker, New York, **1984**.
- [9] Veliky, I.A., McLean, R.J.C. *Immobilized Biosystems: Theory and Practical Applications*; Chapman & Hall: New York, **1994**.

- [10] Avnir, D., Braun, S., Lev, O., Ottolenghi, M. Enzymes and other proteins trapped in sol-gel materials *Chemistry of Materials*, **1994**, *6*, 1605.
- [11] Kisler, J., M., Stevens, G.W., O'Connor, A.J. Adsorption of proteins on mesoporous molecular sieves *Materials Physics and Mechanics*, **2001**, *4*, 89.
- [12] Takahashi, H., Li, B., Sasaki, T., Miyazaki, C., Kajino, T., Inagaki, S. *Chemistry of Materials*, **2000**, *12*, 3301.
- [13] Fujii, T., Ogiwara, D., Ohkawa, K., Yamamoto, H. Alkaline phosphatase encapsulated in gellan-chitosan hybrid capsules *Macromolecular Bioscience*, **2005**, *5*, 394.
- [14] Olea, D., Faure, C. Quantitative study of the encapsulation of glucose oxidase into multilamellar vesicles and its effect on enzyme activity *Journal of Chemical Physics*, **2003**, *119*, 6111.
- [15] Bernheim-Grosswasser, A., Ugazio, S., Gauffre, F., Viratelle, O., Mahy, P., Roux, D. Spherulites: A new vesicular system with promising applications. An example: Enzyme microencapsulation *Journal of Chemical Physics*, **2000**, *112*, 3424.
- [16] Walde, P., Ichikawa, S. Enzyme inside lipid vesicles: Preparations, reactivity, and applications *Biomolecular Engineering*, **2001**, *18*, 143.
- [17] Caruso, F., Trau, D., Mohwald, H., Renneberg, R. Enzyme encapsulation in layer-by-layer engineered polymer multilayer capsules *Langmuir*, **2000**, *16*, 1485.
- [18] Blandino, A., Macias, M., Cantero, D. Calcium alginate gel as encapsulation matrix for coimmobilized enzyme systems *Applied Biochemistry and Biotechnology*, **2003**, *110*, 53.
- [19] Krajewska, B. Application of chitin- and chitin-based materials for enzyme immobilizations: A review *Enzyme and Microbial Technology*, **2004**, *35*, 126.
- [20] Buisson, P., Hernandez, C., Pierre, M., Pierre, A.C. Encapsulation of lipases in aerogels *Journal of Non-crystalline Solids*, **2001**, 285, 295.

- [21] Livage, J., Coradin, T., Roux, C. Encapsulation of biomolecules in silica gels *Journal of Physics: Condensed matter*, **2001**, *13*, R673.
- [22] Lloyd, C.R., Eyring, E.M. Protecting heme enzyme peroxidase activity from H<sub>2</sub>O<sub>2</sub> inactivation by sol-gel encapsulation *Langmuir*, **2000**, *16*, 9092.
- [23] Carturan, G., Campostrini, R., Dire, S., Scardi, V., de Alteris, E. *Journal of Molecular Catalysis*, **1989**, *57*, L13.
- [24] Ellerby, L.M., Nishida, C.R., Nishida, F., Yamanaka, S., Dunn, B., Valentine, J.I. *Science*, **1992**, *255*, 1113.
- [25] Braun, S., Rappoport, S., Zusman, R., Avnir, D., Ottolenghi, M. Biochemically active sol-gel glasses: the trapping of enzymes *Materials Letters*, **1990**, *10*, 1.
- [26] Bhatia, R., Brinker, C.J., Gupta, A.K., Singh, A.K. Aqueous sol-gel process for protein encapsulation *Chemistry of Materials*, **2000**, *12*, 2434.
- [27] Gill, I., Ballesteros, A. Encapsulation of biologicals within silicate, siloxane, and hybrid sol-gel polymers: An efficient and generic approach *Journal of the American Chemical Society*, **1998**, *120*, 8587.
- [28] Lei, C., Shin, Y., Liu, J., Ackerman, E.J. Entrapping enzyme in functionalized nanoporous support *Journal of the American Chemical Society*, **2002**, *124*, 11242.
- [29] Wang, Y., Caruso, F. Mesoporous silica spheres as supports for enzyme immobilization and encapsulation *Chemistry of Materials*, **2005**, *17*, 953.
- [30] Luckarift, H.A., Spain, J.C., Naik, R.R., Stone, M.O. Enzyme immobilization in biomimetic silica support *Nature Biotechnology*, **2004**, *22*, 211.
- [31] Rana, R.K., Murthy, V.S., Yu, J., Wong, M.S. Nanoparticle self-assembly of hierarchically ordered microcapsule structures *Advanced Materials*, **2005**, *17*, 1145.
- [32] Murthy, V.S., Rana, R.K., Wong, M.S. Nanoparticle-assembled capsule synthesis: Formation of colloidal polyamine-salt intermediates *Journal of Physical Chemistry B*, **2006**, submitted.

- [33] McComb, R.B., Bowers, G.N., Posen, S., *Alkaline Phosphatase*, Plenum Press, New York, **1979**.
- [34] Worthington Biochemical Corporation (<http://www.worthington-biochem.com>)
- [35] Van Hekken, D.L., Thompson, M.P., Strange, E.D. Immobilization of potato acid phosphatase on succinamidopropyl glass beads for the dephosphorylation of bovine whole casein *Journal of Dairy Science*, **1990**, 73, 2720.
- [36] Lindqvist, Y., Schneider, G., Vihko, P. Three-dimensional structure of rat acid phosphatase in complex with L(+) tartrate *Journal of Biological Chemistry*, **1993**, 268, 20744.
- [37] Schneider, G., Lindqvist, Y., Vihko, P. Three-dimensional structure of rat acid phosphatase *The EMBA Journal*, **1993**, 12, 2609.
- [38] Ge, S., Kojio, K., Takahara, A., Kajiyama, T. Bovine serum albumin adsorption onto immobilized organotrichlorosilane surface: influence of the phase separation on protein adsorption patterns *Journal of Biomaterials Science. Polymer Edition*, **1998**, 9, 131.
- [39] Abdul-Fadl, M.A.M., King, E.J. Purification of acid phosphatase by tryptic digestion *Biophysical Journal*, **1949**, 44, 434.

## **Chapter 5. “Patchy” particles formed from polyamine microphase separation**

### **5.1. Introduction**

The next generation materials and components used in molecular circuitry, optical applications, clinical diagnostics, sensors, and drug delivery devices will rely on building blocks self-assembling and forming higher order structures. As noted by Alivisatos [1], despite recent advancements in the synthesis techniques of a large variety of organic and inorganic materials, assembling them into ordered structures having functional capabilities remains the major bottle-neck. Within this context, “patchy” particles have garnered tremendous amount of attention, recently. They can be defined as particles with “sticky” surface patches having recognition units at prescribed locations. Such particles have been demonstrated to serve as much more efficient building blocks to create premeditated, higher-order complex architectures owing to their built-in recognition sites which can be “programmed” to direct the self-organization of particles [2]. Glotzer and coworkers, by means of computer simulations, have studied various types of generic structures that will be formed by patchy particles with attractive patches having various simple shapes such as lobes at the opposite poles of spherical particles, or bands around the equators, or even patches on triangular particles (Fig. 5.1 and 5.2) [3,4].

Structures thus formed can take the shape of sheets, rings, pyramids, chains, and three-dimensional clusters with various symmetries, and have potential applications in self-assembling electronic circuits, photonic crystals, solar panels, biological applications and clinical diagnosis utilizing selective molecular recognition, scaffolds for assembling

other compounds, as colloidal liquid crystals in display devices, electro-rheological fluids, and switching devices [5-8].

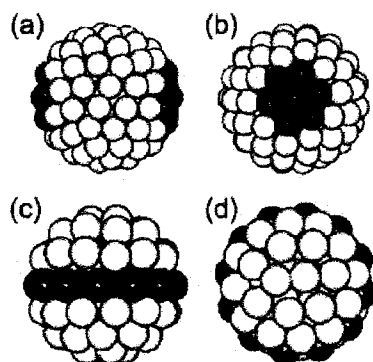


**Figure 5.1** Model patchy particles studied by Zhang and Glotzer [3]. (a) Side view of patchy sphere with two diametrically opposed circular patches. Red beads represent the course-grained “atoms” in the patches; yellow beads represent the rest of the particle, (b) axial view of the patchy sphere in (a), (c) side view of sphere with ring-like patch on the equator, and (d) axial view of sphere in (c).

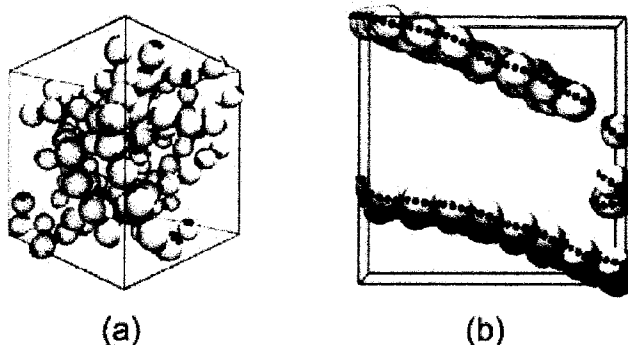


**Figure 5.2.** Equilibrium structures formed by particles in Fig. 5.1. (a) Long chains formed by patchy spheres in Fig. 5.1a and (b) Side view of sheets formed by spheres with ring-like equatorial patch as shown in Fig. 5.1b [3].

Colloidal particles (100 nm to 10 micron in diameter) usually have their surface uniformly covered with charged species which are ionically bound or any other molecular species covalently attached. Synthesis of particles with geometrically well-defined



patches at pre-determined spatial coordinates has been a formidable task for surface and colloid scientists. There are only a few techniques to fabricate patchy particles: These include the Langmuir-Blodgett (L-B) techniques, microcontact printing, evaporation (physical vapor deposition) of metals on colloid monolayer followed by chemisorption, using either gas-liquid, liquid-solid, or gas-solid interface to create particles with hemispheres of two different functionalities, and simultaneous electrohydrodynamic jetting.

In the L-B technique, a plate covered with a monolayer of colloids is initially dipped in a solvent (Fig. 5.3). The solvent hosts a floating monolayer of the coating polymer.

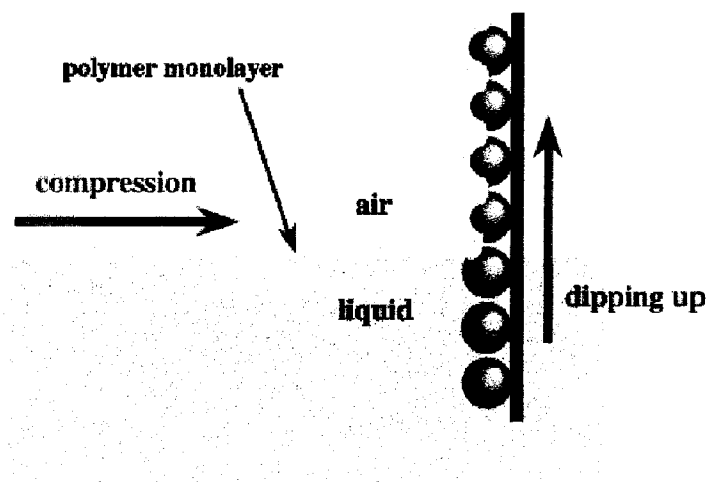


**Figure 5.3.** Schematic procedure of preparation of nonsymmetrical microspheres by the L-B technique. The copolymer monolayers were transferred onto the monolayer of microspheres to modify a restricted part of the microsphere surface [7].

The plate is slowly pulled upwards perpendicular to the monolayer of the coating polymer. The monolayer of coating polymer gets transferred onto a restrictive part of the monolayer of colloidal particles. Thus, the individual colloidal particles end up having patches of the polymer. Nakahama *et al.* demonstrated this by coating a monolayer of

amphiphilic terpolymer of octadecyl acrylamide, p-nitrophenyl acrylate, and 2,2,2-trifluoroethyl methacrylate on particles approximately 182 nm in diameter, initially deposited on a glass plate [7].

In the microcontact printing technique, films of specific chemicals deposited on PDMS stamps are printed onto monolayer of colloid particles deposited on a solid substrate. In one particular example, Cayre *et al.* prepared a monolayer of latex spheres on a glass substrate. Then, a monolayer film of water-insoluble surfactant with charge opposite to that of latex particles was deposited on a PDMS stamp. Lastly, the surfactant film is printed onto the colloid monolayer and then the colloids are redispersed in water [5]. In this way, the colloidal particles ended up having a bipolar surface charge distribution.

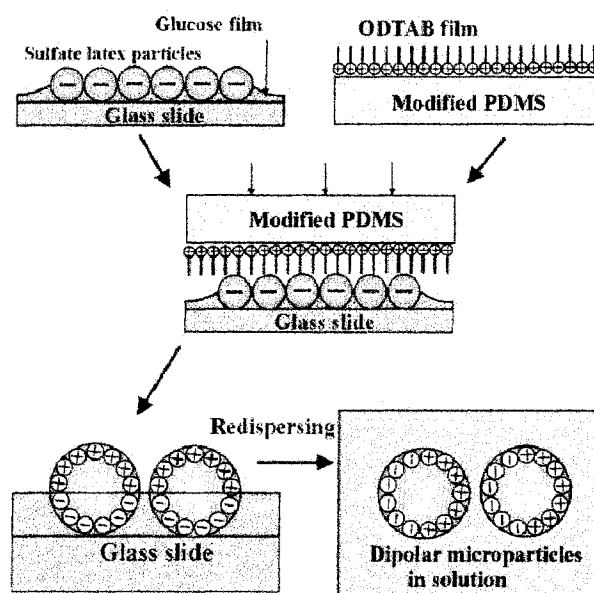


**Figure 5.4.** Scheme of the preparation of dipolar colloidal particles by microcontact printing of water-insoluble cationic surfactant on a monolayer of sulfate latex particles [5].

In the vapor deposition technique, the monodisperse colloidal particles are either spin coated [9] or drop-casted [10] on a solid substrate to form a monolayer (Fig. 5.5). Subsequent physical vapor deposition of metals (*e.g.*, gold, platinum, and palladium) coats only the top hemisphere of the particles [8,11].

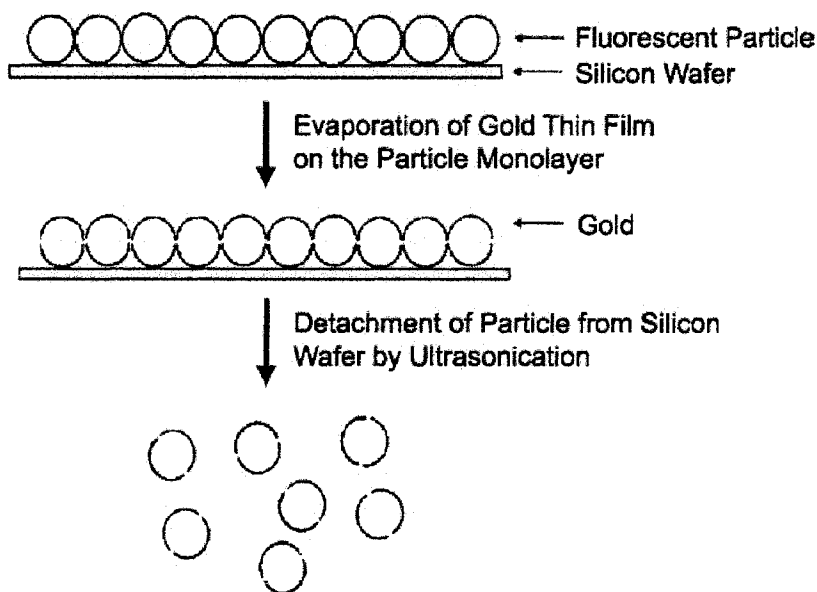


**Figure 5.5.** Schematic description of the fabrication process of the half-coated particle via vapor deposition of gold [9].

The interface between two media has also been used to introduce functional dissymmetry in uniform colloidal particles (Fig. 5.6) [12,13]. In a typical process, the colloidal particles are first assembled on the media interface (air-liquid or liquid-solid) to form a monolayer. The two hemispheres are exposed to the two different mediums owing to which the two sides will react differently. Functional groups to be impinged on either of the hemispheres of the colloid, is introduced through one of the two mediums.

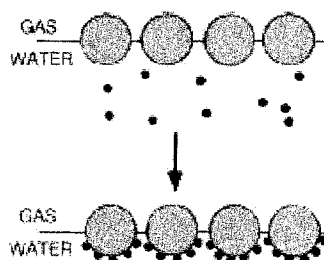


**Figure 5.6.** Schematic of the procedure to synthesize dissymmetric nanoparticles. In gray: silica nanoparticles; in black: gold nanoparticles [13].

In the technique of simultaneous electrohydrodynamic jetting, two distinct polymer solutions were pumped through a modified nozzle with a side-by-side geometry (Fig. 5.7). The ejecting liquids form a Taylor cone which was fragmented to give particles with two distinct hemispheres (also called as biphasic colloids) [14].

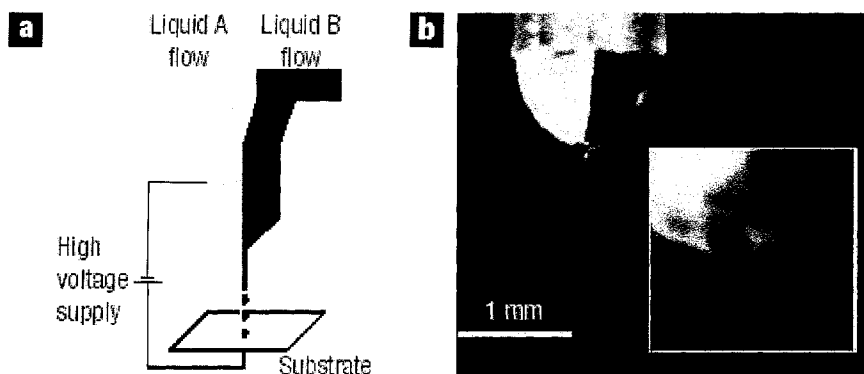


**Figure 5.7.** (a) A schematic diagram of the experimental setup used for electrohydrodynamic processing. When exposed to an applied electric potential (5–15 kV depending on the jetting conditions), the bipolar jetting liquid experiences an electrical field that is formed between the tip of the liquid and the counter-electrode (collecting substrate). For certain parameter combinations, well-structured biphasic Taylor cones were observed at the tip of the nozzle, consisting of two aligned fluid phases (b) A digital image of a typical biphasic Taylor cone with jet. Each phase was labeled by addition of 0.5% w/v of a fluorescent dye, that is, fluorescein isothiocyanate-conjugated dextran (green) and rhodamine-B-conjugated dextran (red). The inset shows a detailed image of the swirl-like jet ejection point [14].

Even though the previous preparation routes to patchy spheres appear flexible, they tend to be labor-intensive processes, requiring multiple steps to be performed in a sequential manner. While there are published methods to prepare spheres with a hydrophobic half and a hydrophilic half (“Janus” particles; named after the two-faced Roman god Janus) at an air-water interface, spheres with metallic sides through metal sputtering, and nanoparticles (NPs) with Angstrom-level ordering of surface-bound molecules [15], are relatively difficult to implement. In addition, none of these techniques allows one to confer more than two types of functionalities to the individual particles.

We recently reported a new technique to make hollow and polymer-filled microcapsules by charge-driven assembly of polyamines and NPs [16,17]. Polyamines (*e.g.*, poly(*L*-lysine)) when brought in contact with multivalent ions (*e.g.*, Na<sub>3</sub>cit) under aqueous conditions formed (sub)micron-sized spherical aggregates. These spherical aggregates were conceived to form via inter-polymer salt bridging by citrate anions. Addition of negatively charged NPs (*e.g.*, SiO<sub>2</sub> NPs) led to the formation of robust shell walls, thus yielding microcapsules (or nanoparticle-assembled capsules, “NACs”). Depending on the polyamine used, the NACs were either hollow or uniformly filled with the polymer.

In this work, we present for the first time a simple route to the fabrication of spherical particles in the micron (1–10 micron) and sub-micron (100 nm – 1 micron) regime with an anisotropic core and surface composed of discrete patches. We study the formation mechanism of these patchy particles and demonstrate control over their morphology. Finally, we show results for controlled localization of Au NPs within these patches which pave way for spatio-selective functionalization of patchy particles.

## 5.2. Experimental Section

### 5.2.1. Materials

Poly(*L*-lysine hydrobromide) (195,000 g/mol, ~935 lysine units per molecule, bromide counterion, “PLL”), poly(*L*-lysine hydrobromide) conjugated with fluorescein isothiocyanate (68,600 g/mol, ~330 lysine units per molecule, bromide counterion, “PLL-FITC”), poly(allylamine hydrochloride) (70,000 g/mol, ~750 allylamine units per molecule, chloride counterion, “PAH”), tetramethylorthosilicate (“TMOS”) were all procured from Sigma–Aldrich and were used without further purification. Trisodium citrate (“cit”) was obtained from Fisher Scientific. SiO<sub>2</sub> NPs (Snowtex-O, Nissan Chemicals) was available as aqueous colloidal suspension (20.5 wt.%, pH 3.4, ionic strength  $I = 16.9$  mM). The NPs measured  $13 \pm 3$  nm in diameter, according to dynamic light scattering. Zeta potential of SiO<sub>2</sub> NPs in the original sol condition was calculated from its electrophoretic mobility ( $-1.4$  (μm/sec)/V/cm)) to be  $-16$  mV in the Henry’s limit. The fluorescent dyes of fluorescein isothiocyanate (FITC) and rhodamine B isothiocyanate (RITC) were procured from Sigma-Aldrich. Polyelectrolyte stock solution and all subsequent diluted precursor solutions were made using deionized water (18.2 MΩ, Barnstead Nanopure Diamond System).

### 5.2.2. Synthesis

Aqueous mixtures of PLL and PAH were prepared by mixing different volume ratios of PLL solution (4.5 mg/ml) and PAH solution (2 mg/ml). In order to prepare 75% PLL and 25% PAH mixture, 37.5 μl of PLL solution was mixed with 12.5 μl of PAH solution. The concentrations of precursor polymer solutions were chosen such that a 75/25 mixture

indicated 75% of positive charges in solution were coming from PLL and the rest 25% from PAH. All experiments with polyelectrolyte-salt solutions were done at specific charge ratio  $R$ , which is defined as the ratio of total negative charge of the added salt to the total positive charge of the polymers ( $R = [\text{anion}] \times |z_-| / [\text{polymer}] \times |z_+|$ , where  $z_-$  is negative charge per anion and  $z_+$  is positive charge per chain). For all experiments,  $R$  value was arbitrarily chosen at 4 using 12.0 mM cit salt solution. A typical synthesis protocol consisted of mixing different volume ratios of PLL (precursor concentration of 4.5 mg/ml) and PAH (precursor concentration of 2 mg/ml) to give a final volume of 50  $\mu\text{l}$ . To this, 125  $\mu\text{l}$  of cit salt solution was added (12 mM,  $R = 4.2$ ) and gently mixed for 10 sec using a vortex mixer at “5” speed (on a scale from 1–10). The resulting suspension was aged for 30 min under quiescent conditions. After the aging period, the suspension was mixed with 50  $\mu\text{l}$  of 1M tetramethylorthosilicate (TMOS) and gently homogenized resulting in solid microspheres. After further aging for 20 min, the suspension was centrifuged and thoroughly washed with deionised water. In order to synthesize hollow microcapsules, TMOS was replaced with 125  $\mu\text{l}$  of colloidal suspension of  $\text{SiO}_2$  NP. Conjugation of PAH with FITC and RITC was carried out as explained in Chapter 3.

### 5.2.3. Characterization

**Confocal Laser Scanning Microscopy.** Confocal images were captured with Carl Zeiss LSM 510 inverted microscope equipped with a 100 $\times$  oil immersion objective (NA = 1.4). The laser excitation wavelength of 488 nm was chosen for FITC ( $\lambda_{\text{ex}} = 494.5$  nm,  $\lambda_{\text{em}} = 519$  nm) and 543 nm for RITC ( $\lambda_{\text{ex}} = 560$  nm,  $\lambda_{\text{em}} = 580$  nm). Samples were

mounted on conventional glass slides and sealed under a cover slip to prevent drying. All samples were freshly prepared 1–2 hrs prior to imaging.

**Zeta Potential Analysis.** Zeta potentials were calculated using phase analysis light scattering (PALS), a variation of electrophoretic dynamic light scattering (DLS), from electrophoretic mobility measurements using Henry's equation (i.e.,  $0.1 \leq \kappa a \leq 100$ , where  $\kappa$  is the Debye–Hückel parameter and  $a$  is the particle radius). A dip-in (Uzgiris type) electrode system with 4 ml polystyrene cuvettes was used.

**Scanning Electron Microscopy.** Scanning electron microscopy (SEM) was carried out in JEOL 6500 field emission microscope equipped with in-lens thermal field emission electron gun. Secondary electron image (SEI) was taken at 15 kV electron beam with a working distance of 10 mm. The microsphere suspension was washed twice with water, loaded on the aluminum stub, and dried before imaging. The sample was sputter-coated with gold for 1 min.

**Optical Microscopy.** Optical microscopy was performed on a Leica DM2500 upright microscope equipped with 100 $\times$  oil immersion objective (NA 1.4).

### 5.3. Results and discussions

Fig. 5.8a shows a fluorescence overlay image of a homogenous, clear mixture of PLL and PAH in aqueous medium (50/50 mixture, PLL/PAH ratio based on the number of monomers of each polymer). Upon the addition of multivalent citrate salt to this mixture, the solution turned turbid immediately. After aging for 30 min, when a drop of this turbid suspension was observed under the microscope, spherical polymer aggregates were seen. However, it was very intriguing to observe that each of these aggregates was composed



of distinct red (PAH) domains distributed within larger green (PLL) aggregates (Fig. 5.8b). PLL and PAH, while homogeneous in aqueous solution, apparently phase segregated into discrete domains after contact with the citrate salt. Smaller aggregates had a core-shell structure and larger aggregates contained multiple PAH cores. In order to check if this microphase segregation of polyamines within the aggregates was an artifact of polymer dye conjugation, we performed control experiments with non-conjugated PLL and PAH and observed very similar results (Fig. 5.8c).

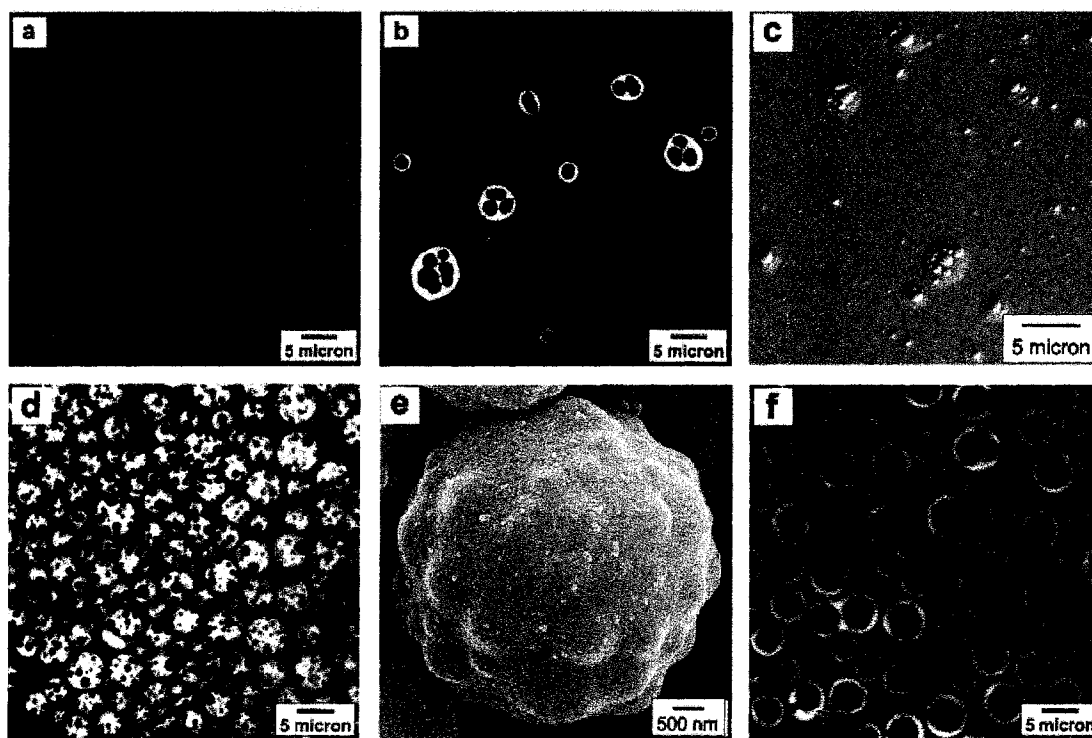


**Figure 5.8.** (a) Confocal image of homogenous 50/50 aqueous mixture of PLL/PAH, (b) confocal image of microphase-separated PLL/PAH-cit aggregates, (c) DIC image of microphase-separated PLL/PAH-cit aggregates (50/50) with non-conjugated PLL and PAH, (d) confocal image of microspheres after addition of silicic acid to (b), (e) SEM image of a microsphere from addition of silicic acid to (b), and (f) confocal image of anisotropic NACs from addition of 13 nm SiO<sub>2</sub> NP to (b).

From our past experiments, it is well known that PLL-cit and PAH-cit tend to spread on contact with glass coverslip [17]. This was observed for the case of PLL/PAH

composite aggregates, as well (Fig. 5.8c). In spite of this spreading, the general observation of microphase separation of PLL and PAH remains indisputable. At this point, we will not assume the observed internal structure of the glass-adsorbed PLL/PAH-cit aggregates is the same as that of freely suspended aggregates.

In our previous work, silicic acid was used to create solid microspheres when used in combination with the polymer-salt aggregate suspension [16]. When the microphase separated PLL/PAH mixture was brought in contact with silicic acid, we obtained microspheres wherein PAH domains were distributed in the PLL-cit aggregate (Fig. 5.8d). The size and number of PAH domains varied across the microspheres. Apparently, the addition of silicic acid preserved the general shape and size of the aggregates seen in Fig. 5.8b. Through closer analysis under SEM, it was observed that the microspheres had protuberances or “patches” on the surface (Fig. 5.8e). The size of these patches varied from 200 nm to 700 nm which correlated well to the size of the PAH domains seen in Fig. 5.8d. Hence, these patches appear to be the PAH domains partially sticking out of the microsphere surface.

Interestingly, when the silicic acid was replaced with SiO<sub>2</sub> NPs, the resulting particles were found to have a completely different morphology. A distinct layer of PLL was seen to form the shell wall (Fig. 5.8f). The PAH domains, in this case, may coalesce with each other and adhere to the inner periphery of the shell lending an anisotropic-shaped core to the NACs.

### 5.3.1. Effect of charge ratio $R$ on aggregate structure

Charge ratio,  $R$ , was used as one of the parameters in our previous work [16,17] for controlling the polymer-salt aggregate size. Experiments were performed to study the effect of  $R$  on the morphology of PLL/PAH-cit composite aggregates (with 50/50 mixture composition). A wide range of  $R$  values was tried (2-100) and it was observed that in all cases the aggregate morphology were very similar. Hence, we did not continue further research on this aspect. In this work, all experiments were performed at an  $R$  value of 4.

### 5.3.2. Effect of PLL/PAH ratio on aggregate internal structure

We studied the effect of PLL/PAH ratio on the internal structure of the composite aggregates. Fig. 5.9 shows the systematic evolution of the internal structure when PLL/PAH ratio was varied from 100/0 to 0/100. For all PLL/PAH ratios between 100/0 to 0/100, the PAH domains always remained inside the PLL aggregates and no PAH was found as discrete PAH-cit aggregates. With a large amount of PLL in the mixture (90/10), small speckles of PAH were distributed in a “continuous” medium of PLL (Fig. 5.9b). On increasing the PAH concentration, the domain size progressively increased. After a certain PAH concentration (>50% PAH), the domains occupied the whole core without any PLL (Fig. 5.9e,f). With the decrease of PLL concentration, the PLL outer layer thickness was seen to decrease as well. Curiously, after attaining the core-shell structure for high PAH concentrations, isolated speckles of PLL were seen within the PAH core.

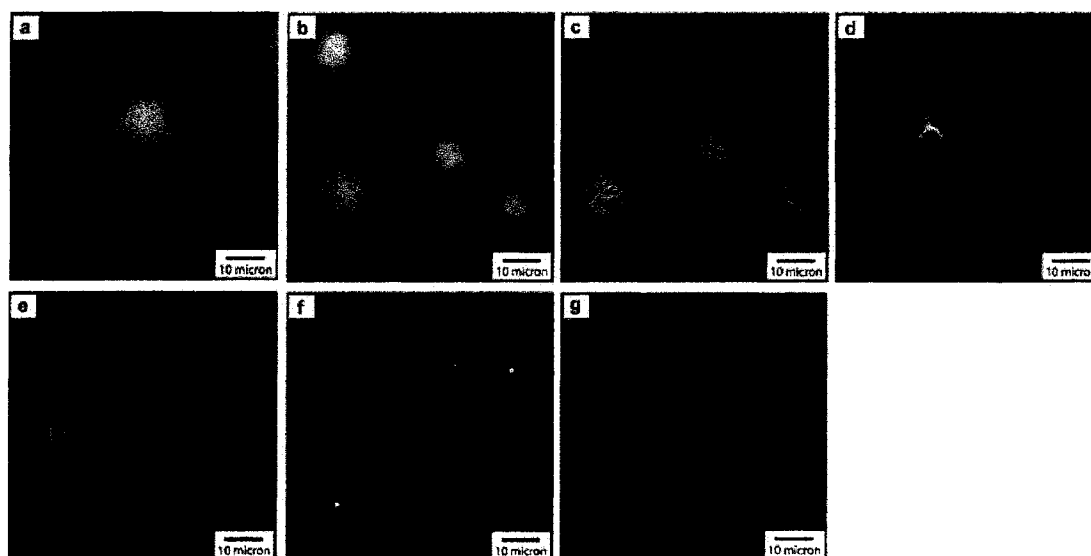


**Figure 5.9.** Confocal microscopy images of PLL/PAH-cit aggregates with varying relative amounts of PLL/PAH. (a) 100/0, (b) 90/10, (c) 75/25, (d) 50/50, (e) 25/75, (f) 10/90, and (g) 0/100. Aggregates were aged for 30 min under suspension conditions before imaging.

In order to understand the PLL/PAH-cit aggregate system, we can draw analogy with the extensive work done in the area of polymer blends. Our PLL/PAH-cit aggregates bear certain similarities to a HDPE/PS/PMMA polymer blend system (HDPE: high density polyethylene; PS: polystyrene; PMMA: polymethylmethacrylate) studied by Reignier and Favis [18]. In their work, PMMA domains were suspended in dispersions of PS in a continuous medium of HDPE. For a high content of PS, the morphology formed by PS/PMMA components constituted of distinct particles of PMMA distributed in the larger domains of PS. PS/PMMA ratio was used to control the inner structure of the composite droplets. The PMMA domain size increased with increasing PMMA content. When PMMA content was high enough ( $>60$  vol%), a PMMA core-PS shell morphology was obtained. Upon increasing the PMMA content further, the shell was observed to decrease in thickness. Further increasing the PMMA content led to the appearance of PS

particles in the PMMA phase akin to speckles of PLL in PAH core (Fig. 5.9e,f). For all compositions of PS/PMMA, the PMMA domains always remained inside the PS phase. This trend was also reported by Luzinov *et al.* for PS/SBR/PE ternary polymer blend (PS: polystyrene; SBR: styrene-butadiene rubber; PE: polyethylene). Further, Reignier and Favis, found that the formation of composite droplets takes places very rapidly ( $< 1$  min). Once formed, the internal structure of the composite did not change with time. The composite aggregates were observed to grow with time and was explained to take place via dual coalescence mechanism, first between PMMA domains within the droplets, and second between composite droplets themselves.

Our system differs from the polymer blends in several ways. First, the phase separation between the polyamines was triggered by multivalent ions, whereas in the case of polymer blends it takes place spontaneously without the need for external trigger. Another difference is that water exists not only as the continuous phase for our system, but also within the PLL-cit and PAH-cit domains [17]. Also, in contrast to their observations on the constant internal structure of the aggregates with time, we found that the PLL/PAH-cit domains undergo a definite change in their internal structure at short time scales as explained in the next section.

### 5.3.3. Effect of aggregate aging time

In order to track the morphology of composite aggregates with time, aliquots from a freshly prepared PLL/PAH-cit suspension (50/50 mixture) were withdrawn at different times and imaged under confocal microscopy. At five seconds, immediately after mixing in the salt solution with PAH/PLL mixture (50/50), most of the aggregates had assumed a

core-shell structure as shown in Fig. 5.10a. There were, however, a few exceptions of larger aggregates containing multiple PAH domains. After aging for  $t = 5$  min, a significant increase in aggregates composed of multiple PAH domains was noted (Fig. 5.10b). In addition, the average size of composite aggregates had increased. Upon further aging for 30 min, most of the composite aggregates were composed of multiple PAH domains and had grown bigger in size (Fig. 5.10c). After aging the PLL/PAH-cit aggregate suspension for  $>1$  hr, a macroscopic film was observed at the bottom of the reaction tube.

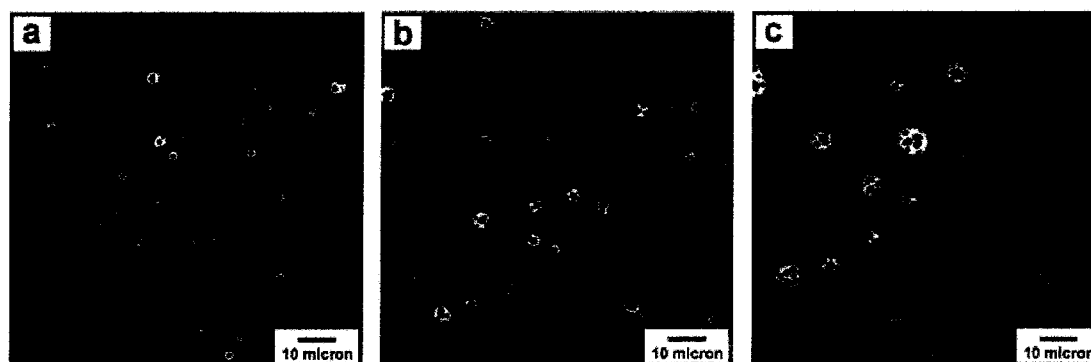


**Figure 5.10.** Confocal microscopy images of representative PLL/PAH-cit aggregates (50/50 mixture). Aliquots were withdrawn from the aggregates suspension at different times: (a) 5 sec, (b) 5 min, and (c) 30 min.

#### **5.3.4. Formation and growth mechanism of microphase-segregated polyamine aggregates**

We hypothesized the formation of microphase-separated polyamine aggregates to be a two-step process (Fig. 5.11). These steps consist of: (1) formation of separate PLL-cit and PAH-cit nuclei aggregates and (2) coalescence of aggregates leading to composite PLL/PAH-cit aggregate formation. In this section, we will discuss these two points at length.

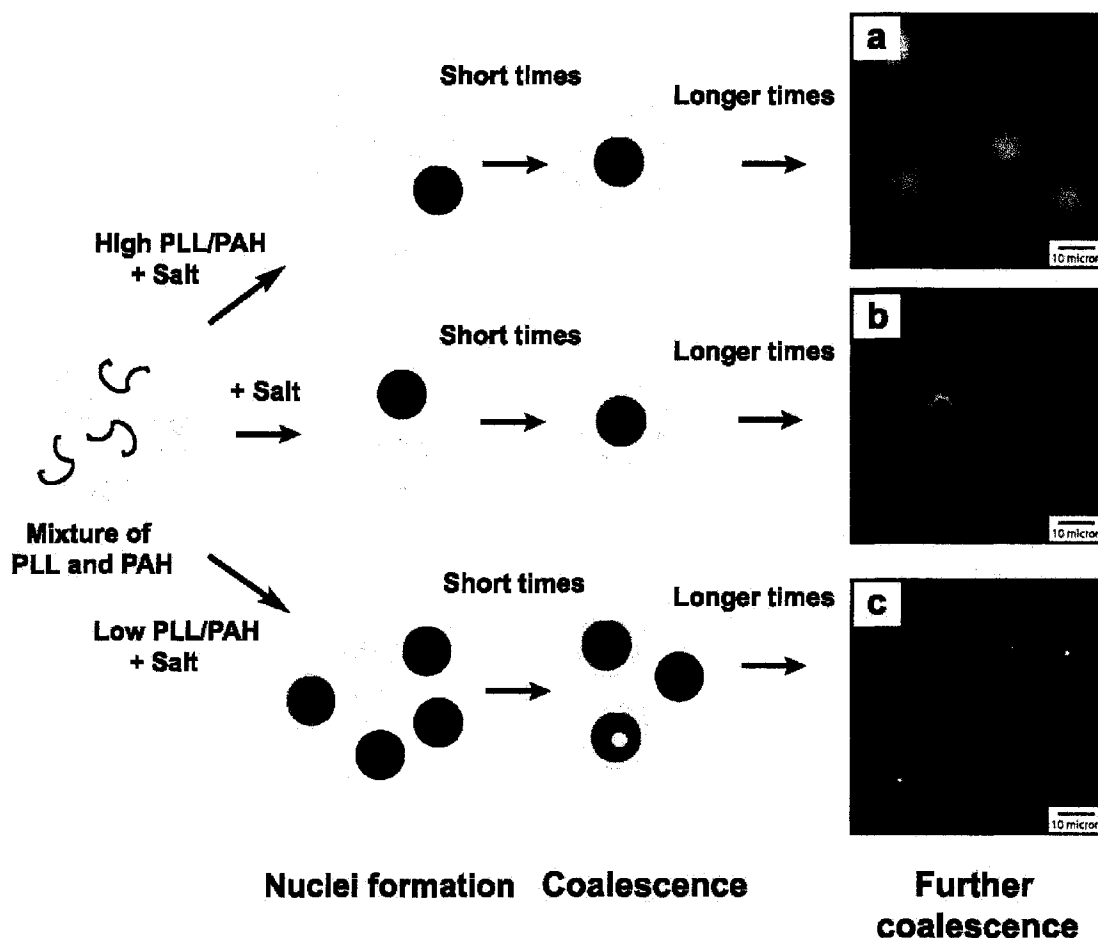


**Figure 5.11.** Schematic for the proposed formation mechanism of microphase-segregated polyamine aggregates. Confocal microscopy images of PLL/PAH-cit aggregates with varying relative amounts of PLL/PAH. (a) 90/10, (b) 50/50, and (c) 10/90. Aggregates were aged for 30 min under suspension conditions before imaging.

Addition of cit salt to the PLL/PAH mixture was hypothesized to lead to the formation of separate nuclei aggregates. Multivalent ion-induced nucleus formation in polyamines has been discussed at length in Chapter 3 and in other references [16,17]. Briefly, the multivalent anions act as ionic bridges which electrostatically crosslink the polyamines through their protonated amine groups forming spherical aggregates composed of polymer-salt network. The nucleation process is spontaneous and occurs on

the time scale of less than a second. Since this process is extremely rapid, we were not able to image the formation of distinct PLL and PAH nuclei particles.

After the initial nuclei particles have been formed for both PLL and PAH, the PLL-cit and PAH-cit aggregates could grow *via* droplet-droplet coalescence. To prove this, we prepared aggregate suspensions of PLL-cit and PAH-cit (Fig. 5.12a,b). After separately aging them for 10 min, the suspensions were mixed together and gently homogenized using a pipette. A small aliquot was withdrawn immediately (in less than five seconds after mixing) for imaging. Three types of structures were seen: (1) discrete PAH-cit aggregates, (2) individual PLL-cit aggregates, and (3) core-shell structures wherein a distinct layer of PLL was seen to envelope PAH aggregates (Fig. 5.12c). Upon further aging (for 10 min), more of the composite aggregates (containing multiple PAH domains) were observed and the number of individual PAH-cit aggregates had depleted considerably. The composite aggregates containing multiple PAH domains resembled PLL/PAH-cit aggregates and are shown in Fig. 5.9d and Fig. 5.10c.

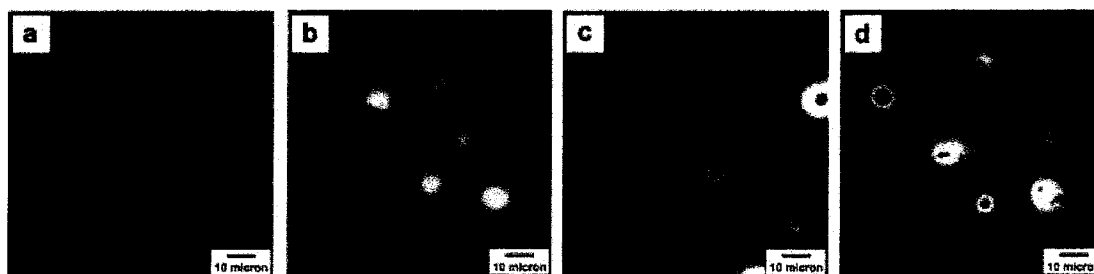


**Figure 5.12.** Confocal images of (a) PAH-cit aggregates aged for 10 min, (b) PLL-cit aggregates aged for 10 min, (c) composite aggregates formed by mixing (a) and (b) and aging for 5 sec, (d) composite aggregates obtained after aging (c) for 10 min. PLL/PAH ratio was set at 50/50.

Since different PLL/PAH ratios produced composite aggregates with different internal structures, we proposed that the formation of the composite aggregates at low



and high PLL/PAH ratios was consistent with the coalescence process. To verify this, experiments were performed to study the growth mechanism of PLL/PAH-cit aggregates for the cases of 75/25 and 25/75 mixtures. Two types of suspensions were made for both types of mixtures: PLL/PAH-FITC-cit and PLL/PAH-Rhod-cit. PLL used for this experiment was not conjugated to a fluorescent dye. The suspensions were mixed and aliquots were withdrawn at 5 sec and 10 min for imaging purpose.

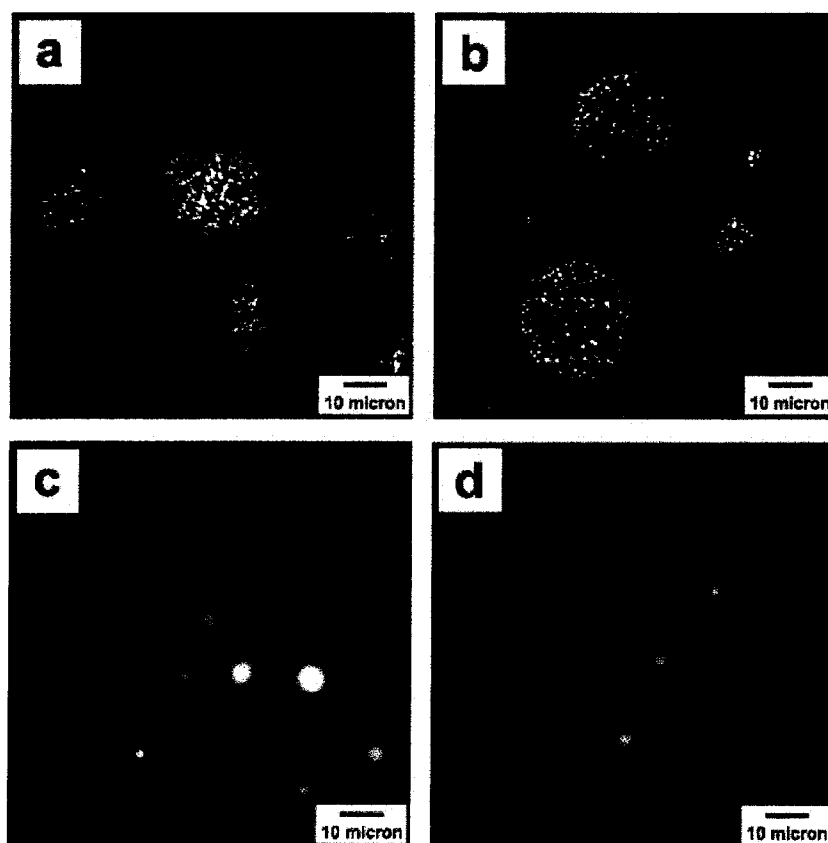


**Figure 5.13.** Confocal microscopy images of suspensions obtained after mixing PLL/PAH-FITC-cit and PLL/PAH-Rhod-cit aggregates for 75/25 mixture (aged for (a) 5 sec and (b) 10 min) and 25/75 mixture (aged for (c) 5 sec and (d) 10 min). The PLL/PAH-FITC-cit and PLL/PAH-Rhod-cit aggregates were aged for 10 min prior to mixing.

In the 75/25 mixture case (PLL in excess), after 5 sec aging, the composite aggregates seemed to have undergone coalescence through merging of PLL/PAH-FITC-cit and PLL/PAH-Rhod-cit aggregates. Inside these coalesced aggregates, discrete red and green PAH-cit domains were distributed (Fig. 5.13a). PAH domains containing mixed colors could not be identified which indicated that there was no mixing between the PAH-cit domains. After 10 min aging the PLL/PAH-cit aggregates grew, but the coalescence of PAH-cit domains still did not take place (Fig. 5.13b).

Contrasting results were obtained for mixtures with higher PAH content (25/75 mixture). After aging for only 5 sec, the resulting aggregates appeared to form from the coalescence of the overall PLL/PAH-FITC-cit and PLL/PAH-Rhod-cit aggregates and the coalescence of PAH-FITC-cit domains with PAH-Rhod-cit domains (Fig. 5.13c). We also observed a few smaller aggregates which were pure red and pure green which may result when those aggregates did not undergo coalescence or less likely, underwent coalescence with similar-colored aggregate. Upon aging for 10 min, more of the mixed color aggregates were seen, indicating that the system was going towards a homogenous composition (Fig. 5.13d). Hence, in mixtures composed of larger amount of PAH, not only do the composite PLL/PAH-cit aggregates grow with time, but also the PAH-cit domains within them show coalescence. This dual coalescence mechanism was consistent with the observation of Reignier and Favis [18] for the polymer blend system.

In order to better understand the apparent engulfing of PLL-cit over PAH-cit aggregates, we need to consider the interfacial tensions between the PLL-cit/water, PLL-cit/PAH-cit, and PAH-cit/water phases. Starting from the first principles, we consider a drop of liquid (L) on a solid substrate (S) (Fig. 5.14). Three interfacial tensions come into

play in this system:  $\gamma_{SV}$ ,  $\gamma_{SL}$ , and  $\gamma_{LV}$ . If the drop wets the solid, two interfaces will form: liquid-vapor and solid-liquid. On the other hand, if the drop were to bead up, only the solid-vapor interface extends macroscopically. Considering that the system will always tend to minimum surface energy, if the sum of the two interfacial tensions (liquid-vapor and solid-liquid) is smaller than the solid-vapor interfacial tension, then the drop will spread to form a film. Otherwise, it will form a bead.

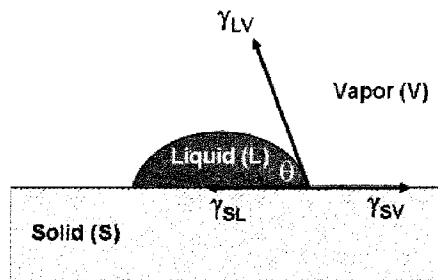


**Figure 5.14.** Schematic showing a drop of liquid on a solid substrate.

The tendency of a liquid to spontaneously spread on a substrate can be predicted by introducing the parameter of spreading coefficient,

$$S_{LS} = \gamma_{SV} - (\gamma_{LV} + \gamma_{SL})$$

such that if  $S_{LS} \geq 0$ , then the drop is predicted to spread, while for  $S_{LS} < 0$ , the drop is predicted to form a lens.

This spreading coefficient can be extended to a system where a liquid droplet (phase 1) is in contact with another immiscible droplet (phase 3) in the presence of a mutually immiscible liquid (phase 2) (Fig. 5.15). For example, if the spreading coefficient for phase 3 over phase 1,  $S_{31} > 0$  (which means 3 likes to spread on 1 and also that 1 does not want to interface with 2), and the spreading coefficient of phase 1 on phase 3,  $S_{13} < 0$  (which means 1 does not like to spread over 3), then 3 will spread over 1, thereby

engulfing it. In other words, when  $S_{31} > 0 \Rightarrow \gamma_{12} > (\gamma_{13} + \gamma_{23})$ , the formation of the 2-3 and 1-3 interface is much preferred over the formation of 12 interface.

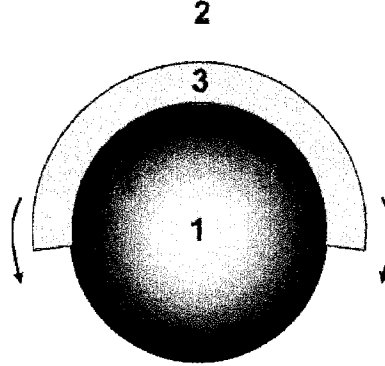


**Figure 5.15.** Schematic showing the spreading behavior of one liquid on another immiscible liquid droplet in the presence of a third mutually immiscible liquid.

Insight can be achieved by considering at all twelve possibilities of spreading coefficients ( $S_{ij}$ ,  $i, j = 1, 2, 3$ ,  $i \neq j$ ):

**Case 1.**  $S_{31} = \gamma_{12} - (\gamma_{23} + \gamma_{13})$

- (a) If  $S_{31} \geq 0$ , then  $\gamma_{12} > (\gamma_{23} + \gamma_{13}) \Rightarrow$  1-2 interface is not formed (1 avoids interfacing with 2; 3 spreads over 1, thereby avoiding the 1-2 interface formation).
- (b) If  $S_{31} < 0$ , then  $\gamma_{12} < (\gamma_{23} + \gamma_{13}) \Rightarrow$  1-2 interface is formed; 3 does not spread over 1, leading to the possibility of either discrete drop formation by 1 and 3, or 3 being engulfed by 1.

**Case 2.**  $S_{13} = \gamma_{23} - (\gamma_{12} + \gamma_{13})$

- (a) If  $S_{13} \geq 0$ , then  $\gamma_{23} > (\gamma_{12} + \gamma_{13}) \Rightarrow$  2-3 interface is not formed; 1 spreads over 3 leading to engulfing of 3.
- (b) If  $S_{13} < 0$ , then  $\gamma_{23} < (\gamma_{12} + \gamma_{13}) \Rightarrow$  2-3 interface is formed; 1 does not spread over 3.

**Case 3.**  $S_{32} = \gamma_{12} - (\gamma_{23} + \gamma_{13})$

(a) If  $S_{32} \geq 0$ ,  $\gamma_{12} > (\gamma_{23} + \gamma_{13}) \Rightarrow$  1-2 interface is not formed; 3 spreads over 2. This means that all of phase 2 gets engulfed in phase 3, which is not possible since phase 3 is a minor component and phase 2 is in excess.

(b) If  $S_{32} < 0$ , then  $\gamma_{12} < (\gamma_{23} + \gamma_{13}) \Rightarrow$  1-2 interface is formed; 3 does not spread over 2.

**Case 4.**  $S_{23} = \gamma_{13} - (\gamma_{12} + \gamma_{23})$

(a) If  $S_{23} \geq 0$ ,  $\gamma_{13} > (\gamma_{12} + \gamma_{23}) \Rightarrow$  1-3 interface is not formed because of which the contact of 1 and 3 with 2 is favored; hence 2 spreads over 1 and 3.

(b) If  $S_{23} < 0$ ,  $\gamma_{13} < (\gamma_{12} + \gamma_{23}) \Rightarrow$  1-3 interface is formed; 2 does not spread over 3.

**Case 5.**  $S_{12} = \gamma_{23} - (\gamma_{12} + \gamma_{13})$

(a) If  $S_{12} \geq 0$ , then  $\gamma_{23} > (\gamma_{12} + \gamma_{13}) \Rightarrow$  1-2 interface is not formed; 1 spreads over 2, which is not possible for reasons similar to Case 3a.

(b) If  $S_{12} < 0$ , then  $\gamma_{23} < (\gamma_{12} + \gamma_{13}) \Rightarrow$  1-2 interface is formed; 1 does not spread over 2.

**Case 6.**  $S_{21} = \gamma_{13} - (\gamma_{12} + \gamma_{23})$

(a) If  $S_{21} \geq 0$ ,  $\gamma_{13} > (\gamma_{12} + \gamma_{23}) \Rightarrow$  1-3 interface is not formed; 2 spreads over 1.

(b) If  $S_{21} < 0$ , then  $\gamma_{13} < (\gamma_{12} + \gamma_{23}) \Rightarrow$  1-3 interface is formed; 2 does not spread over 1.

Some of these possibilities for the spreading coefficient can be eliminated. For example, mathematically,  $S_{21}$  is the same as  $S_{23}$ . Also,  $S_{31} = S_{32}$  and  $S_{12} = S_{13}$ . Hence, we will take only  $S_{21}$ ,  $S_{31}$ , and  $S_{13}$  for our analysis.

The following five are the five possible configurations:

**(1) Complete engulfing (1 inside 3):** This occurs when the interfacial tension 12 exceeds the combined interfacial tensions 1-3 and 2-3. Hence  $S_{31} > 0$ , which essentially means that 3 likes to spread on 1. Also, since 1 does not like to spread over 3,  $S_{13} < 0$ . Water tries avoids forming an interface with 2, hence  $S_{21} < 0$ .

**(2) Partial engulfing (1 inside 3):** In this case, 3 does not like to spread over 1. Also 1 does not like to spread over 3. This should ideally give discrete droplet. However, since the major component, 2, does not like to spread over 1, it is energetically favorable to have a partially engulfed morphology wherein 1 is partially covered by 3. Detailed analysis on the extent of engulfing has been done by Torza and Mason [19].

**(3) Non-engulfing:** This case is quite straightforward since 1 does not like to spread on 3, and neither does 3 on 1. However, 2 likes to spread on each of them leading to the formation of discrete droplets.

**(4) Partial engulfing (3 inside 1):** This case is quite similar to partial engulfing with 1 inside 3, except for the fact that 2 does not like to spread over 3. Hence, the configuration with least surface energy would be partial engulfment of 3 inside 1.

(5) **Complete engulfing (3 inside 1):** In this case, 1 likes to spread over 3 and the majority fraction, 2 avoid to form an interface with 3. Hence 3 gets engulfed within 1 to give the structure with lowest surface energy.

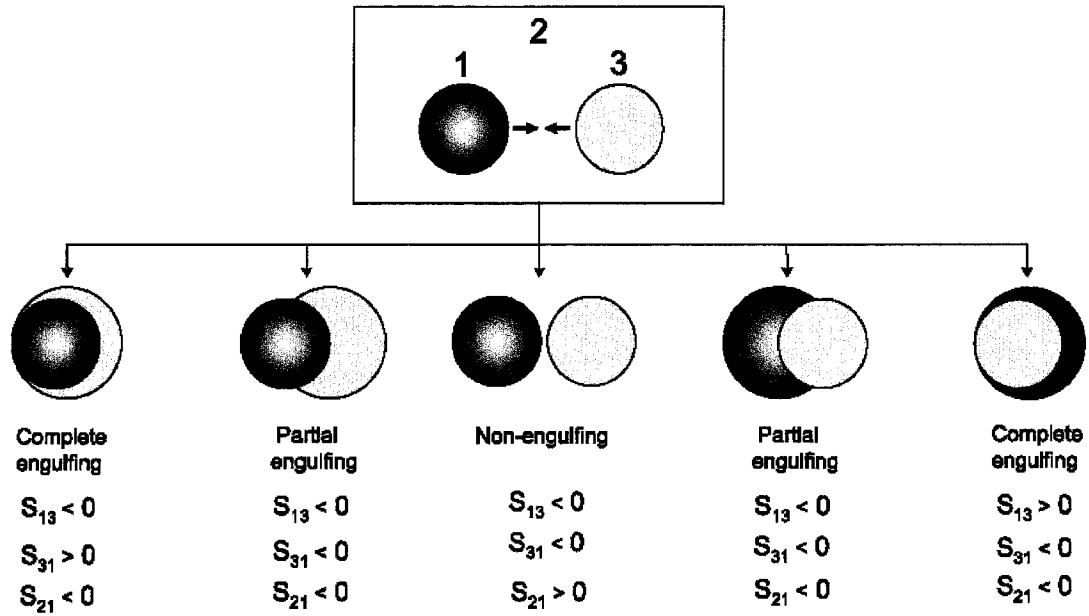


**Figure 5.16.** Possible equilibrium configurations when two immiscible droplets (phase 1 and 3) come in contact in the presence of a third mutually immiscible liquid (phase 2).

This model based on relative interfacial tensions between phases can be exploited to understand the morphologies obtained for PLL/PAH-cit/water system. From confocal microscopy images in Fig. 5.9, the composite aggregates from PLL/PAH-cit resembled structures akin to the complete engulfing case. For all PLL/PAH compositions, PAH domains were completely engulfed inside the PLL aggregates. We have also seen that when PLL-cit and PAH-cit aggregates were combined, the PLL-cit aggregates wrapped around the PAH-cit aggregates spontaneously leading to complete engulfing (Fig. 5.12). This clearly indicated that  $S_{\text{PAH-PLL}} < 0$ ,  $S_{\text{PLL-PAH}} > 0$ , and  $S_{\text{water-PAH}} < 0$ . From this,

relative magnitudes of the interfacial tensions can be deduced:  $\gamma_{\text{PAH-water}} > \gamma_{\text{PLL-water}}$  and  $\gamma_{\text{PAH-water}} > \gamma_{\text{PLL-PAH}}$ .

Quantification of the interfacial tensions for PAH-water, PLL-water, and PAH-PLL was not performed. Due to the highly viscous nature of phases formed by PLL-cit aggregates and PAH-cit aggregates, determining the interfacial tensions between the three phases was not possible with conventional techniques such as contact angle measurement. So far, we have not observed the other three morphologies (partial engulfing, discrete droplets, and PAH engulfing PLL domains) for our system.

First given by Harkins [20], and later applied to liquid droplets by Hobbs [21], this model has been successfully applied to predict structures for different systems such as polymer blends [18,22,23], latex particles [24], and for polymer phase separation in oil-in-water emulsions [25]. Guo *et al.* studied the phase morphologies obtained in ternary blends using different combinations of polystyrene, polyethylene, polypropylene, and poly(methyl methacrylate) [22]. In addition to interfacial tensions playing a prominent role, it was suggested that interfacial areas should also be considered, even if their role is not as significant. Furthermore, they demonstrated that phase structure of ternary polymer blends can be converted from one type to another by changing the interfacial tensions between one or more pairs of the components using surface active agents such as block or graft copolymers. Structures having geometries such as acorn shapes (due to partial engulfing) or non-engulfing systems have also been provided by workers [24,26]. In addition to Torza and Mason [19], theoretical studies have been performed by Mori [27] and Johnson and Sadhal [28].



### 5.3.5. Effect of PLL/PAH ratio on SiO<sub>2</sub>/polymer microsphere structure

The external and internal morphology of the microphase-separated composite aggregates could be preserved by mixing them with silicic acid to yield microspheres. Confocal images of microspheres obtained upon the addition of silica to aggregates of different PLL/PAH mixtures are shown in Fig. 5.17. For the 90/10, 75/25, and 50/50 mixtures (Fig. 5.17b-d), the PAH domains could be seen distributed inside the PLL-silica matrix. The size of the PAH domains increased with increasing PAH content. From image analysis, it was confirmed that the PAH domain sizes in the microspheres correlated well with the sizes in the corresponding PLL/PAH-cit aggregates (Fig. 5.9) for all compositions of PLL/PAH.

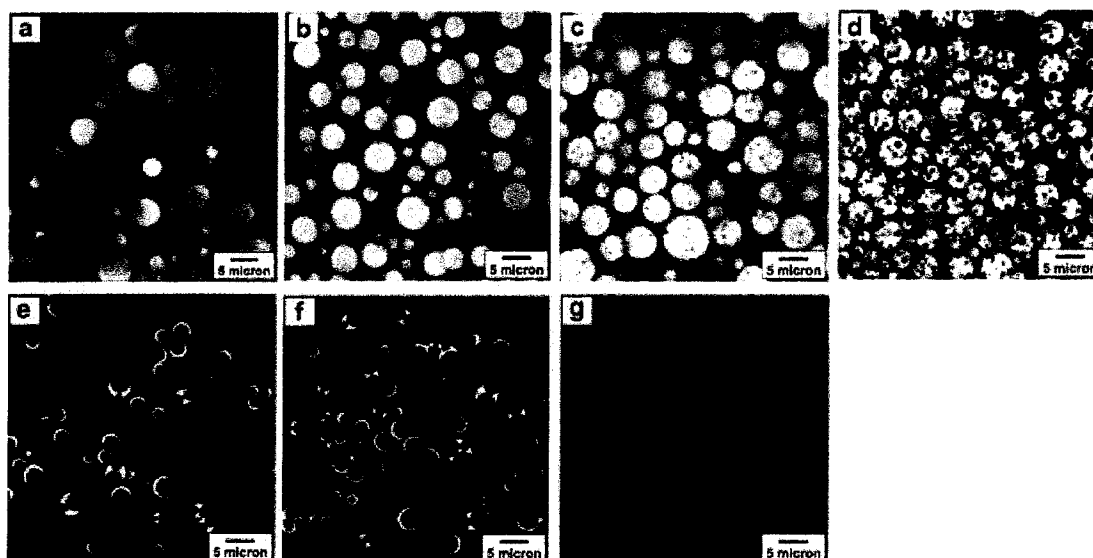


**Figure 5.17.** Confocal microscopy images of SiO<sub>2</sub>/polymer microspheres prepared from PLL-FITC/PAH-Rhod-cit aggregates with varying relative amounts of PLL/PAH: (a) 100/0, (b) 90/10, (c) 75/25, (d) 50/50, (e) 25/75, (f) 10/90, and (g) 0/100.

From the confocal images of microspheres with higher PAH content (25/75 and 10/90) in Fig. 5.17e,f, it was noted that the PAH cores seem to be situated eccentrically

such that a small area of PAH domain was exposed to water. Since the silicic acid templates the PLL/PAH-cit aggregates, it suggests that the PAH domains might have been situated eccentrically in the precursor PLL/PAH-cit aggregates. This was not reflected in Fig. 5.9e,f possibly because of secondary effects of electrostatic interaction between the aggregates and the glass coverslip, during which the aggregates tend to spread, hence, leading to a slight change in the aggregate internal structure. Similar structures with eccentric liquid core have been seen for double emulsions. Johnson and Sadhal in their detailed studies on compound multiphase drops attribute this eccentricity to the differences in drag forces experienced by the engulfed fluid and the composite droplet itself [28]. Concentric configuration is surmised to be only a special case of equilibrium configuration in complete engulfing wherein the body forces (such as gravity) on phase 1 is exactly balanced by the viscous forces which tend to drive it off-center. For all other cases, one should expect an eccentric core configuration.

Since the only parameter changing in Fig. 5.9 panel was the PLL/PAH ratio (due to which the interfacial tensions do not change), we suspected at least some of the PAH domains in the 90/10, 75/25, and 50/50 microspheres would also be slightly exposed to the interface. This was indeed seen to be the case as shown in Fig. 5.18, which shows SEM images of dried PLL/PAH silica microspheres. The size of the microspheres matched well with the sizes in the wet state from confocal image (Fig. 5.17). Upon closer analysis, surface protrusions were apparent, especially for 90/10, 75/25, and 50/50 mixtures (Fig 5.18b-d). These surface patches on the microspheres could not be discerned from the confocal image due to limited resolution. Hence, SEM images can be treated as complementary data for analyzing the surface structure of microspheres. Quantitative

data on the relative distribution of PAH domains on the surface and internally could not be obtained with both the techniques.

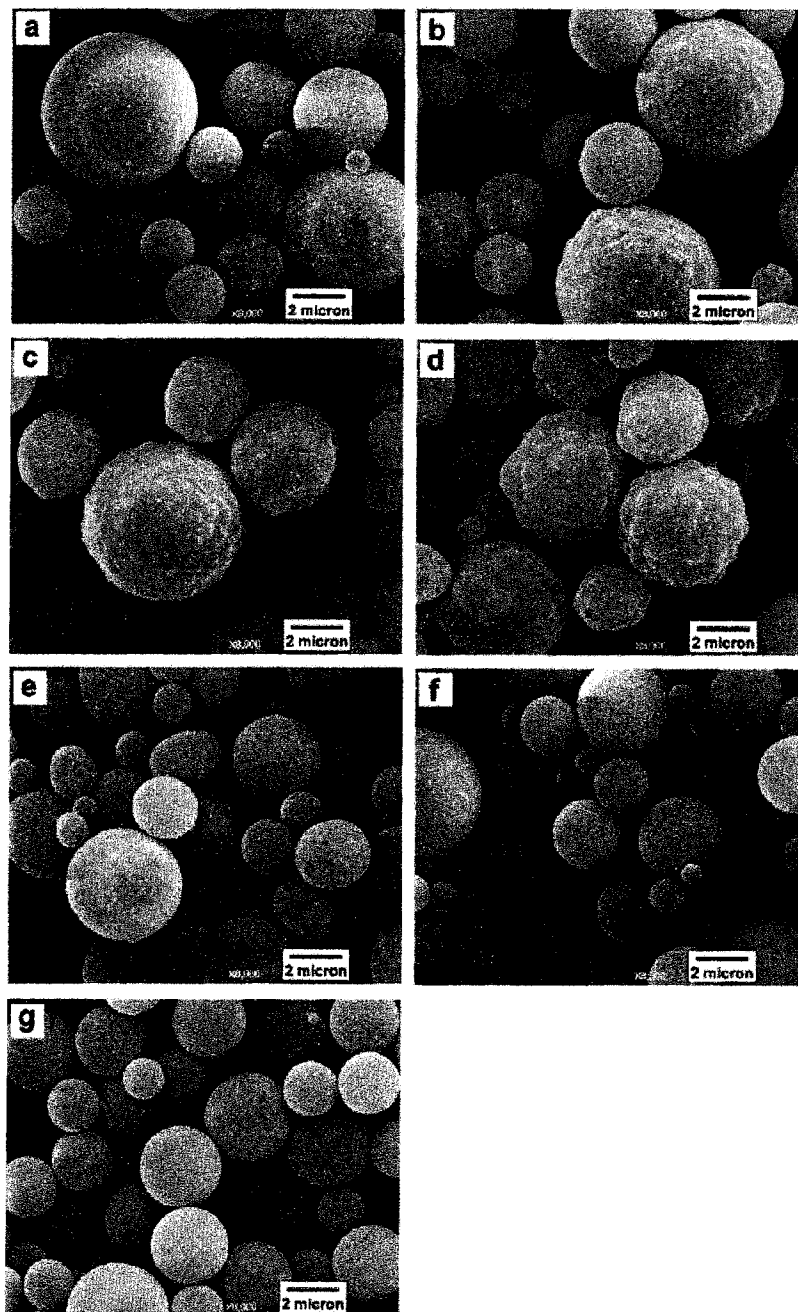


**Figure 5.18.** SEM images of SiO<sub>2</sub>/polymer microspheres with varying relative amounts of PLL/PAH. (a) 100/0, (b) 90/10, (c) 75/25, (d) 50/50, (e) 25/75, (f) 10/90, and (g) 0/100.

The surface-exposed PAH domains were not readily apparent for the 25/75 and 10/90 PLL/PAH microspheres (Fig. 5.18e-g). It is possible that when PAH domain size becomes approximately the same as the composite aggregates size, the surface protrusions become difficult to discern due to approximately equal radii of curvature. It may also be possible that the larger PAH domains do not show the same extent of protrusion as their smaller counterparts.

### **5.3.6. Anisotropic nanoparticle-assembled capsules**

Replacing the silica oligomers (in the form of silicic acid) with SiO<sub>2</sub> NPs yielded particles with completely different morphologies. Confocal images of these nanoparticle-assembled capsular structures (NACs) are shown in Fig. 5.19. Clearly, PLL formed a distinct shell wall upon interaction with the negatively charged SiO<sub>2</sub> NPs for all values of PLL/PAH. The internal core structure of the NACs was dependent on the PAH amount. For small amounts of PAH in the mixture (90/10 and 75/25), speckles of PAH were seen to decorate the inside shell wall of the NACs. This was probably a result of attractive forces between the SiO<sub>2</sub> NPs in the shell wall and PAH which drew the PAH domains towards the periphery. With an increase in PAH content (50/50, 25/75, and 10/90 mixtures), the cores were found to be partially filled up with PAH. In these cases, the PAH domains are perhaps undergoing coalescence amongst themselves to form larger domains. This was clearly apparent in Fig. 5.19d where one could observe only one or two domains in each NACs as against two or more domains in the precursor PLL/PAH-cit aggregates (Fig. 5.9d).

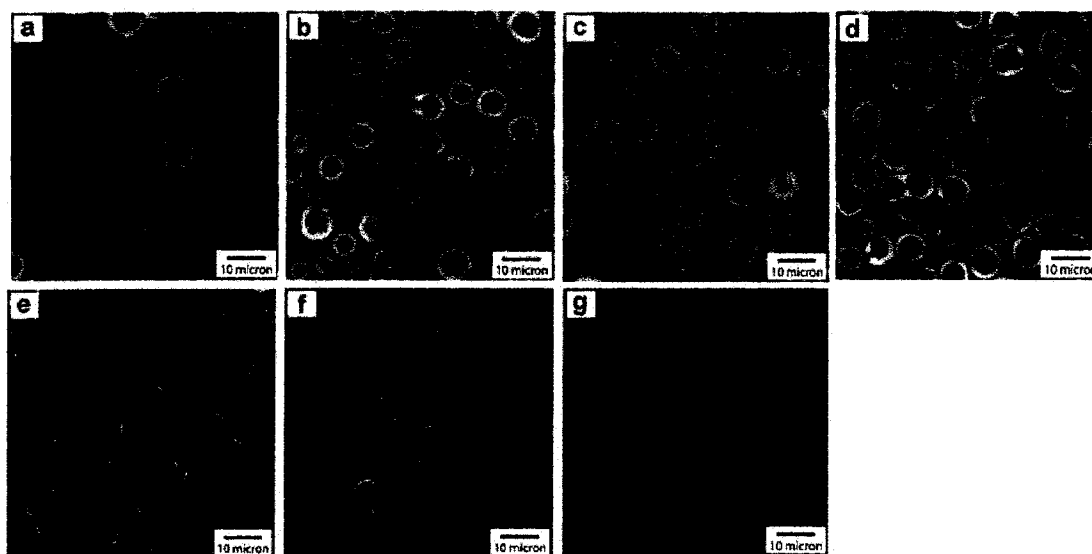


**Figure 5.19.** Confocal microscopy images of NACs prepared from PLL-FITC/PAH-Rhod-cit aggregates with varying relative amounts of PLL/PAH: (a) 100/0, (b) 90/10, (c) 75/25, (d) 50/50, (e) 25/75, (f) 10/90, and (g) 0/100.

It was intriguing to see that in all the structures PLL exclusively formed the shell wall while PAH either adhered to the inside of the shell or was confined to the core space. In our previous work, with PLL-cit-SiO<sub>2</sub> NP NACs we had observed that the PLL tends to preferentially localize in the shell wall leading to a hollowing effect. This was attributed to the disassembly of the PLL-cit aggregates on contact with SiO<sub>2</sub> NPs. On the other hand, in the case of PAH-cit-SiO<sub>2</sub> NP NACs, no such hollowing effect resulted and the core was observed to be polymer-filled. This was proposed to be due to stronger electrostatic interaction between PAH and cit molecules which do not disassemble as easily upon contact with SiO<sub>2</sub> NP. Applying this theory to the present system of composite aggregates constituting both PLL and PAH, we hypothesize that upon contact with SiO<sub>2</sub> NPs, both polymers behave in an individualistic manner independent of the presence of the other, meaning PLL will always form the shell irrespective of its location and PAH will either remain in the core, or is drawn towards the periphery if the domains

are small. An explanation for the hollowing effect observed for structures in Fig. 5.17f, is still lacking.

### 5.3.7. Spatio-selective localization of gold nanoparticles

Patchy particles make themselves amenable to selective functionalization with chemical groups. Taking advantage of the differences in the chemical entities present on the surface, one could selectively conjugate functional groups to sites located specifically in the patches. Our initial attempts stressed on exploiting the differences in  $pK_a$  values of amine groups located on PAH patches ( $pK_a \sim 8.5$ ) and amine groups of PLL ( $pK_a \sim 9.0$ ). Certain compounds, such as fluorescamine, bind to primary amine groups and fluoresce. If the amine groups are protonated, then the binding (hence fluorescence) does not take place.

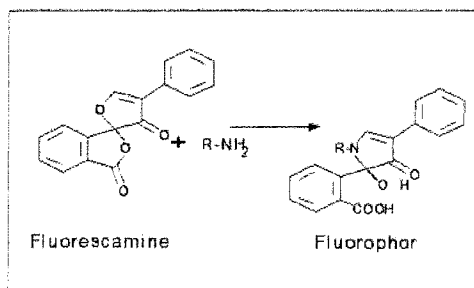


**Figure 5.20.** Reactions scheme showing the conjugation of non-fluorescence fluorescamine with primary amine groups to yield a fluorescent product.

Hence, we proposed that by contacting the patchy particles with fluorescamine at solution pH near the  $pK_a$  of PAH, we would be able to specifically conjugate PAH patches. However, it was observed that the fluorescamine was getting conjugating indiscriminately to both the polymers. This was thought to happen because of the close proximity of the  $pK_a$  values of both polymers. At pH close to the  $pK_a$  of PAH, PLL has a

certain fraction of its amine groups which are uncharged because of which they would bind to fluorescamine.

As route to fabrication of anisotropic microspheres with patchy surface, microphase segregation of polyamines also allows for spatio-selective localization of nanoparticles. Au NPs were used to demonstrate controlled localization in the aggregate ensemble. We had studied previously that Au NPs were able to interact electrostatically with the polyamines and could be confined inside the aggregates [29]. With this knowledge, we wanted to fabricate microspheres with patches containing Au NPs.

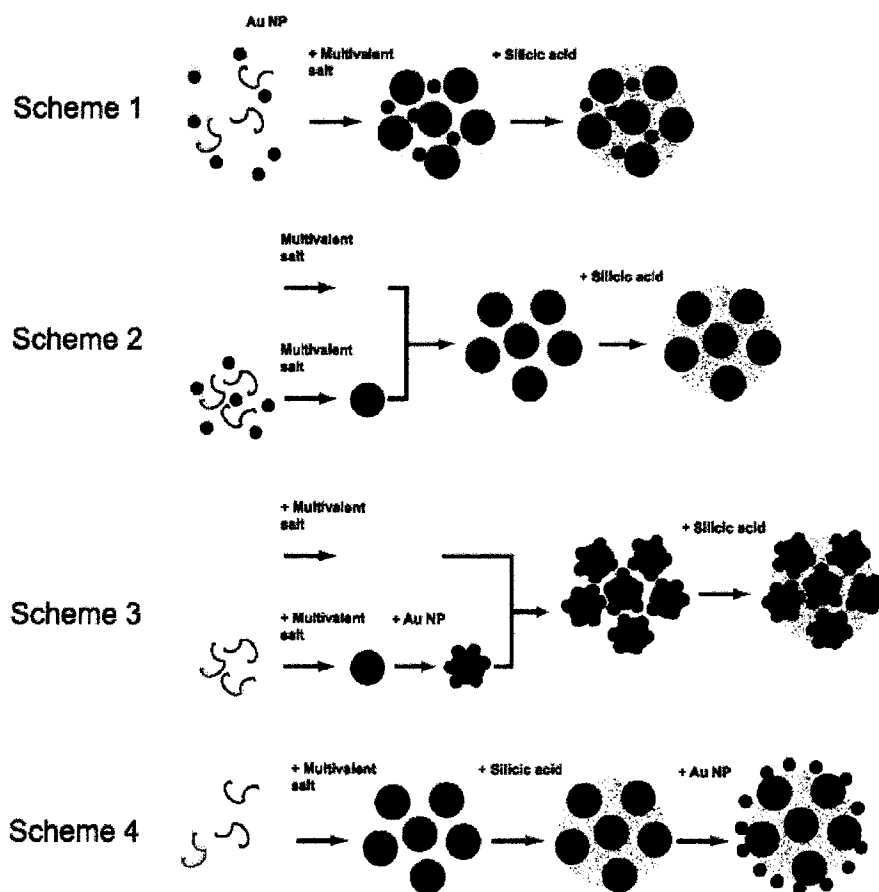


**Figure 5.21.** Schematic showing four possible modes to impart spatial control of Au NPs inside microspheres.

We explored four different ways to control Au NP distribution using our discovery of PLL/PAH-cit phase segregation and Au NP-PLL and Au NP-PAH aggregate formation (Fig. 5.19). Optical microscopy images of the resulting microspheres using a 50/50 mixture of PLL/PAH are shown in Fig. 5.20. The microspheres obtained through scheme 1 was observed to contain Au NPs throughout the particle. Since the Au NP was mixed homogeneously with the PLL/PAH mixture prior to adding of cit, the Au NP does not show any preferred localization in the composite aggregate and is present both in the PLL and PAH domains. Hence, after addition of silicic acid, the Au NPs remain scattered throughout the particle (Fig. 5.20a).

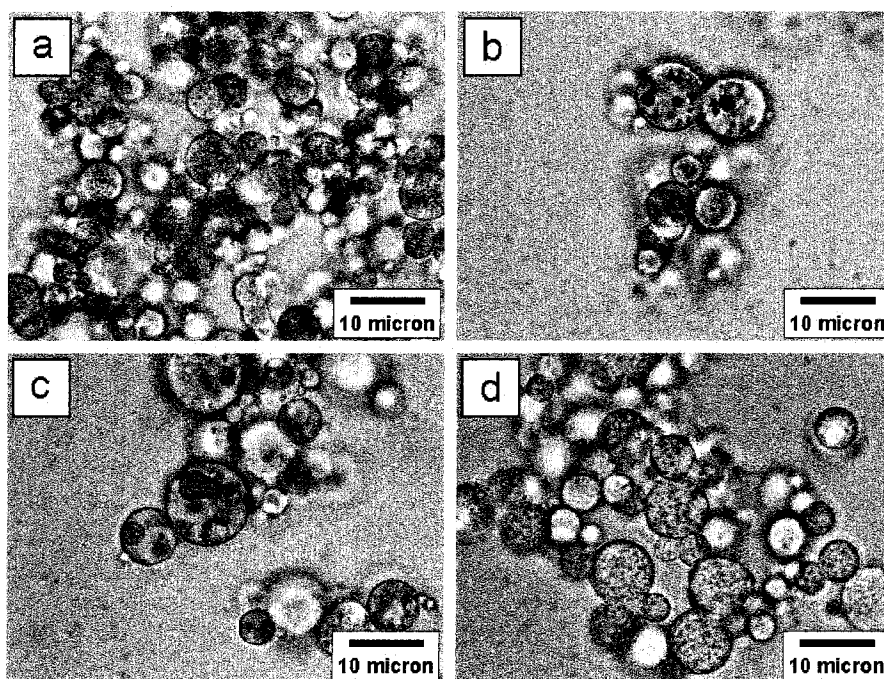


**Figure 5.22.** Optical microscopy images of PLL/PAH (50/50) silica microspheres with controlled localization of Au NPs (a) evenly located throughout the microspheres, (b) located only within the PAH domains, (c) located on the periphery of the PAH domains, and (d) located on the external surface of the microsphere.



In scheme 2, the Au NPs are initially confined in PAH aggregates and then mixed with PLL domains. Due to this, the Au NPs are confined in the PAH domains in the microspheres and can be seen as pink globules under the optical microscope (Fig. 5.20b). Addition of negatively charged Au NPs to pre-formed PAH aggregates, leads to their electrostatic adsorption on the aggregate surface (the PAH aggregates were verified to be positively charged). After mixing with PLL aggregates, the PAH domains get engulfed along with the Au NP coating. Under the optical microscope, a thin coating of Au NP was visible and was seen to be dark purple in color (Fig. 5.20c). This color is usually exhibited by Au NPs in close proximity to one another, especially in the case of aggregation. Lastly, when the Au NP was added to the preformed solid microsphere (scheme 4) and the suspension centrifuged, a light pink precipitate was observed and the supernatant became clear. This suggested that Au NP may have adhered electrostatically to the microsphere surface. In order to verify this, in a separate experiment, washed microsphere suspension was contacted with Coomassie reagent. Coomassie reagent upon reacting with the microsphere turned blue indicating the presence of positively charged amine groups on the microsphere surface. In our opinion, scheme 2 wherein the Au NPs are located on the PAH domains would lead to the desired  $\text{SiO}_2/\text{Au}$  microsphere structure. These Au NP patches can be further functionalized relatively easily using thiol groups or other functional entities.

## 5.4. Conclusions

In this work, we report a new phenomenon of microphase segregation of polyamines triggered by multivalent counterions by taking model polymer, poly(L-lysine

hydrochloride) and poly(allylamine hydrochloride). This segregation leads to polymer-salt aggregates with incomplete mixing of the polyamines yielding anisotropic morphology. The internal structure of the aggregates could be tuned by varying the relative amounts of PLL and PAH. The formation mechanism of composite PLL/PAH aggregates was explained by a coalescence mechanism. Two coalescence events were occurring: (1) the composite aggregates coalescing into larger aggregates, and (2) the internal PAH-cit domains that coalesced depending on the relative PLL/PAH amounts. Smaller amounts of PAH led to discrete domains and larger amounts to large, internal PAH domains which occupied the core. The spreading of PLL-cit aggregates on PAH-cit aggregates was thought to be due to higher interfacial tension between PAH/water as compared to PLL/water. Due to this, the PAH aggregates get completely engulfed within the PAH aggregates. The general shape and size of these aggregates could be preserved by contacting them with silicic acid. Solid microspheres with distinct surface patches was produced for lower PAH content. These surface patches were not seen for higher PAH content. Replacing silicic acid with SiO<sub>2</sub> NPs, led to NACs with different spatial distributions of PAH and PLL. Au NPs could be controllably localized within the composite aggregates, *i.e.*, either throughout the particle, in the interior of the PAH domains, on the surface of the PAH domains, or on the exterior surface of the silica microsphere.

## 5.5 References

- [1] Yin, Y., Alivisatos, A.P. Colloidal nanocrystal synthesis and the organic-inorganic interface *Nature*, **2005**, 437, 664.
- [2] Glotzer, S. Some assembly required *Science*, **2004**, 306, 419.

- [3] Zhang, Z., Glotzer, S. Self-assembly of patchy particles *Nano Letters*, **2004**, *4*, 1407.
- [4] Zhang, Z., Keys, A.S., Chen, T., Glotzer, S.C. Self-assembly of patchy particles into diamond structures through molecular mimicry *Langmuir*, **2005**, *21*, 11547.
- [5] Cayre, O., Paunov, V., Velev, O. Fabrication of asymmetrically coated colloidal particles by microcontact printing techniques *Journal of Materials Chemistry*, **2003**, *13*, 2445.
- [6] Lu, Y., Xiong, H., Jiang, X., Xia, Y., Prentiss, M., Whitesides, G. Assymmetric dimers can be formed by dewetting half-shells of gold deposited on the surfaces of spherical oxide colloids *Journal of the American Chemical Society*, **2003**, *125*, 12724.
- [7] Nakahama, K., Kawaguchi, H., Fujimoto, K. A novel preparation of nonsymmetrical microspheres using Langmuir-Bodgett technique *Langmuir*, **2000**, *16*, 7882.
- [8] Takei, H., Shimuzu, N. Gradient sensitive microscopic probes prepared by gold evaporation and chemisorption on latex spheres *Langmuir*, **1997**, *13*, 1865.
- [9] Choi, J., Zhao, Y., Zhang, D., Chien, S., Lo, Y. Patterned fluorescent particles as nanoprobe for the investigation of molecular interactions *Nano Letters*, **2003**, *3*, 995.
- [10] Love, J., Gates, B., Wolfe, D., Paul, K., Whitesides, G. Fabrication and wetting properties of metallic half-shells with submicron diameters *Nano Letters*, **2002**, *2*, 891.
- [11] Petit, L., Manaud, J., Mongotaud, C., Ravaine, S., Duguet, E. Sub-micrometer silica spheres dissymmetrically decorated with gold nanoclusters *Materials Letters*, **2001**, *51*, 478.
- [12] Fujimoto, K., Nakahama, K., Shidara, M., Kawaguchi, H. Preparation of unsymmetrical microspheres at the interfaces *Langmuir*, **1999**, *15*, 4630.

- [13] Petit, L., Sellier, E., Duguet, E., Ravaine, S., Mingotaud, C. Dissymmetric silica nanospheres: a first step to difunctionalized nanomaterials *Journal of Materials Chemistry*, **2000**, *10*, 253.
- [14] Roh, K., Martin, D., Lahann, J. Biphasic Janus particles with nanoscale anisotropy *Nature Materials*, **2005**, *4*, 759.
- [15] Jackson, A.M., Myerson, J.W., Stellacci, F. Spontaneous assembly of subnanometer-ordered domains in the ligand shell of monolayer-protected nanoparticles *Nature Materials*, **2004**, *3*, 330.
- [16] Rana, R.K., Murthy, V.S., Yu, J., Wong, M.S. Nanoparticle self-assembly of hierarchically ordered microcapsule structures *Advanced Materials*, **2005**, *17*, 1145.
- [17] Murthy, V.S., Rana, R.K., Wong, M.S. Nanoparticle-assembled capsule synthesis: Formation of colloidal polyamine-salt intermediates *Journal of Physical Chemistry B*, **2006**, submitted.
- [18] Reignier, J., Favis, B.D. Control of the subinclusion microstructure in HDPE/PS/PMMA ternary blends *Macromolecules*, **2000**, *33*, 6998.
- [19] Torza, S., Mason, S.G. Three-phase interactions in shear and electrical fields *Journal of Colloid and Interface Science*, **1970**, *33*, 67.
- [20] Harkins, W.D., *The Physical Chemistry of Surface Films*, Reinhold Publishing Co., New York, **1952**.
- [21] Hobbs, S.Y., Dekkers, M.E.J., Watkins, V.H. Effect of interfacial forces on polymer blend on morphologies *Polymer*, **1988**, *29*, 1598.
- [22] Guo, H.F., Packirisampy, S., Gvozdic, N.V., Meier, D.J. Prediction and manipulation of the phase morphologies of multiphase polymer blends: 1. Ternary systems *Polymer*, **1997**, *38*, 785.
- [23] Legros, A., Favis, B.D., Carreau, P., Michel, A. Morphology modification by interfacial chemical reaction in a polyester/ethylene vinyl acetate/polyethylene blend *Polymer*, **1997**, *38*, 5085.

- [24] Chen, Y.-C., Dimonie, V., El-Aasser, M.S. Effect of interfacial phenomena on the development of particle morphology in a polymer latex system *Macromolecules*, **1991**, *24*, 3779.
- [25] Loxley, A., Vincent, B. Preparation of poly(methylmethacrylate) microcapsules with liquid cores *Journal of Colloid and Interface Science*, **1998**, *208*, 49.
- [26] Shao, Y., van de Ven, T.G.M. Spinning of partially engulfed droplets *Langmuir*, **1989**, *5*, 1234.
- [27] Mori, Y.H. Configuration of gas-liquid two-phase bubbles in immiscible liquid media *International Journal of Multiphase Flow*, **1978**, *4*, 383.
- [28] Johnson, R.E., Sadhal, S.S. Fluid mechanics of compound multiphase drops and bubbles *Annual Review of Fluid Mechanics*, **1985**, *17*, 289.
- [29] Murthy, V.S., Cha, J.N., Stucky, G.D., Wong, M.S. Charge-driven flocculation of poly(L-lysine)-gold nanoparticle assemblies leading to hollow microspheres *Journal of the American Chemical Society*, **2004**, *126*, 5292.

## **Chapter 6. Summary and recommendations for future work**

In this dissertation, a simple mix-and-shake approach to assemble charged nanoparticles (NPs) and polymers into functional microcapsules was studied. Positively charged polymers when combined with negatively charged multivalent ions formed spherical, micron-sized polymer-salt aggregates in aqueous medium. It was theorized that the anions ionically crosslinked the polymer to form a three-dimensional network. Robust microcapsules were obtained by mixing negatively charged NPs with the aggregate suspension, around which the NPs form a shell to create nanoparticle-assembled capsules (NACs). This NP assembly route was demonstrated to be the easiest method to synthesize stable capsule structures. The chemistry was generalized to a variety of different polymers, multivalent salts, and NPs opening up exciting opportunities to tailor the structural and functional properties of capsules for specific applications. The benign synthesis conditions allowed non-damaging encapsulation of sensitive molecules such as enzymes. With acid phosphatase as the model enzyme, synthesis, characterization, activity, and recoverability of enzyme-containing NACs were studied. Finally, an intriguing aspect of microphase segregation of polyamines was examined which led to solid particles with surface patches and anisotropic internal structure (“patchy” particles).

For future work, it is highly recommended to start by investigating the possibility of controlling the interior and exterior morphology of the patchy particles. In particular, methods to control the size, location, and number of surface patches needs to be researched on a war-footing. Further, selective functionalization of these patches with specific recognition elements can lead to self-assembly of particles giving ordered structures. Such spatio-selective functionalization of particles in the (sub)micron range

has itself been a formidable challenge for surface and colloid scientists, not to mention taking a step further to assemble these particles into ordered structures. Microphase segregation of polyamines opens up new opportunities for fascinating research work. Phase separation obtained by using three (or more) polymers can lead to interesting morphologies. Also by selectively functionalizing the patches with two or more types of NPs (*e.g.*, Au, Ag, and Pd NPs) can lead to avenues in optical and catalytic applications.

Systematic studies on transport and structural properties of NACs have been lacking so far. Material properties of NACs such as shell porosity, molecular weight cut-off, and mechanical strength of NACs are needed so that the NACs can be rationally engineered for applications in encapsulation and controlled delivery of drugs, dyes, and other compounds. With work related to enzyme encapsulation, a knowledge of the transport parameters would also help explain the diffusion limitations imposed by the shell wall and the various parameters which can be used to tune the same.

Control of size dispersity of NACs has been a challenge so far. Although we have demonstrated good control over the size dispersity of precursor polymer-salt aggregates in the <200 nm size range, the polymer-salt aggregates tends to become polydisperse above this size, giving capsules in a broad size range. In order to solve this issue, it is recommended to borrow concepts and best practices from a lateral field, such as emulsion technology, and apply it to our system. Continuous synthesis route (as against batch process) could be investigated as an option for generating monodisperse NACs. Microreactors are one system which can be used for continuous generation of NACs. Microreactors are devices that enable reactions to be carried out on the microliter scale. They can be fabricated by etching channels on a solid substrate. For our system,

microreactors can also be used for studying the NAC formation, *in situ*. Preliminary work to set up microreactors made from polydimethoxysilane (PDMS) is being carried out.

The work done so far has been limited to cationic polymer, multivalent anions, and negatively charged NPs. It would be fulfilling to conduct research in the reverse charged system constituting anionic polymer, multivalent cations, and positively charged NPs to see whether NP assembly chemistry could be generalized further. While much is known with DNA-cation aggregates, we are not aware of capsule formation with reverse-charged polymer aggregates. Our preliminary attempts to encapsulate positively charged compounds in the NACs core have not been very successful. Through the use of oppositely charge system, we may be able to achieve this successfully.



## Appendix A. Nanoparticle Self-Assembly of Hierarchically Ordered Microcapsule Structures\*

As a process by which molecular subunits spatially organize into well-defined supramolecular structures through non-covalent interactions, self-assembly is becoming a powerful synthesis approach for generating advanced materials out of nanoparticle (NP) building blocks [1-5]. Highly structured NP assemblies, such as wires, rings, and superlattices, can be prepared on flat surfaces [6-17]. However, ordered NP-based structures remain difficult to prepare in the unsupported colloidal form [18-23], limiting the prospects of the latter for practical applications (such as drug delivery and catalysis). Here, we identify the solution conditions under which inorganic NPs effectively self-assemble into hierarchically ordered closed-shell structures in the presence of polymer. We demonstrate that, in a tandem two-step process, cationic polyamines form supramolecular aggregates with multivalent counter-anions via ionic crosslinking, and negatively-charged NPs deposit around these aggregates to form a multilayer-thick shell. The resulting organic/inorganic hybrid microcapsules contain polymer or water in the core interior, depending on the multivalent anion used. In this work, we analyze the polymer aggregation step and present a new preparative route that we term tandem self-assembly.

Rotello and co-workers showed that appropriately functionalized gold NPs could be induced to self-assemble into micron-sized spherical aggregates by using polymer chains specially designed with complementary hydrogen bonding pendant groups [22]. Stucky and co-workers later showed that diblock copolypeptides could mediate NP self-assembly to form hollow microspheres, in which cysteine and lysine polymer

---

\* Rana, R.K., Murthy, V.S., Yu, J., Wong, M.S. Nanoparticle self-assembly of hierarchically ordered microcapsule structures *Advanced Materials*, **2005**, *17*, 1145.

blocks bind to gold and silica NP surfaces, respectively [23]. Hollow sphere (alternatively, capsule or shell) structures function as encapsulation, protection, and delivery agents, and are used in application areas as diverse as medicine, foods, cosmetics, and paints [24,25]. Further research indicated that Au NP/polymer aggregates were important intermediates in the formation of the hollow spheres [26,27]. In the course of studying this NP self-assembly process, we observed that poly(*L*-lysine) chains undergo counterion condensation in certain salt solutions to form polymer aggregates, and discovered that these ionically crosslinked polymer aggregates lead to the rapid formation of ordered microcapsule structures.

The room-temperature synthesis of microcapsules (or nanoparticle-assembled capsules, NACs) is illustrated by using poly(*L*-lysine) (PLL) conjugated to fluorescein isothiocyanate (FITC) dye. In a typical preparation, 21  $\mu\text{l}$  of a FITC-tagged PLL solution (2 mg/ml, 68 kDa, HBr salt) is gently mixed for 10 sec with 125  $\mu\text{l}$  of a tetrasodium ethylenediamine tetraacetate solution ( $\text{Na}_4\text{EDTA}$ , 4.02 mM) or with a trisodium citrate solution ( $\text{Na}_3\text{Cit}$ , 5.36 mM) (Figure A.1a). The overall charge ratio  $R$  of total negative charge of the added salt to total positive charge of the polymer ( $R = [\text{anion}] \times |z_-| / [\text{polymer}] \times |z_+|$ , where  $z_-$  is negative charge per anion and  $z_+$  is positive charge per chain) is 10. This slightly cloudy polymer/salt solution is aged for 30 min and then vortex mixed with 125  $\mu\text{l}$  of a silica sol (particle diameter of  $13 \pm 3$  nm, 20 wt%  $\text{SiO}_2$ , pH  $\sim 3.4$ ) for 20 sec. The immediate increase in turbidity is due to microcapsule formation. The as-synthesized colloidal assemblies are spherical and have a core/shell morphology with diameters primarily in the 1-4  $\mu\text{m}$  size range, according to optical microscopy images (Figures A.1c,e) and Coulter counter size measurements. The microcapsule yield is estimated from fluorospectroscopy

measurements to be 85-90%, on a polymer weight basis. According to TGA results,

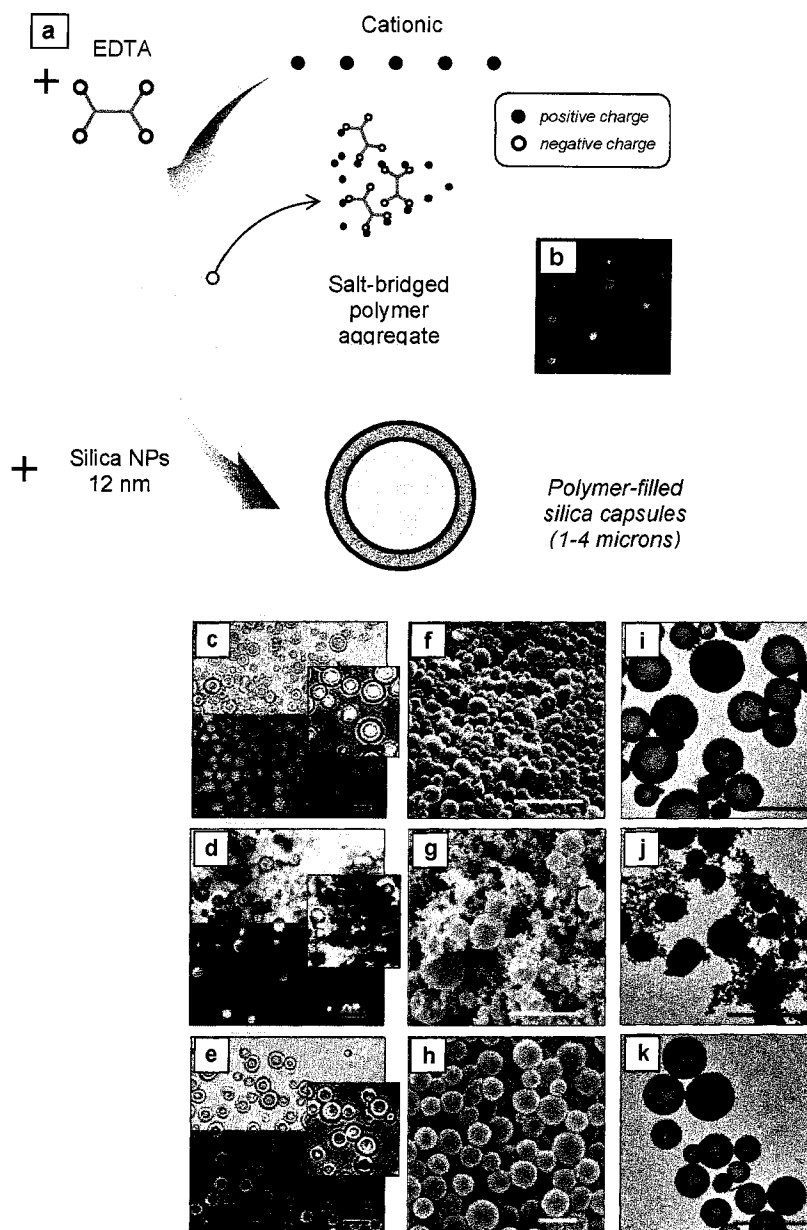


**Figure A.1.** Tandem self-assembly of microcapsules. **(a)** Proposed schematic of the tandem, two-step formation process, in which positively-charged polymer chains ionic crosslink with multivalent anions, and silica NPs subsequently deposit around the polymer aggregates. **(b)** Confocal microscopy image of EDTA-bridged PLL-FITC aggregates. **(c-e)** Brightfield and confocal and (Inset) combined confocal/brightfield images of three different silica structures suspended in water, and **(f-h)** SEM and **(i-k)** TEM images of the corresponding dried structures: (c,f,i) microcapsules self-assembled from SiO<sub>2</sub> NPs, EDTA, and PLL, (d,g,j) microspheres synthesized using silicic acid, EDTA, and PLL, and (e,h,k) microcapsules self-assembled from SiO<sub>2</sub> NPs, citrate, and PLL. All scale bars, 5  $\mu$ m.

the microcapsules have a volatiles content (which includes the salt and polymer) in the 12-15 wt% range, indicating that these organic/inorganic NAC materials are composed mostly of silica.

Contrasting the sequential layer-by-layer adsorption of colloidal species around sacrificial templates to yield hollow and filled spheres [25,28], the above two-step sequence forms the basis of the tandem self-assembly model (Figure A.1a). We followed the process through optical and confocal microscopy using FITC-tagged PLL. The polymer forms globular aggregates upon addition of EDTA (Figure A.1b), which then yield microcapsule structures (with sharply defined inner and outer perimeters observed in Figure A.1c) upon the addition of SiO<sub>2</sub> NPs. The polymer aggregates are necessary for microcapsule formation, as confirmed by a negative control experiment in which combining SiO<sub>2</sub> NPs with a PLL solution resulted in randomly structured aggregates. The microcapsules have the PLL located in the core interior and within the shell wall, where the positively charged polymer chains are interspersed with the negatively charged SiO<sub>2</sub> NPs.

The microcapsules are structurally robust, exhibiting no apparent damage after being subjected to centrifugation and drying steps used for electron microscopy sample preparation (Figures A.1f-k). Confocal, SEM, and TEM image analysis of as-synthesized and dried materials indicated contraction of ~20-25% and ~5-10% for EDTA-derived and citrate-derived microcapsules, respectively. The former material had thinner shell walls (~150-200 nm) than the latter (~250 nm), and thus contracted to a greater extent.

The thick microcapsule shell walls are inconsistent with Langmuir-type adsorption of SiO<sub>2</sub> NPs around the polymer aggregates, which should yield a shell wall one NP thick (~12 nm). We propose that the NPs penetrate the surface exterior of

the polymer aggregate and that the penetration depth determines the shell thickness, with the implication that smaller particles diffuse deeper into the polymer aggregate than larger particles. Indeed, replacing the  $\text{SiO}_2$  particles with oligomeric silicate clusters ( $\sim 1$  nm) in silicic acid preparations (Supplementary Materials) led to spheres with thicker shells and even solid silica cores (Figures A.1d,g,j). These particular polymer/silica structures are reminiscent of those reported by the groups of Sumper and Clarson [29-31].

The concept of ionic crosslinking between the polymer and salt species provides a simple and informative way to understand polymer aggregation. The effect of reducing the total number of anion carboxylate groups (negatively-charged binding sites) from 4 to 3 can be gauged by replacing EDTA with citrate anions. Citrate anions caused PLL to form aggregates, which also led to microcapsules after contacting with  $\text{SiO}_2$  NPs (Figures A.1e,h,k). Unlike the EDTA-derived materials, however, the citrate-derived microcapsules contained the polymer mostly in the shell wall. We speculate that the citrate-bridged PLL aggregate was not as crosslinked (and therefore not as structurally stable) as the EDTA-bridged aggregate, leading to its deaggregation or its self-collapse after the shell wall was formed. This crosslinking density argument could explain the observed difference in shell thicknesses;  $\text{SiO}_2$  NPs penetrate less deeply into the higher-crosslinked EDTA-bridged aggregates, which results in the thinner shell of EDTA-derived microcapsules.

The thermodynamically favored formation of carboxylate-ammonium salt bridges drives ionic crosslinking between the multivalent anions and polyamines[32,33], but the presence of carboxylate and ammonium groups is an insufficient condition for polymer aggregation. A minimum number of binding sites in the anion is required, as found for PLL and PAH (polyallylamine hydrochloride) (Table A.1). Curiously,

divalent carboxylate anions (*e.g.*, succinate and malonate) and sulfate anions did not cause PLL to aggregate, but did so with PAH. The aggregation process is apparently sensitive to polymer molecular structure. We found that other polyamines like poly(*L*-arginine) and poly(ethyleneimine) formed aggregates with citrate anions, as long as the pH of the synthesis medium was below the polyamine  $pK_a$ 's ( $\sim 9.5$ -11). Aggregation occurred over a wide range of polymer molecular weights (10-250 kDa), with the longer chains tending towards larger polymer aggregates.

**Table A.1.** Various sodium salt forms that were used for microcapsule synthesis from PLL (222 kDa) or PAH (70 kDa) and SiO<sub>2</sub> NPs. Charge ratio *R* was kept at 10 for all the experiments.

Anions	Structure	Salt form	pH of PLL/salt suspension	Polymer aggregate formation?	Microcapsule formation?
Chloride	$Cl^-$	NaCl	5.5	×	×
Acetate	$H_3C-C(=O)O^-$	Na acetate	6.6	×	×
Sulphate	$O=S(=O)([O-])[O-]$	Na <sub>2</sub> SO <sub>4</sub>	6.8	×	×
Malic Acid	$H_2C-COO^-$   $HOOC-CH-OH$	Na <sub>2</sub> hydroxy succinate	6.6	×	✓ (for PAH)
Succinate	$H_2C-COO^-$   $H_2C-COO^-$	Na <sub>2</sub> succinate	7.2	×	✓ (for PAH)



form of  $\text{H}_3\text{cit}$  and  $\text{H}_2\text{cit}^-$  species at pH values below 5. Thus, solution pH controls the effective charge (and therefore binding site number) of the multivalent anion, and polymer aggregation proceeds within a pH window defined by the  $\text{pK}_a$ 's of the anionic salts and polyamines.

The polymer aggregates grow in size with aging time through coalescence. To gain an understanding of the polymer aggregation dynamics, we focused on citrate-bridged PAH aggregates (Figure A.2a). Aggregation formation was immediate after citrate addition, with the hydrodynamic diameter ( $D_h$ ) of the PAH solution measured at  $\sim 110$  nm (before citrate addition) and  $\sim 700$  nm (2 min after citrate addition). For comparison, addition of a NaCl solution at the same charge ratio ( $R = 10$ ) and at higher concentrations did not induce PAH aggregation; instead, PAH contracted ( $D_h \sim 30$  nm) due to Coulombic screening of the positive charged ammonium units. Crosslinking between the citrate and the PAH could be tracked by measuring the increase in free chloride concentration caused by the displacement of  $\text{Cl}^-$  bound to the polymer backbone [34]. Chloride potentiometric measurements of the PAH-only solution indicated that 26% of the total  $\text{Cl}^-$  were dissociated, and that one citrate molecule displaced  $\sim 2.2$   $\text{Cl}^-$  ions, based on the initial slope of the Cl dissociation curve (Figure A.2b). Although the polymer aggregates are metastable, they are apparently rigid to allow for NP deposition and shell formation; the addition of  $\text{SiO}_2$  NPs to the aggregate suspension aged at different times results in microcapsules of tunable diameters (Figures A.2c,d).



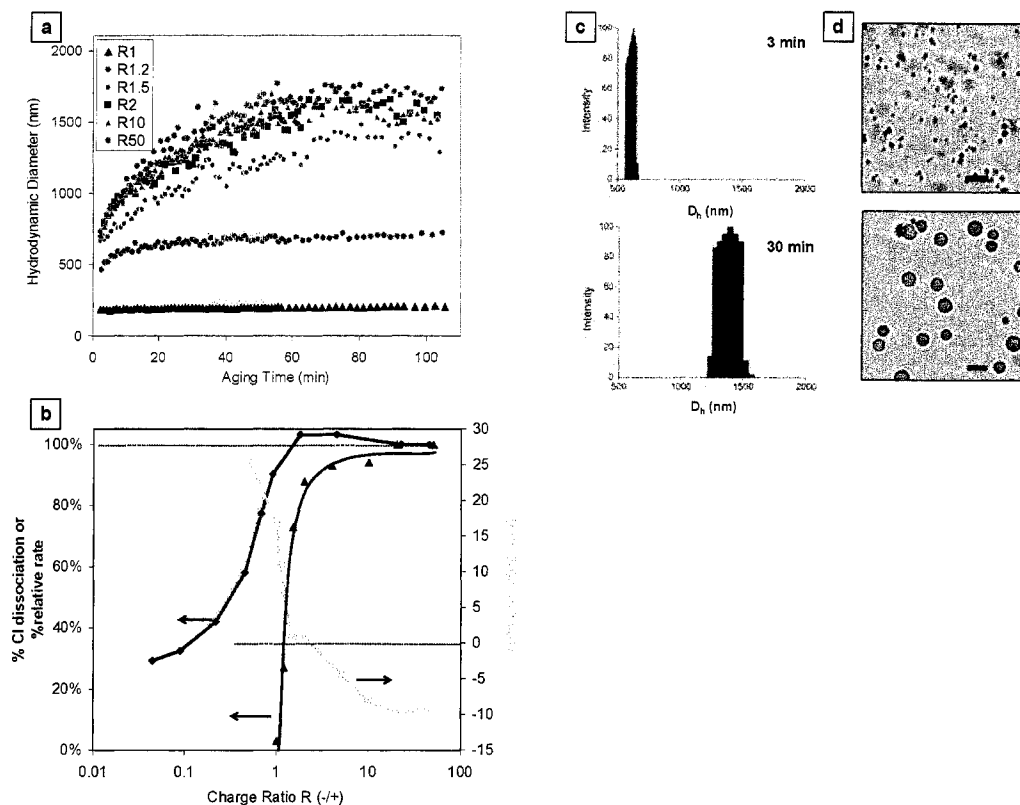


**Figure A.2.** Citrate-bridged PAH aggregates in microcapsule formation. **(a)** Aggregate growth curves of citrate and PAH suspensions at different charge ratios  $R$ . The charge ratio was adjusted with varying amounts of citrate. The citrate and polymer were combined at an aging time of 0 min. The suspensions could not be analyzed at times earlier than ~2 min due to experimental limitations. **(b)** Aggregate growth rates (at 2 min, determined from growth curves of (a)), zeta potentials, and %dissociation of Cl ions at different  $R$ 's. Growth rates were normalized to maximum growth rate (found at  $R = 50$ ). **(c)** Size distributions of citrate-bridged PAH aggregate ( $R = 10$ ) at 3 min and 30 minutes. **(d)** Optical microscopy images of microcapsules prepared from corresponding PAH aggregates. Scale bars, 5  $\mu\text{m}$ .

The charge ratio  $R$  governs the formation and growth rate of the salt-bridged polymer aggregates, which can be rationalized through the DLVO (Derjaguin-Landau-Vervey-Overbeek) theory of colloidal stability [35]. Namely, a suspension of charged colloidal particles is kinetically stable to aggregation if the particle surfaces are sufficiently charged to repel one another. Polymer aggregation occurs at  $R > 1$ , which is coincident with the near complete removal of  $\text{Cl}^-$  ions from the PAH by the

citrate anions (Figure A.2b). The  $\zeta$ -potentials of the polymer aggregates decrease in magnitude and eventually assume negative values with increasing  $R$  values with the observed charge reversal resulting from citrate anions binding to the aggregate exterior. The aggregates remain insufficiently charged ( $-10 \text{ mV} < \zeta < +10 \text{ mV}$ , between  $R = 1.2$  and  $R = 50$ ) to prevent contact with each other and with  $\text{SiO}_2$  NPs, allowing for fast aggregate growth and shell formation, respectively.

**Table A.2.** Negatively-charged colloidal species self-assemble into microcapsule structures [a].

NP (or polymer) composition	Particle size (or molecular weight)	pzc (or pKa)	pH of microcapsule suspension	Zeta potential (mV)
$\text{SiO}_2$	10-20 nm	2	6.0	-13
ZnO	50-90 nm	9	8.9	-41
$\text{SnO}_2$	10-15 nm	4-7	9.0	-20
CdSe	3-5 nm	—	7.6	-30
Carboxylated polystyrene	20 nm	—	7.2	-26
PAA	30 kDa	4.8	8.5	—
PSS	70 kDa	1	8.4	—

[a] The colloidal species (NPs and anionic polyelectrolytes) were added to a suspension of either (FITC tagged)-PLL/citrate or PAH/citrate suspension after aging for 30 min ( $R = 10$ ). Microcapsules of 1-6  $\mu\text{m}$  diameter were typically formed, as evaluated through a combination of optical and fluorescence microscopies. Electrophoretic mobilities of PAA and PSS confirmed the negative charges of the polymers.

We have found the concept of tandem self-assembly of charged nanoparticles and polymer molecules to be broadly applicable. NPs of other metal oxide compositions, such as tin oxide and zinc oxide, can be used to generate capsular structures as long the particle surface is negatively charged under the synthesis conditions (Table A.2).

This condition is ensured if the suspending fluid pH is higher than the point-of-zero charge of the metal oxide [35]. Other NPs having negatively charged surface species, such as citrate-stabilized CdSe and carboxylated polystyrene beads can also be used to make microcapsules. Interestingly, negatively-charged linear polyelectrolytes like poly(acrylic acid) (PAA) and poly(styrene sulfonate) (PSS) can also yield microcapsular structures, in which they presumably take the place of silica NPs in the shell formation step (images are not shown for brevity).

Polymer aggregates can also be supported on surfaces to template the formation of capsular hybrid structures (Fig. A.3). Citrate-bridged PAH aggregates adsorbed on a mica surface, which appear as flattened spheres due to spreading, lead to dome-like shells after contacting with SiO<sub>2</sub> NPs (Fig. A.3).

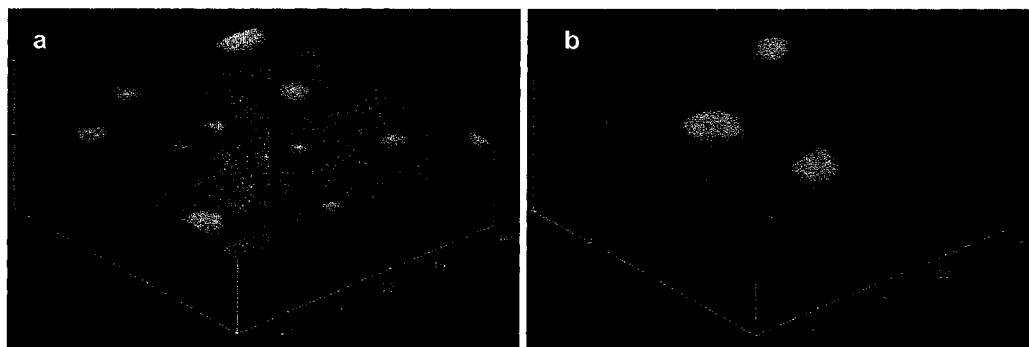


**Figure A.3.** Tapping mode AFM of (a) citrate-bridged PAH aggregates and (b) microcapsules formed on a mica support. After aging the citrate-bridged PAH suspension for 30 min, 100  $\mu$ l of the suspension was dropped on a freshly cleaved mica surface. After 1 min, the suspension was rinsed with deionized water, and the substrate dried overnight before imaging. For the microcapsule formation, 100  $\mu$ l of silica colloidal suspension was dropped on to the above freshly added PAH aggregates on a mica support. It was then aged for 30 min, rinsed with deionized water and then dried overnight before imaging. Height scale, 4  $\mu$ m.

The rapid generation of microcapsules in an aqueous medium is amenable to the facile encapsulation of water-soluble compounds, for example, by adding a solution of the desired cargo to a PLL/citrate suspension prior to adding the silica sol. To test the feasibility of microcapsules as reaction vessels [36,37], we encapsulated acid phosphatase enzyme at a loading of 0.15 mg/(mg microshell) and suspended the spheres in a solution containing fluorescein diphosphate, a non-fluorescent molecule. Fluorescence emerged and grew in intensity inside the microcapsule and within the shell wall over a course of 40 min, due to the formation of fluorescein from enzymatic cleavage of the phosphates (Figure A.4). We could not discern if the enzyme

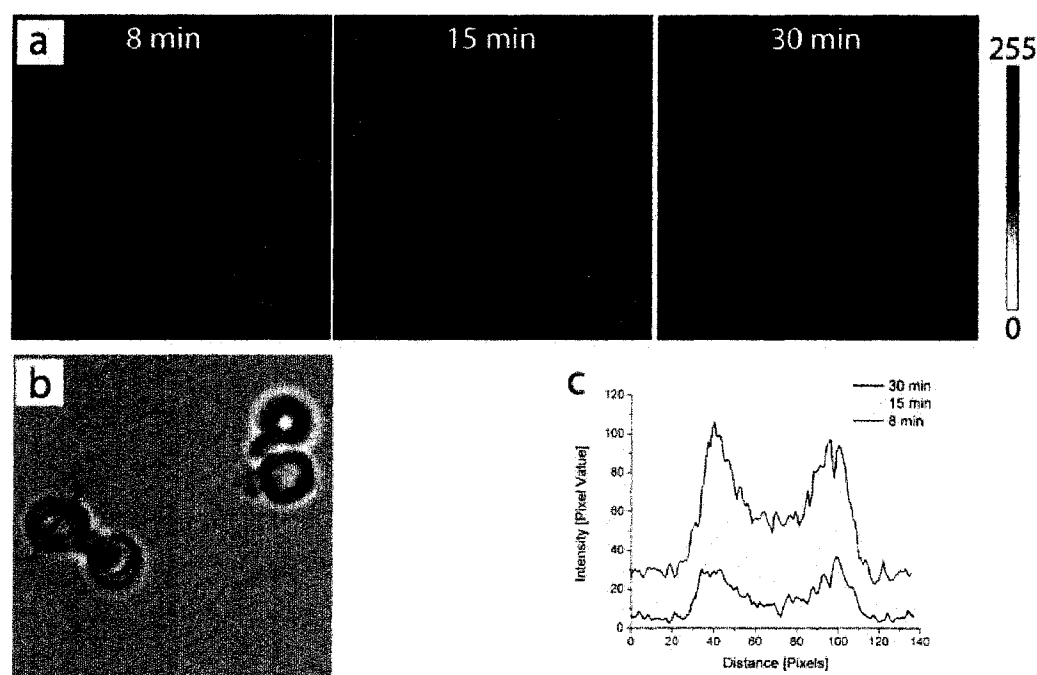


**Figure A.4.** Representative microcapsules prepared from citrate-bridged PLL aggregates and SiO<sub>2</sub> NPs that contain *acid phosphatase* enzyme, in an aqueous solution containing fluorescein diphosphate: **(a)** a series of time-lapse confocal microscopy images collected over the course of 30 min, **(b)** brightfield image, and **(c)** line intensity profiles along the red line shown in (b). The reactant diffuses inside the microcapsules and interacts with the encapsulated enzyme to form the fluorescent fluorescein product. Scale bars: 2  $\mu$ m.

molecules were located inside the microcapsule, within the shell wall, or both, but confocal analysis indicated clearly the generated fluorescein was accumulating inside the shell wall and in the interior before diffusing out after 15 min. Vigorous mixing or sonication did not noticeably degrade the microcapsule structure or the contained enzyme. The microcapsules allow the confined enzymes to function in a protected environment, and allow the reactant and product molecules to transport across the permeable shell walls.

In conclusion, we demonstrate that electrostatic interactions at the molecular and nanometer levels can be employed in the self-assembly of highly structured, nanoparticulate-based materials. Under solution conditions that favor the appropriate acid-base and colloidal chemical interactions, nanometer-size particles organize into multiscale-ordered ensembles in the form of micron-sized spheres with submicron-thick shells. The self-assembly chemistry is very flexible, and can be extended to different NP compositions, polymer molecules, and multivalent anions. The ease of encapsulation, the mild conditions of microcapsule synthesis, and the structural robustness and semi-permeability of the organic/inorganic shell wall collectively point to the exciting possibilities of microcapsules and surface-patterned microcapsule arrays as controlled release devices and reaction vessels.

### *Experimental*

*Materials:* FITC-tagged poly(*L*-lysine hydrobromide) (68 kDa), poly(*L*-lysine hydrobromide) (30 and 222 kDa), poly(*L*-arginine) (94 kDa), poly(allylamine hydrochloride) (15 and 70 kDa), branched poly(ethyleneimine) (750 kDa), poly(sodium 4-styrenesulfonate) (PSS, 70 kDa), Poly(acrylic acid, sodium salt) (PAA, 30 kDa, 40 wt% in water), all the salts, and EDTA buffer solution (2mM EDTA, pH

8.4) were procured from Sigma-Aldrich (USA) and used as-received. All solutions were prepared using deionized water (18.2 M $\Omega$ , Barnstead NANOpure Diamond water purification system). SiO<sub>2</sub> NPs (Snowtex-O, 13 $\pm$ 3 nm, 20 wt% SiO<sub>2</sub>, pH 3.4) were obtained from Nissan Chemical (USA). ZnO (DP5370, 50-90 nm, 30 wt % containing 4 wt% of PAA salt, pH 9.5), and SnO<sub>2</sub> (SN15, 10-15 nm, 15 wt %, pH 10) were purchased from Nyacol Nanotechnologies (USA) and used after dilution in water. Citrate-stabilized CdSe NPs (3-5 nm) were synthesized in an aqueous medium through the reaction of a cadmium nitrate with a selenourea. Carboxylated polystyrene NPs tagged with FITC were obtained from Molecular Probes, Inc. (USA).

*Synthesis of SiO<sub>2</sub> microcapsules:* In all the preparations, 21  $\mu$ l of an aqueous polymer solution (2 mg/ml) is gently mixed for 10 sec with 125  $\mu$ l of a salt solution (Na<sub>4</sub>EDTA or Na<sub>3</sub>Cit). The overall charge ratio  $R$  was varied from 0.5 to 100 by adding same volume of varying salt concentration to maintain a constant polymer concentration. The polymer/salt solution was aged for different times (2-30 min) and then vortex mixed with 125  $\mu$ l of a silica sol for 20 sec. The resultant silica microcapsules were aged for 2 hr and then centrifuged, decanted, and re-suspended in EDTA buffer for further characterization.

*Synthesis of SiO<sub>2</sub> solid spheres:* Silicic acid, with a nominal composition of Si(OH)<sub>4</sub>, was prepared at a 1 M concentration by dissolving tetramethylorthosilicate into 10<sup>-3</sup> M HCl solution, and used within 1 hr. Silica spheres were obtained by mixing 125  $\mu$ l of silicic acid with the above polymer-aggregate suspension for 10 sec. The resulted silica spheres were immediately centrifuged, decanted, and re-suspended in water.

*Synthesis of Microcapsule from other NPs:* Microcapsule synthesis from various NPs and polyamines was carried out as follows: 21  $\mu$ l of a FITC tagged-PLL or PAH

solution (2 mg/ml) was mixed with 125  $\mu$ l of Na<sub>3</sub>Cit solution ( $R = 10$ ) and aged for 30 min. To this salt/polymer suspension was added different NPs or anionic polymers with the following volumes and concentrations, respectively: SiO<sub>2</sub> (Snowtex-O, 125  $\mu$ l, 20 wt% solids); ZnO (125  $\mu$ l, 1 wt %); SnO<sub>2</sub> (125  $\mu$ l, 5 wt %); CdSe (125  $\mu$ l, 5  $\mu$ M); carboxylated polystyrene (100  $\mu$ l, 0.01 wt %); PAA (30  $\mu$ l, 5.0 wt %); PSS (30  $\mu$ l, 3.0 wt %).

*Enzyme Encapsulation and Testing:* 10  $\mu$ l of acid phosphatase enzyme solution (7.5 mg/ml = 40.2 units/ml in EDTA buffer, pH 8.4) was added to a citrate/PLL suspension ( $R = 10$ ), which was prepared by mixing 21  $\mu$ l of PLL (2 mg/ml, 222 kDa) and 125  $\mu$ l of Na<sub>3</sub>Cit (5.36 mM) and aged for 20 min. The reaction suspension was aged for 10 min before SiO<sub>2</sub> NP was added and thoroughly mixed. The resulting microcapsule suspension was centrifuged and rinsed with EDTA buffer several times, to ensure removal of any free enzymes. Enzyme loading of the microcapsules was determined by assaying the catalytic activity of the free enzyme in the wash. An encapsulation efficiency of 60% was estimated. 5  $\mu$ l of 0.1 mM FDP solution was added to the washed microcapsules, and the reaction mixture was imaged via confocal microscopy.

*Characterization Techniques:* The structures were characterized in the wet state via brightfield optical microscopy (Carl Zeiss Axioplan2 and Nikon Eclipse E600), laser scanning confocal microscopy (Carl Zeiss, LSM 510 Meta), fluorescence spectroscopy (Jobin–Yvon Horiba Fluoromax 3 spectrophotometer), and Coulter counter measurements (Beckman Coulter, Multisizer 3). In the dry state, the structures were analyzed via transmission electron microscopy (TEM, JEM 2010 FasTEM), scanning electron microscopy (SEM, JEOL6500), and thermogravimetric analysis (TA Instruments, SDT 2960). Tapping mode atomic force microscopy (AFM) was

performed on Digital Instrument Nanoscope IIIA Atomic Force Microscope using a 125 micrometer TESP tip. Dynamic light scattering (DLS) and zeta potential analysis were carried out with a Brookhaven Instruments ZetaPALS with BI-9000AT digital autocorrelator. Zeta potentials were calculated from electrophoretic mobility measurements using Henry's equation (for NPs) and Smoluchowski's equation for polymer aggregates.

## References

- [1] Mann, S., Ozin, G.A. Synthesis of inorganic materials with complex form *Nature*, **1996**, 382, 313.
- [2] Whitesides, G.M., Boncheva, M. Beyond molecules: Self-assembly of mesoscopic and macroscopic components *Proceedings of the National Academy of Sciences of The United States of America*, **2002**, 99, 4769.
- [3] Shenhar, R., Rotello, V.M. Nanoparticles: Scaffolds and building blocks *Accounts of Chemical Research*, **2003**, 36, 549.
- [4] Rogach, A.L. Binary superlattices of nanoparticles: Self-assembly leads to "metamaterials" *Angewandte Chemie International Edition*, **2004**, 43, 148.
- [5] Pileni, M.P. Nanosized particles made in colloidal assemblies *Langmuir*, **1997**, 13, 3266.
- [6] Murray, c.b., Kagan, c.r., Bawendi, m.g. Self-organization of CdSe nanocrystallites into 3-dimensional quantum-dot superlattices *Science*, **1995**, 270, 1335.
- [7] Zeng, H., Li, J., Liu, J.P., Wang, Z.L., Sun, S.H. Exchange-coupled nanocomposite magnets by nanoparticle self-assembly *Nature*, **2002**, 420, 395.
- [8] Kimura, M., Kobayashi, S., Kuroda, T., Hanabusa, K., Shirai, H. Assembly of gold nanoparticles into fibrous aggregates using thiol-terminated gelators *Advanced Materials*, **2004**, 16, 335.



- [9] Li, H.Y., Park, S.H., Reif, J.H., LaBean, T.H., Yan, H. DNA-templated self-assembly of protein and nanoparticle linear arrays *The Journal of American Chemical Society*, **2004**, *126*, 418.
- [10] Moriarty, P., Taylor, M.D.R., Brust, M. Nanostructured cellular networks *Physical Review Letters*, **2002**, *89*, 248.
- [11] Lee, S.W., Lee, S.K., Belcher, A.M. Virus-based alignment of inorganic, organic, and biological nanosized materials *Advanced Materials*, **2003**, *15*, 689.
- [12] McMillan, R.A., Paavola, C.D., Howard, J., Chan, S.L., Zaluzec, N.J., Trent, J.D. Ordered nanoparticle arrays formed on engineered chaperonin protein templates *Nature Materials*, **2002**, *1*, 247.
- [13] Theobald, J.A., Oxtoby, N.S., Phillips, M.A., Champness, N.R. Controlling molecular deposition and layer structure with supramolecular surface assemblies *Nature*, **2003**, *424*, 1029.
- [14] Redl, F.X., Cho, K.S., Murray, C.B., O'Brien, S. Three-dimensional binary superlattices of magnetic nanocrystals and semiconductor quantum dots *Nature*, **2003**, *423*, 968.
- [15] Rabani, E., Reichman, D.R., Geissler, P.L., Brus, L.E. Drying-mediated self-assembly of nanoparticles *Nature*, **2003**, *426*, 271.
- [16] Tripp, S.L., Pusztay, S.V., Ribbe, A.E., Wei, A. Self-assembly of cobalt nanoparticle rings *The Journal of American Chemical Society*, **2002**, *124*, 7914.
- [17] Hassenkam, T., Norgaard, K., Iversen, L., Kiely, C.J., Brust, M., Bjornholm, T. Fabrication of 2D gold nanowires by self-assembly of gold nanoparticles on water surfaces in the presence of surfactants *Advanced Materials*, **2002**, *14*, 1126.
- [18] Mirkin, C.A., Letsinger, R.L., Mucic, R.C., Storhoff, J.J. A DNA-based method for rationally assembling nanoparticles into macroscopic materials *Nature*, **1996**, *382*, 607.
- [19] Novak, J.P., Feldheim, D.L. Assembly of phenylacetylene-bridged silver and gold nanoparticle arrays *Journal of The American Chemical Society*, **2000**, *122*, 3979.

- [20] Tang, Z.Y., Kotov, N.A., Giersig, M. Spontaneous organization of single CdTe nanoparticles into luminescent nanowires *Science*, **2002**, 297, 237.
- [21] Yonezawa, T., Matsune, H., Kimizuka, N. Formation of an isolated spherical three-dimensional nanoparticle assembly as stable submicrometer-sized units by using an inorganic wrapping technique *Advanced Materials*, **2003**, 15, 499.
- [22] Boal, A.K., Ilhan, F., DeRouchey, J.E., Thurn-Albrecht, T., Russell, T.P., Rotello, V.M. Self-assembly of nanoparticles into structured spherical and network aggregates *Nature*, **2000**, 404, 746.
- [23] Wong, M.S., Cha, J.N., Choi, K.S., Deming, T.J., Stucky, G.D. Assembly of nanoparticles into hollow spheres using block copolypeptides *Nano Letters*, **2002**, 2, 583.
- [24] Wilcox, D.L.S.B., M., Bernat, T., Kellerman, D., Cochran, J.K.J. *Hollow and Solid Spheres and Microspheres: Science and Technology Associated with Their Fabrication and Application*; MRS Proceedings, Materials Research Society: Pittsburgh, **1995**
- [25] Caruso, F. Hollow capsule processing through colloidal templating and self-assembly *Chemistry - A European Journal*, **2000**, 6, 413.
- [26] Cha, J.N., Birkedal, H., Euliss, L.E., Bartl, M.H., Wong, M.S., Deming, T.J., Stucky, G.D. Spontaneous formation of nanoparticle vesicles from homopolymer polyelectrolytes *Journal of the American Chemical Society*, **2003**, 125, 8285.
- [27] Murthy, V.S., Cha, J.N., Stucky, G.D., Wong, M.S. Charge-driven flocculation of poly(L-lysine)-gold nanoparticle assemblies leading to hollow microspheres *Journal of the American Chemical Society*, **2004**, 126, 5292.
- [28] Caruso, F., Caruso, R.A., Möhwald, H. Nanoengineering of inorganic and hybrid hollow spheres by colloidal templating *Science*, **1998**, 282, 1111.
- [29] Kröger, N., Lorenz, S., Brunner, E., Sumper, M. Self-assembly of highly phosphorylated silaffins and their function in biosilica morphogenesis *Science*, **2002**, 298, 584.
- [30] Sumper, M., Lorenz, S., Brunner, E. Biomimetic control of size in the polyamine-directed formation of silica nanospheres *Angewandte Chemie International Edition*, **2003**, 42, 5192.

- [31] Patwardhan, S.V., Mukherjee, N., Steinitz-Kannan, M., Clarson, S.J. Bioinspired synthesis of new silica structures *Chemical Communications*, **2003**, 10, 1122.
- [32] Bosshard, H.R., Marti, D.N., Jelesarov, I. Protein stabilization by salt bridges: concepts, experimental approaches and clarification of some misunderstandings *Journal of Molecular Recognition*, **2004**, 17, 1.
- [33] De Stefano, C., Foti, C., Giuffrè, O., Sammartano, S. Dependence on ionic strength of protonation enthalpies of polycarboxylate anions in NaCl aqueous solution *Journal of Chemical and Engineering Data*, **2001**, 46, 1417.
- [34] Schmitz, K.S., *Macroions in Solution and Colloidal Suspension*, VCH Publishers, New York, **1993**.
- [35] Hunter, R.J., *Foundations of Colloid Science*, 3rd ed., Oxford University Press, New York, **2001**.
- [36] Walde, P., Ichikawa, S. Enzymes inside lipid vesicles: Preparation, reactivity and applications *Biomolecular Engineering*, **2001**, 18, 143.
- [37] Gao, C.Y., Donath, E., Möhwald, H., Shen, J.C. Spontaneous deposition of water-soluble substances into microcapsules: Phenomenon, mechanism, and application *Angewandte Chemie International Edition*, **2002**, 41, 3789.